Time-resolved Spectroscopic Study on Fundamental Chemical Reactions in a Unique Class of Solvents

Kaori Fujii

Doshisha University

2020

Table of Contents

Chapter 1

General Introduction

1.1. Solvent Effects on Chemical Reaction in Solution

In solution, solvent molecules play an important role during chemical reaction. They could alter reaction yield and kinetics in various systems from simple to complex. When considering reaction kinetics with Arrhenius equation,

$$\ln k = \ln A + \left(-\frac{E_a}{RT}\right), \tag{1.1}$$

solvent roles on the rate constant are classified in two, depending on temporal or spatial scale. For time-averaged effect, solvent could affect the rate constant, k by providing a preferred solvation environment for reactant or products, which results in changing the transition energy, E_a. On the other hand, they could also be involved in chemical reactions dynamically, retarding or enhancing reaction rate. Of course, it could alter E_a, but the solvation dynamics are also included in pre-exponential term, $\ln A$. The effect clearly appears when the time scale of solvent motion (rotation or diffusion) cannot be neglected comparing to the intrinsic reaction rate.

Studies on fundamental chemical reactions and molecular dynamics in solution have been accumulated both by experimental and theoretical researchers. From experimental side, thanks to the development of ultrafast spectroscopic method, we are now able to capture molecular dynamics with time-resolution of attosecond, at the shortest. It includes intramolecular vibration, rotation, and translational diffusion of molecule. These molecular dynamics can be obtained from time-resolved spectroscopies for molecular probes. Choosing a probe molecule may be a key strategy for a spectroscopic research, depending on what kind of information we want to extract from the time-resolved spectroscopic data.

In this thesis, fundamental chemical reactions in solution have been investigated by monitoring time-resolved spectrum and the effects of solvation energy and solvation

dynamics will be discussed. As the first topic, we focus on proton transfer (PT) reaction between solute and solvent, and discuss the reaction kinetics from the view of solvation energy and solvation dynamics. As solvents, we have selected ionic liquids (ILs) and high-temperature and high-pressure methanol. They have been reported to possess anomalous physicochemical properties that could influence the local environment around the solute. One of the unique properties of these solvents is spatial inhomogeneity at nano-order scale. Especially for ILs, the inhomogeneous liquid structure has been discussed from the dynamic aspect of solvent; how solvent molecules response to the structural change and electronic re-distribution of solute molecule during chemical reaction, because the unique properties of ILs comes from the bulky and asymmetric structure of anion and cation molecules. As the second topic of this study, we focus on the photodissociation reaction of disulfide compound in ILs. In the photodissociation process, the polarity and the molecular volume of a solute can be significantly changed, which forces surrounding solvent reorient to stabilize photo-dissociated products, i.e., geminate pair of photo-products. Additionally, the pair of photo-products undergoes recombination in a solvent cage. Formation of that solvent cage by the solvation dynamics could compete with the recombination dynamics of photo-products in ILs. We focus on the recombination kinetics in ILs and give an explanation by mathematical model. In the following we will briefly review the unique solvent properties and ILs.

1.2. Unique Classes of Liquids: Ionic Liquids and Super Critical Fluids

Ionic liquids (ILs) and supercritical fluids (SCFs) are distinguished from conventional solvent, water, alcohol and other organic solvent under ambient conditions. In this section, we introduce what makes these substances different from conventional solvents from the physicochemical aspect, and briefly summarize previous works on molecular dynamics and kinetics in ILs and SCFs.

Historically, real-time observation and theoretical analysis of chemical reaction dynamics started using a simple system (conventional liquids or gas-phase) and have been developed to more complex system. ILs and SCFs are examples of this complex and unique reaction media. Researches on chemical reactions in SCF have been actually an active area prior to those in ILs, which goes back to 1980s. With the development of experimental technology of high-pressure conditions, a lot of work have been dedicated to unveil physicochemical properties of SCF. In 1990s, ILs became to be an active area as a new solvent.

1.2.1. Physicochemical Researches on Supercritical Fluids

Super critical fluid (SCF) is defined as a fluid above the critical point that bounds liquid and gas phases. Figure 1-1 shows a phase diagram (density vs pressure) of carbon dioxide (CO_2) (critical point P_c = 7.38 MPa, T_c = 304.2 K). The red curves show isothermal lines and the blue one shows the gas-liquid phase separation. Above the critical point, density of

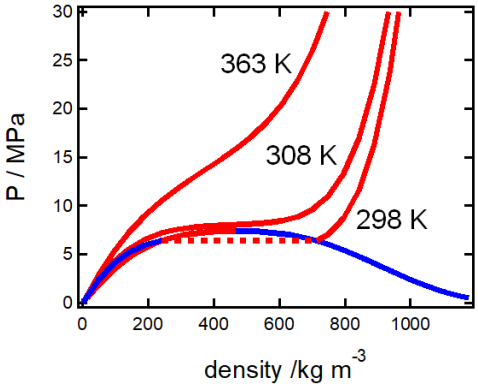

Figure 1-1. Phase-diagram (density vs Pressure) of CO_2.

fluid shows a continuous change from gas-like to liquids-like value without phase separation. This property makes SCF applicable to extend low-density, gas-like researches to high-density ones.

For a solute molecule dissolved in fluid, density of the fluid is an important parameter since it determines viscosity and dielectric properties. Researches on physicochemical properties of fluids above the critical point show that fluids should be classified based on its density: low, medium and high-density fluid. Among these three density regions, medium density region where reduced density (the density divided by the critical density of the solvent), $\rho_r (= \rho/\rho_c)$, is lied between 0.5 to 1.5, has been an active topic due to its anomalous properties related to density inhomogeneity and fluctuation. One of the experimental proofs for the density inhomogeneity was an electronic spectrum of dye molecule.[1,2] Kajimoto et al.[3] investigated the emission spectrum shift of (*N*,*N*-dimethylamino)benzonitrile (DMABN) in CF_3H at various thermal condition including supercritical region. Although the spectrum shift is correlated with the solvent polarity estimated by Onsager reaction field in conventional liquids, their experimental results on the density dependence deviated from the theoretically predicted values estimated from the dielectric constant, and a larger shift was observed near the critical density. This was interpreted by assuming that number of solvent molecules located around DMABN is larger than the average value calculated from the density of the solvent. Those anomalous phenomena, later called local density augmentation, gathered much attention. These anomalies of SCF as solvent also brought many chemists to the studies on the chemical reaction kinetics. Intra-, intermolecular electron transfer and ionic reactions have been extensively explored, since their reactants, products and transition states are sensitive to the polar character of solvent.[4-6] Kimura et al. measured electron-transfer rate in the

hexamethlbenzene-tetracyanoethylene complex in various fluids including CO_2 at various density conditions including SC state.[5,6] Experimentally obtained electron-transfer rate constant increases significantly with solvent density from the gaseous phase to the medium density region ($\rho_r < 1$), and the dependence becomes mall above the critical density ($1< \rho_r < 2$), which is considered due to the density augmentation around the reactant. The electron transfer rate was discussed in relation with the Marcus-Jortner model using the parameters (solvent fluctuation and reaction free energy) obtained by the spectral analysis.

However, most of spectroscopic studies focused on the effect of the change of the polarity caused by density inhomogeneity in medium density region in relation with charge transfer of molecules. Considering that some of the fundamental chemical reactions are controlled by intermolecular hydrogen bond (HB), we need to investigate proton transfer (PT) reaction and get insight how solvent-solvent HB formation near and above SC region influences the PT kinetics. For HB between solvent molecules, there have been many experimental and theoretical studies on water, methanol, ethanol, etc. over the wide density regions. Experimentally, Matubayasi et al. studied the HB in SC water by high-pressure NMR, and estimated the number of HB in SC water by the chemical shift of proton with the help of the molecular dynamics simulation.[7,8] Hoffman et al also used NMR spectroscopy in water[9], methanol and ethanol[10] in wide range of density, and took similar linear correlation of chemical shift with the number of HB. These studies indicated that the number of HBs is more than one per molecule around the supercritical region, which indicates that HB persists even above the critical temperature.

Since HB is molecular event, information from molecular probe gives us more direct and microscopic pictures about the HB formation between solute and solvent molecules

in wide range of solvent density.[11,12] Measuring specific vibrational modes of probe molecule that is sensitive to HB, is a direct tool to understand solute-solvent HB (see Figure 1-2). Fujisawa et al.[11] measured Raman shift of NO_2 and NH_2 stretching mode of p-nitroaniline (pNA) in methanol and ethanol over the wide range of density, and found that the vibrational frequency of the NH_2 stretching mode showed a unique solvent density dependence; i.e. from the gaseous to the density near critical density ($\rho_r \cong 1$) the frequency showed a large low frequency shift, and from $\rho_r \cong 1$ to 2, the density dependence becomes small. Further increase of the density brought a large negative shift of the spectrum. Later Kobayashi et al. indicated that the vibrational frequency shift of NH_2 stretching mode is correlated with the HB basicity (β of Kamlet-Taft parameters).[13] HB acidity (α of Kamlet-Taft parameters) was also investigated by Raman shift of C=O stretching mode of benzophenone (BP). Fujisawa et al. found that the CO stretching vibration of benzophenone (BP) is correlated with solvent acceptor number which is closely related to the hydrogen-bonding acidity.[14] Recently Kimura et al. measured the Raman spectra of BP in methanol and ethanol at various densities,[12] and found a similar density dependence of the spectra shift observed for the NH_2 stretching mode of pNA. In Figure 1-2, solvent parameters of HB ability (α and β) of methanol and ethanol are plotted against solvent density together with the Rama spectra of probe molecules at different solvent densities. In lower density region ($\rho_r < 0.5$) and higher density region ($\rho_r > 1.5$) these parameters show liner correlation with density. On the other hand, in medium density region ($0.5 < \rho_r < 1.5$), their dependence on the density is small, which is interpreted by the saturation of solvent density around solute molecules.

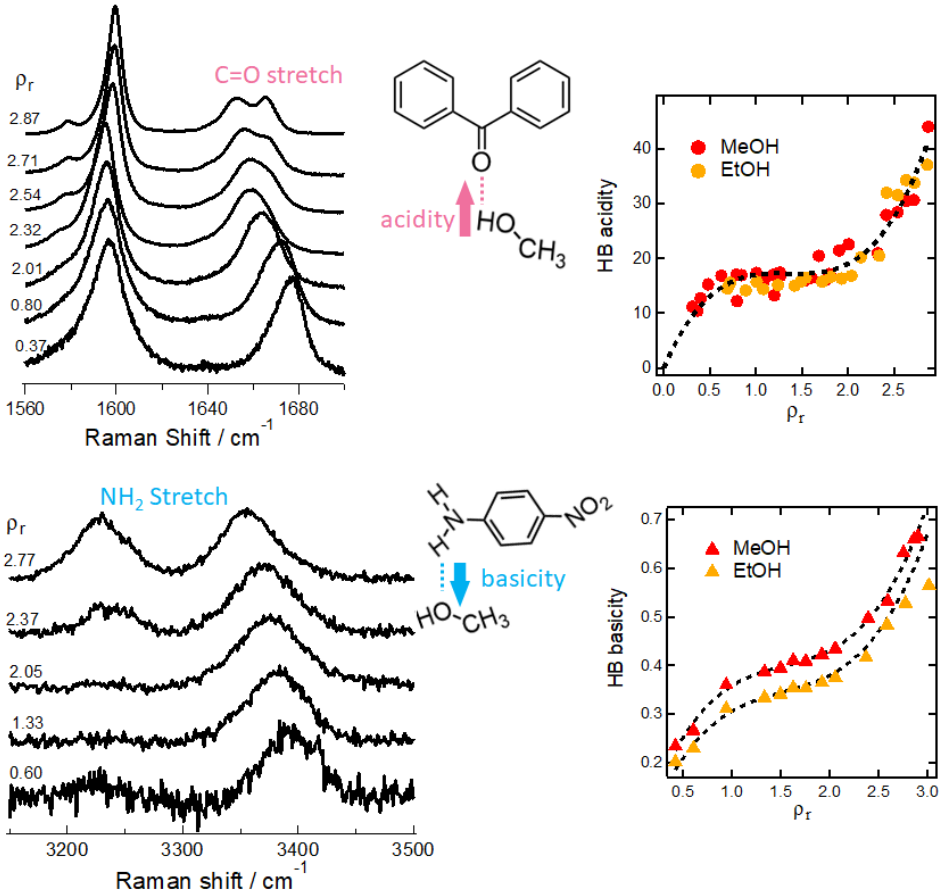

Figure 1-2. Hydrogen-bonding acidity and basicity in methanol and ethanol determined by Raman shift of molecular probes.

1.2.2. Physicochemical Researches on Ionic Liquids

Ionic liquids (ILs) are family of salts whose melting point is under 100 ℃, due to the bulky and asymmetric structure of the cations. Typical examples of the molecular structure of cations and anions commonly used for ILs are shown in Figure 1-3. Abbreviations of the names of cations of ILs are also noted in the Figure and caption. By changing the pairs of anions and cations, a variety of ILs that have special functionality can be synthesized.

From the physicochemical aspect, ILs have been paid attention as reaction media because of their unique solvation abilities. In 2000s, an existence of inhomogeneous

structure of ILs was experimentally and theoretically demonstrated by several groups.

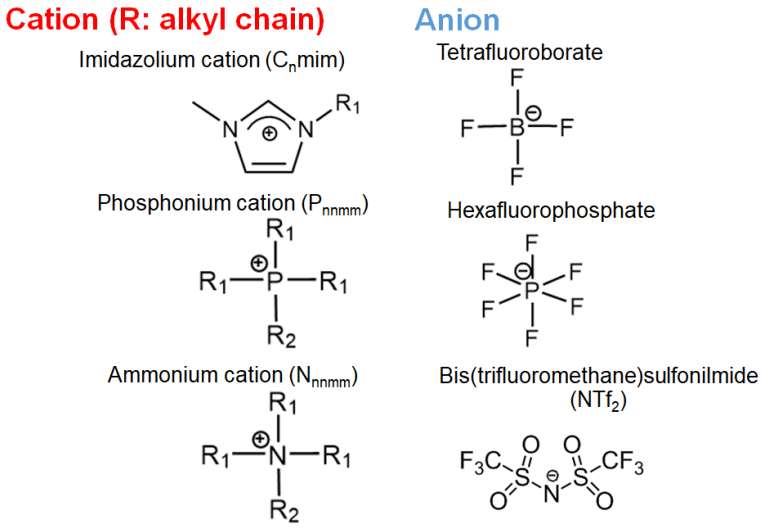

Figure 1-3. Typical cations and anions composed of ionic liquids. Abbreviated names are given in parenthesis. (n and m represent the number of alkyl carbon in cation). 1-akyl-3-methylimidazolimu cation is abbreviated as C_nmim^+, where n indicates the number of carbon atoms in the alkyl-chain. Phosphonium and ammonium cations are abbreviated as P_{nmmm}^+ or N_{nmmm}^+, where m and n are the number of carbon atoms in the alkyl-chains of R_1 and R_2, respectively. Bis(trifluoromethanesulfonyl)imide anion is abbreviated as NTf_2^-.

Figure 1-4 shows snap shot of typical imidazolium ILs with different number of alkyl carbons (n=4 (upper picture) and 12 (bottom picture)). A polar group composed of charged head group of anion and cation (red region in the snap shot), and a non-polar group composed of alkyl carbons in cation (green region) are heterogeneously distributed and formed periodically segregated structure in several ten angstroms. This segregated structure is clearly observed when the cation has a long alkyl chain such as $[C_{12}mim][NTf_2]$. Using molecular dynamics simulation, Lopes and co-workers gave clear snapshots of imidazolium ILs ($[C_nmim][PF_6]$, n = 2, 4, 6, 8, 12) and proposed the existence of nanometer scale structure for ILs of n > 4 by the aggregation of alkyl chains in the non-polar domain.[15] From the experimental side, by X-ray scattering, Triolo and co-workers found the peak in low-Q domain for $[C_nmim][BF_4]$ (n = 4, 6, 8).[16] It is the

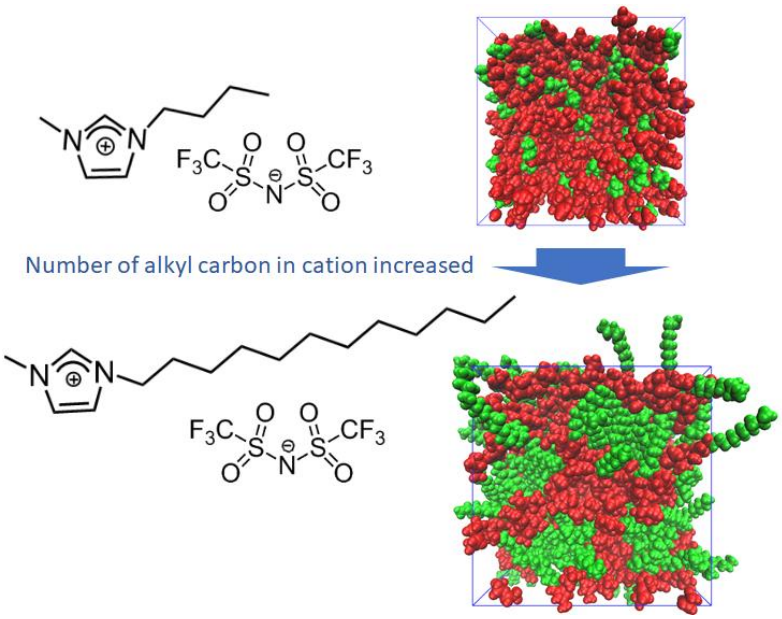

Figure 1-4. Segregated structure of imidazolium ILs. (snapshot from molecular dynamics simulation). Red region is composed of anion and charged group of cation (imidazolium ring and alkyl carbon directly bonded to nitrogen in the imidazolium ring), and green region contains remaining alkyl carbons.

first experimental evidence of the nanoscale correlations in thermodynamically stable ILs.

Due to the unique liquid structure of ILs, solute molecules dissolved in them show anomalous behavior differently from the conventional liquid solvents. For example, rotational and diffusional dynamics of various types of solutes have been investigated by several groups. In the case of translational diffusion, Kaintz et al. assessed diffusional coefficients of various solutes with different aspect ratios in 1-alkyl-1-methylpyrrolidinium bis(trifluoromethanesulfonyl)imides ([Pr_n1][NTf_2], n = 3, 4, 6, 8, and 10) by NMR spectroscopy (pulsed-field-gradient (PFG)-NMR) and compared obtained diffusion coefficients with those in conventional solvents.[17] In ILs, experimentally obtained diffusion coefficients deviate from the theoretically predicted values from the Stokes-Einstein (SE) equation which predicts self-diffusion coefficients of solute as

$$D = k_{\mathrm{B}}T/C\eta r, \tag{1.1}$$

where T temperature, η viscosity of solvent, r the radius of the solute, and C friction parameter between solute and solvent. One of the reasons for this deviation is the ratio of van der Waals volume of solute and solvent ILs. Since ILs is composed of bulky and asymmetric species as mentioned in the last section, we cannot assume that the environment provided by ILs is continuum. By including the effect of the different size into the SE equation, experimentally obtained diffusional behavior of various solutes in ILs are successfully explained.[18]

Considering local environment provided by ILs is quite different from that in conventional solvent, chemical reaction of solute molecules should be complex in ILs. In addition to molecular size effect of cation and anion in ILs, their viscous environment could affect reaction kinetics: reaction rate constant could be controlled by reorganization of solvent and diffusion process of anion and cation. Elementary reaction process, such as proton transfer, charge transfer and isomerization reaction have been main topics in this field. Li and Maroncelli studied intramolecular electron transfer in three types of solutes that all exhibit two electronically excited states depending on the local polarity (locally excited state and charge-transfer state).[19] Several examples indicate that in ILs, solvent motion plays a significant role to determine whole reaction rate process. To understand that kinetics in ILs completely, we need to know how solvent ILs response to the local perturbation given by solute: structural change or charge redistribution of solute molecule by chemical reaction. So far, many research groups have been experimentally and computationally involved in the solvation dynamics of ILs. From the experimental side, Maroncelli and coworker's works have given complete description of dynamic response of ILs in wide range of time-scale.[20,21] They combined two spectroscopic

methods to detect time-resolved fluorescence of solute molecule, optical Kerr-gated emission and time-correlated single photon-counting, whose time-window are 100 fs-200 ps and 50 ps-5 ns, respectively. They observed that solvent response was biphasic, sub-picosecond response with modest contribution and slow component whose time-scale were widely distributed (several picoseconds to several hundred nanosecond).

1.3. Theoretical Background for Bimolecular Diffusion Limited Reactions

In Section 1.2, we introduce the physicochemical properties of supercritical fluids and ionic liquids, and how they have been attracted as a reaction media by picking up representative researches in the fields. Although we mainly pick up experimental studies in the previous section, it is needless to say that there have also been great contributions from computational and theoretical research groups. Computer simulations (molecular dynamics simulations and quantum chemical calculations) and theoretical formulations can give clear explanations to understand experimental observation. In this section, we pick up the development of theoretical researches on the bimolecular diffusion limited reaction in solution, since we will mainly treat the bimolecular reactions in this thesis (proton transfer reaction and geminate recombination reaction from the photodissociation).

Consider a bimolecular reaction between A and B, one of the well-explored chemical reaction theoretically. When the activation energy for the reaction is small, the reaction rate is controlled by the diffusion process in which where one of the reactants diffuses toward another to be close enough to react. This diffusion limited reaction was first formulated by Smoluchowski.[22] He gave diffusional equation for the number density (n) of A, considering a spherical radius of A surrounded by excess concentration of B. By solving the equation under a boundary condition at reaction radius (R) of A and B, where the concentration of B is zero (called absorbing boundary condition), we obtain the flux (j) of B toward A and steady-state rate constants k. According to the model, the bimolecular reaction rate k is given by

$$k = 4\pi R D_{\mathrm{AB}}, \tag{1.2}$$

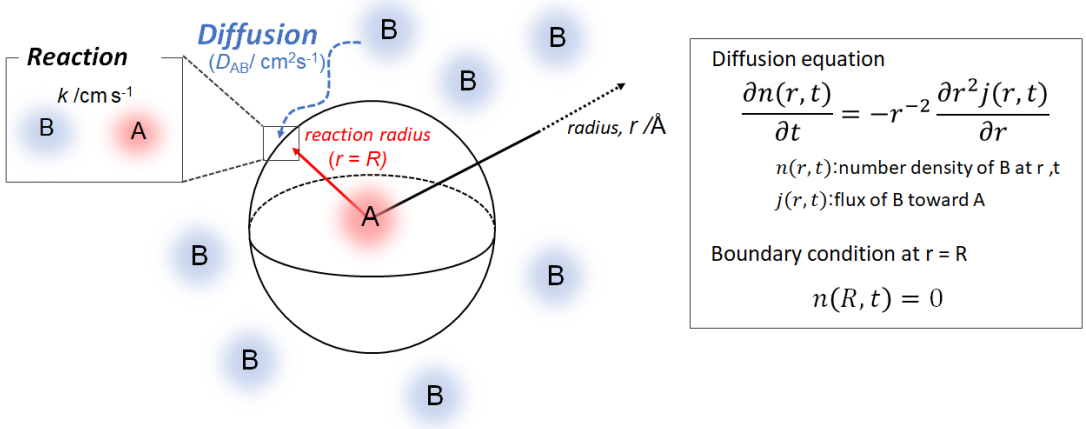

Figure 1-5. Diffusion limited bimolecular reaction between A and B, based on Smoluchowski's theory (absorbing boundary condition).

where D_{AB} is the mutual diffusion coefficient between A and B molecules. Although Smolchowski's theory has been often used to interpret experimental results, there have also been number of researches to test and revise the theory to simulate experimentally or computationally obtained chemical reaction dynamics. For example, Collins and Kimball revised the boundary condition in the Smoluchowski equation by considering the velocity distribution rather than density distribution at a collision radius. Their improved version of diffusional equation (Smoluchowski-Collins-Kimball equation[23]) has shown to successively reproduce transient dynamics in solution. Reproducing experimental observations with theoretical model has been one of major stream to develop the diffusion-influencing chemical reaction. Recombination dynamics of iodine atoms and complex formation of aromatic fluorescence dye molecule in the excited states (fluorescence quenching) have been well studied themes, since it can be assessed by the fluorescence lifetime measurement. [24-27]

Another great contribution was made by Ibuki and Ueno.[28] Using the computer simulation (MD and Langevin Dynamics (LD) simulation) to compare theoretical model,

they focused on the chemical reaction in short time where diffusional equation based on Smolchowski's theory failed to reproduce. This failure is because in the initial several picoseconds, bimolecular reaction between neighboring A and B would proceed: B diffusing from the bulk would not be involved in the reaction at the initial stage. They introduced the potential mean force of surrounding media and also modified the boundary condition of the reaction using the velocity distribution of the reactant molecule, and succeeded in reproducing the initial dynamics of the reaction. Ibuki and Ueno also developed another mathematical model, Fokker-Planck-Kramers equation, to treat diffusion limited reactions in the short time reaction.[29-31]

Understanding of diffusion coefficient has been another topic in this area. Generally, diffusion coefficient is modeled by hydrodynamic formula, Stokes-Einstein (SE) equation (eq. (1.1)). Since that approximation blurs the real situation, the case where the SE equation succeeds in simulating experimental results is rare. According to the molecular hydrodynamics theory, the diffusion coefficient is related with the friction acting on the molecule as,[32]

$$D = \frac{k_{\mathrm{B}}T}{m\xi}, \tag{1.3}$$

where m is the mass of the molecule, and ξ is the friction acting on the molecule. Generally, the friction acting on the molecule is time-dependent,

$$\xi = \int_0^\infty \xi(t)dt. \tag{1.4}$$

A lot of works has been devoted to understand the origin of the friction acting on the solute molecule. For the diffusional motion in supercritical fluids, Yamaguchi et al. have focused on origin of diffusion coefficient of solute molecule by molecular dynamics (MD) simulation of solute molecules in Lenard-Jones (LJ) fluids.[33,34] Based on eq (1.4) they

discussed the roles of attractive and repulsive solute-solvent interaction by varying LJ parameters.

In order to consider the detail of molecular dynamics during chemical reaction, the process before the reactants encountering and solute-solvent interaction that could alter not only intrinsic chemical reaction but also diffusional motion, should be discussed.

1.4. Scope of This Study

In this study, we aim to investigate solvent effect of supercritical fluids and ionic liquids on the chemical reaction kinetics. Time-resolved spectroscopic measurements were applied to capture reaction dynamics of solute molecule and solvation dynamics of ILs.

This thesis consists of five chapters. Chapter 1 is this introduction. In Chapters 2 and 3, we focus on the intermolecular proton transfer (PT) between solute and solvent molecule. We used cyano-derivatives of 2-naphthol as fluorescence probe molecules that undergo the excited state proton transfer (ESPT). By measuring the time-resolved fluorescent spectrum of cyanonaphthols, we obtain rate constants of ESPT and discuss them in relation with solvent properties. In Chapter 2, high-temperature and high-pressure methanol including supercritical state is selected as solvent. Experimentally obtained PT rate constants are discussed with solvent Kamlet-Taft parameter, hydrogen-bond basicity (β) and polarity/polarizability (π^*)

In Chapter 3, we study protic ionic liquids (PILs) as a solvent. Three PILs composed of different anion species ($[N_{222}H][CF_3SO_3]$, $[N_{222}H][CH_3SO_3]$ and $[N_{222}H][CF_3COO]$) are prepared. PT yield and dynamics are affected by the hydrogen-bond basicity of solvent molecules. PT mechanism in three different PILs are highly dependent on the acidity of conjugate acid of anion.

In Chapters 4 and 5, we focus on photodissociation reaction of disulfide compound (bis-(*p*-aminophenyl)disulfide) in ILs. Transient absorption spectrum and time-resolved emission spectrum after the photodissociation are measured in various ILs composed of tetraalkylphosphonium and tetraalkylammonium cation. In Chapter 4, we discuss solvation dynamics of ILs after the photodissociation. Time-profile of spectrum shift in

the transient absorption spectrum and time-resolved emission spectrum of photodissociated product (p-aminophenylthyil radical) are discussed to understand solvent reorientation of ILs around radicals. Intriguing behavior in the emission spectrum shift is found. To elucidate experimentally obtained results, non-equilibrium molecular dynamics (MD) simulation is conducted.

Topic of Chapter 5 is recombination dynamics of geminate pair of p-aminophenylthyil radicals. By analyzing integral of transient absorption spectrum at each time (change in concentration of thyilradical), we discuss the yield and dynamics of recombination in ILs. Mathematical model to explain the experimental results are proposed in this study.

Concluding remarks are given in Chapter 6, where the new findings and accumulated knowledge obtained in this thesis are summarized.

References

1. Yamaguchi, T.; Kimura, Y.; Hirota, N., Solvent and Solvent Density Effects on the Spectral Shifts and the Bandwidths of the Absorption and the Resonance Raman Spectra of Phenol Blue. *The Journal of Physical Chemistry A* **1997,** *101* (48), 9050-9060.

2. Kimura, Y.; Hirota, N., Effect of solvent density and species on static and dynamic fluorescence Stokes shifts of coumarin 153. *The Journal of Chemical Physics* **1999,** *111* (12), 5474-5484.

3. Kajimoto, O.; Futakami, M.; Kobayashi, T.; Yamasaki, K., Charge-transfer-state formation in supercritical fluid: (N,N-dimethylamino)benzonitrile in trifluoromethane. *The Journal of Physical Chemistry* **1988,** *92* (5), 1347-1352.

4. Takahashi, K.; Sawamura, S.; Jonah, C. D., Solvent reorganization energies measured by an electron transfer reaction in supercritical ethane. *The Journal of Supercritical Fluids* **1998,** *13* (1), 155-161.

5. Kimura, Y.; Takebayashi, Y.; Hirota, N., Electron-transfer rate in the hexamethylbenzene-tetracyanoethylene charge-transfer complex in carbon dioxide. *Chemical Physics Letters* **1996,** *257* (5), 429-433.

6. Kimura, Y.; Takebayashi, Y.; Hirota, N., Effect of the solvent density and species on the back-electron transfer rate in the hexamethylbenzene/tetracyanoethylene charge-transfer complex. *The Journal of Chemical Physics* **1998,** *108* (4), 1485-1498.

7. Matubayasi, N.; Wakai, C.; Nakahara, M., Structural study of supercritical water. I. Nuclear magnetic resonance spectroscopy. *The Journal of Chemical Physics* **1997,** *107* (21), 9133-9140.

8. Matubayasi, N.; Wakai, C.; Nakahara, M., Structural study of supercritical water. II. Computer simulations. *The Journal of Chemical Physics* **1999,** *110* (16), 8000-8011.

9. Hoffmann, M. M.; Conradi, M. S., Are There Hydrogen Bonds in Supercritical Water? *Journal of the American Chemical Society* **1997,** *119* (16), 3811-3817.

10. Hoffmann, M. M.; Conradi, M. S., Are There Hydrogen Bonds in Supercritical Methanol and Ethanol? *The Journal of Physical Chemistry B* **1998,** *102* (1), 263-271.

11. Fujisawa, T.; Terazima, M.; Kimura, Y., Solvent Effects on the Local Structure of p-Nitroaniline in Supercritical Water and Supercritical Alcohols. *The Journal of Physical Chemistry A* **2008,** *112* (24), 5515-5526.

12. Kimura, Y.; Fukura, T.; Asada, Y.; Ueno, M.; Yasaka, Y., Raman spectroscopic study on the acceptor number of supercritical methanol and ethanol. *Journal of Molecular Liquids* **2017,** *245*, 11-16.

13. Kobayashi, A.; Osawa, K.; Terazima, M.; Kimura, Y., Solute–solvent hydrogen-bonding in room temperature ionic liquids studied by Raman spectroscopy. *Physical Chemistry Chemical Physics* **2012,** *14* (39), 13676-13683.

14. Fujisawa, T.; Ito, T.; Terazima, M.; Kimura, Y., Raman Spectroscopic Study of the Solvation of Decafluorobenzophenone Ketyl Radical and Related Compounds in 2-Propanol at Ambient to Supercritical Temperatures. *The Journal of Physical Chemistry A* **2008,** *112* (9), 1914-1921.

15. Canongia Lopes, J. N. A.; Pádua, A. A. H., Nanostructural Organization in Ionic Liquids. *The Journal of Physical Chemistry B* **2006,** *110* (7), 3330-3335.

16. Triolo, A.; Russina, O.; Bleif, H.-J.; Di Cola, E., Nanoscale Segregation in Room Temperature Ionic Liquids. *The Journal of Physical Chemistry B* **2007,** *111* (18), 4641-4644.

17. Kaintz, A.; Baker, G.; Benesi, A.; Maroncelli, M., Solute Diffusion in Ionic Liquids, NMR Measurements and Comparisons to Conventional Solvents. *The Journal of Physical Chemistry B* **2013,** *117* (39), 11697-11708.

18. Kimura, Y.; Kida, Y.; Matsushita, Y.; Yasaka, Y.; Ueno, M.; Takahashi, K., Universality of Viscosity Dependence of Translational Diffusion Coefficients of Carbon Monoxide, Diphenylacetylene, and Diphenylcyclopropenone in Ionic Liquids under Various Conditions. *The Journal of Physical Chemistry B* **2015,** *119* (25), 8096-8103.

19. Li, X.; Liang, M.; Chakraborty, A.; Kondo, M.; Maroncelli, M., Solvent-Controlled Intramolecular Electron Transfer in Ionic Liquids. *The Journal of Physical Chemistry B* **2011,** *115* (20), 6592-6607.

20. Arzhantsev, S.; Ito, N.; Heitz, M.; Maroncelli, M., Solvation dynamics of coumarin 153 in several classes of ionic liquids: cation dependence of the ultrafast component. *Chemical Physics Letters* **2003,** *381* (3), 278-286.

21. Jin, H.; Baker, G. A.; Arzhantsev, S.; Dong, J.; Maroncelli, M., Solvation and Rotational Dynamics of Coumarin 153 in Ionic Liquids: Comparisons to Conventional Solvents. *The Journal of Physical Chemistry B* **2007,** *111* (25), 7291-7302.

22. Von Smoluchowski, M., Mathematical theory of the kinetics of the coagulation of colloidal solutions. *Z. Phys. Chem* **1917,** *92*, 129-168.

23. Collins, F. C.; Kimball, G. E., Diffusion-controlled reaction rates. *Journal of Colloid Science* **1949,** *4* (4), 425-437.

24. Szabo, A., Theory of diffusion-influenced fluorescence quenching. *The Journal of Physical Chemistry* **1989,** *93* (19), 6929-6939.

25. Eads, D. D.; Dismer, B. G.; Fleming, G. R., A subpicosecond, subnanosecond and steady-state study of diffusion-influenced fluorescence quenching. *The Journal of Chemical Physics* **1990,** *93* (2), 1136-1148.

26. Sikorski, M.; Krystkowiak, E.; Steer, R. P., The kinetics of fast fluorescence quenching processes. *Journal of Photochemistry and Photobiology A: Chemistry* **1998,** *117* (1), 1-16.

27. Okamoto, M., Diffusion-Controlled Reaction in Supercritical Fluid. *Review of High Pressure Science and Technology/Koatsuryoku No Kagaku To Gijutsu* **2004,** *14* (1), 30-36.

28. Ibuki, K.; Ueno, M., Theories and Simulations of Short-Time Dynamics of Diffusion-Controlled Reactions. *Review of High Pressure Science and Technology/Koatsuryoku No Kagaku To Gijutsu* **2004,** *14* (1), 20-29.

29. Kazuyasu, I.; Fumihiro, N.; Masakatsu, U., Improved Velocity Distribution Applied to Fokker–Planck–Kramers Equation Treatment for Dynamics of Diffusion-Controlled Reactions in Two Dimensions. *Bulletin of the Chemical Society of Japan* **2003,** *76* (2), 261-270.

30. Ibuki, K.; Ueno, M., Fokker–Planck–Kramers equation treatment of dynamics of diffusion-controlled reactions using continuous velocity distribution in three dimensions. *The Journal of Chemical Physics* **2003,** *119* (14), 7054-7064.

31. Ibuki, K.; Ueno, M., Improved treatment of inertia and non-Markovian effects on short-time dynamics of diffusion-controlled reaction based on generalized diffusion equation. *The Journal of Chemical Physics* **1997,** *106* (24), 10113-10122.

32. Hansen, J.-P.; McDonald, I. R., *Theory of simple liquids*. Elsevier: 1990.

33. T. Yamaguchi Y. Kimura N, H., Molecular dynamics simulation of solute diffusion in Lennard-Jones fluids. *Molecular Physics* **1998,** *94* (3), 527-537.

34. Yamaguchi, T.; Kimura, Y., Effects of solute-solvent and solvent-solvent attractive interactions on solute diffusion. *Molecular Physics* **2000,** *98* (19), 1553-1563.

Chapter 2

Proton Transfer Dynamics in High-temperature and High-pressure Methanol

2.1. Introduction

Hydrogen-bonding ability of solvent plays an important role in solute-solvent intermolecular proton transfer (PT). Considering that the parameters for HB ability (Kamlet-Taft parameters, α[1] and β[2]) of solvent show non-linear dependence on the density above and near the critical point, PT reaction kinetics might be affected by that anomalous change in these solvent parameters. In this study, we investigate intermolecular PT in methanol at various thermal condition including SC region and discuss how PT yield and rate constants are explained by the solvation environment given by the change of Kamlet-Taft parameters.

As a probe molecule, we selected one of the famous photoacids, 2-naphthols, whose acidity is enhanced in the electronically excited state. Substituted compounds of 2-naphthol with an electron withdrawing group at the C5 and/or C8 site show large enhancement of acidity. For example, the values of pK_a* (pK_a in the excited states) of 5-cyano-2-naphthol (5CN2) and 5, 8-dicyano-2-naphthol (DCN2) are reported to be -0.75 and -4.5, respectively, while that of 2-naphthol is 2.8.[3-5] Because of the remarkable enhancement of the acidity, they can undergo excited-state proton transfer (ESPT) not only in water but also in organic solvents such as alcohols, DMSO and so on. Since cyano-substituted 2-naphthols show dual fluorescence from the normal form (ROH*) at shorter wavelength and the anionic form (RO^-*) at longer wavelength as shown in Figure 2-1, we can clarify the kinetics of PT by monitoring the fluorescence dynamics.

Studies on solute-solvent PT dynamics in SCF is not so many, because of the difficulty of time-resolved spectrum measurement in extreme condition. Green et al.[6] determined rate constant of ESPT of 2-naphthol in water from ambient to critical condition. They found PT rate showed large deviation from the Arrhenius behavior above

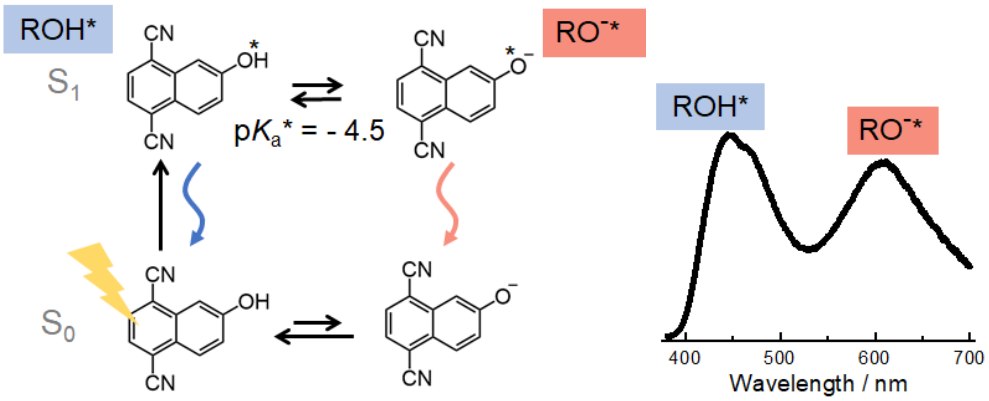

Figure 2-1. Excited state proton transfer (ESPT) of 5,8-dicyano-2-naphthol (DCN2) and fluorescence spectrum of DCN2 in ethanol.

383 K, which was attributed to change in water-water HB networks in medium density region. Fifteen years later, Kobayashi et al investigated ESPT dynamics of 5CN2 whose acidity is higher than 2-naohthol, in water at various thermal conditions and found an intermediate species of PT, contact ion pair of RO^-* with hydronium ion in the medium density region (ρ_r =1.7~2.1).[7] Solute-solvent PT kinetics are significantly affected by the solvent density and HB parameters related to change in density, and there might be some unknown mechanisms in the SC region.

In this study, to further understand intermolecular PT kinetics in HB solvents at various density and relate them with the change in Kamlet-Taft parameters, we investigate PT between DCN2 and methanol at high temperature and pressure (T_c = 512 K and P_c = 8.09 MPa) including the supercritical states. We also measured the PT dynamics in n-alcohols (n = 1, 2, 3, 4, 5, 6, 8, and 10) under ambient conditions to compare the dynamics and reaction rate with change of solvent Kamlet-Taft parameters. Due to the high-temperature condition where reaction kinetics are affected by molecular diffusion, diffusional model analysis was applied to extract PT rate from time-resolved spectrum. We found PT dissociation rate constants in the alcohols under various thermal conditions

is explained by the change of activation energy caused by the competing effects of hydrogen bonding and dipolarity/polarizability that controlled the energy state of ROH* and RO^{-}*···H, respectively.

2.2. Experiment

2.2.1. Materials

5,8-Dicyano-2-naphthol (DCN2) were synthesized according references.[5,8] Reaction schemes is shown in Appendix A1. As solvents, we used n-alcohols ($C_nH_{2n+1}OH$; n = 1, 2, 3, 4, 5, 6, 8, and 10) for the measurements under ambient conditions and methanol for the measurements at high temperature and pressure. Herein, n-$C_nH_{2n+1}OH$ is abbreviated as C_nOH. C_1OH (spectral grade), C_4OH (spectral grade), C_5OH (special grade), C_6OH (special grade), C_8OH (special grade), and $C_{10}OH$ (special grade) were purchased from Nacalai Tesque, and C_2OH (spectral grade) was purchased from Wako Chemicals. These C_nOH compounds were used without further purification. C_3OH (primary grade), purchased from Nacalai Tesque, was distilled before use.

For Spectra measurements under high temperature and high-pressure conditions were conducted along the 30 MPa isobar between room temperature (294 K) and 543 K and at 20 MPa and 543 K. Figure 2-2 is phase diagram of methanol (density vs pressure), where the solvent density is plotted as the reduced density divided by the critical density of the solvent (ρ_r). Black circles represent the condition we conducted spectrum measurements.

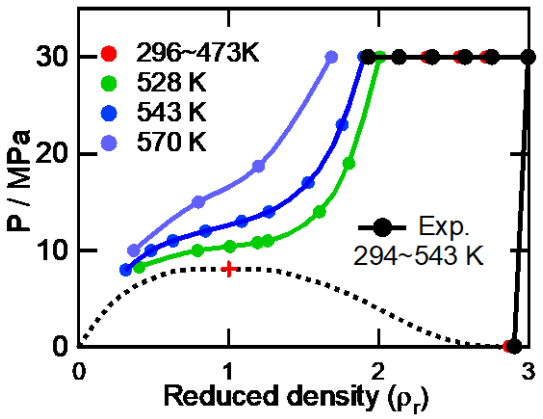

Figure 2-2. Phase diagram of methanol. Blue and green curves with makers show isotherms at various temperatures. Dashed line represents boundary of gas and liquid phase. We conducted spectrum measurements at 294 ~543 K with 30 MPa isobar.

2.2.2. Absorption and Time-Resolved Fluorescence Measurements

For the absorption spectra measurements at high temperature and pressure, we used a xenon lamp (XC-150SRE, Eagle Technology) as the light source. The light intensities with and without the solute were measured successively using a CCD spectrometer (EPP2000, Stellar Net Inc.). The sample solution, pumped using an HPLC pump (PU-1580, JASCO), was passed (flow speed, 1.5 mL/min) through a specially designed high-temperature and high-pressure cell (Figure 2-3).[9] Sample solution flowed in the pump is inducted from upside to downside of the cell. Optical pass length in this cell is determined by the distance between pair of optical windows located in the center of the cell and is 5mm. The temperature was controlled using a temperature controller (E5CN-QTC, Omron) with an accuracy of typically ±1.5 °C and monitored using a thermocouple directly inserted into the cell. The pressure of the sample solution controlled using a back-pressure regulator (880-81, JASCO) with an accuracy of ±0.3 MPa.

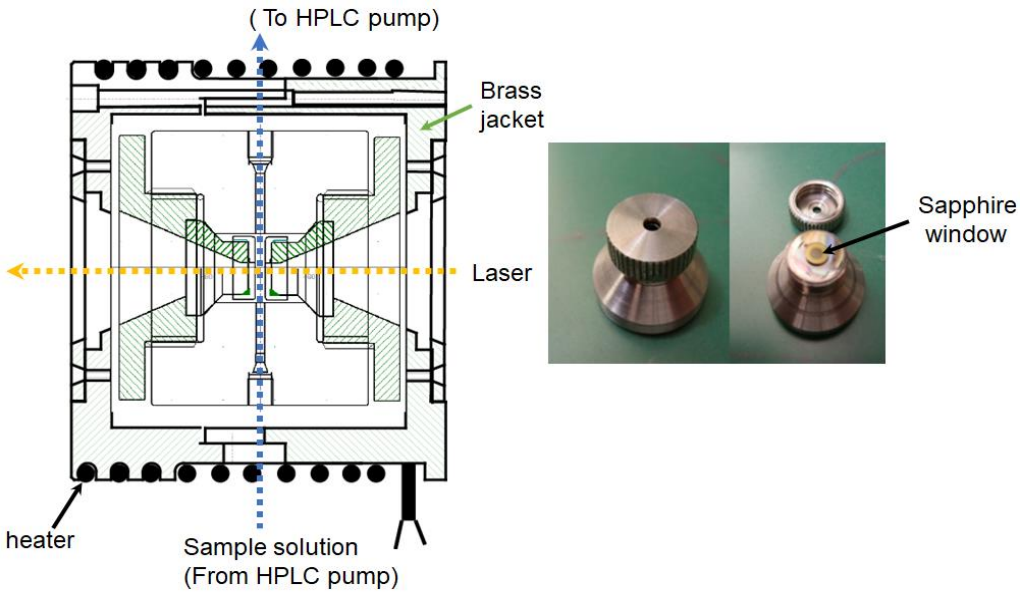

Figure 2-3. Cross section of the cell for high-pressure measurement and pictures of optical

Figure 2-4 shows setup for the time-resolved fluorescence spectrum measurement. An

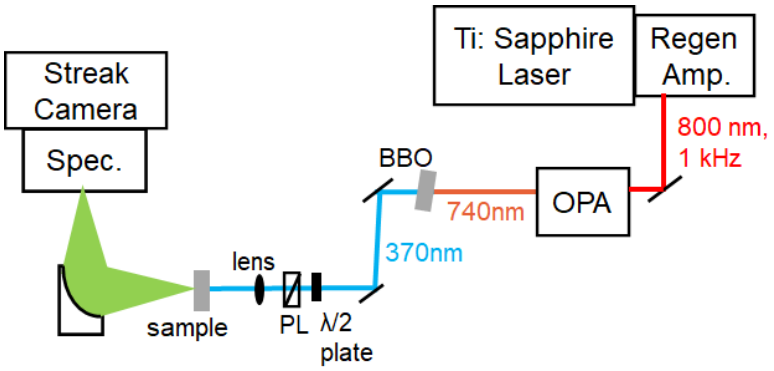

Figure 2-4. Systematic illustration of time-resolved fluorescence spectrum. (PL: polarizer)

excitation light of 800 nm from an amplified Ti: sapphire laser (Spectra physics, Spitfire Xp) was converted to 370 nm by an OPA (Spectra physics, TOPAS-800C) and a BBO crystal. Fluorescence from a sample solution in a 1 mm path length quartz cell was detected by a streak camera (Hamamatsu, C4334) attached to a spectrometer (Princeton Instruments, Acton SP2150). The color-sensitivity and the time shift were corrected as was done previously.[10]

For the measurements under ambient conditions (294 K, 0.1 MPa), the sample solution was enclosed in a quartz cell with a 1 mm path length. For the measurements under high-temperature and high-pressure conditions, the cell described above was used and the sample solution was passed at a speed of 1.5 mL/min. The steady-state fluorescence and absorption spectra under ambient conditions were measured using the Shimadzu UV-2400PC and JASCO FP-6500 instruments, respectively.

2.3. Results

2.3.1. Absorption Spectra and Steady-State Fluorescence of DCN2

Figure 2-5 shows absorption spectra of DCN2 in (a) C_nOH (n = 1, 2, 3, 4, 5, 6, 8, and 10) under ambient conditions and (b) C_1OH at the 30 MPa isobar and different temperatures from 294 to 523 K. For both cases, the spectral shape is identical to that of ROH reported previously, indicating that PT does not occur at the electronic ground state. The peak position of the lowest transition energy in C_nOH slightly shifts to a long wavelength as the number of alkyl carbons increases. In the case of C1OH at high-temperature at 30 MPa isobar, the peak position shift to a short wavelength at elevated temperatures. The peak positions of the $S_1 \leftarrow S_0$ transition of DCN2 in C_nOH and C_1OH at high temperature and pressure are summarized in Table 2-1. This peak shift is discussed from the point of view of the solvent static parameter, in section 2-4.

Figure 2-6 shows the steady-state fluorescence spectrum of DCN2 in C_nOH under

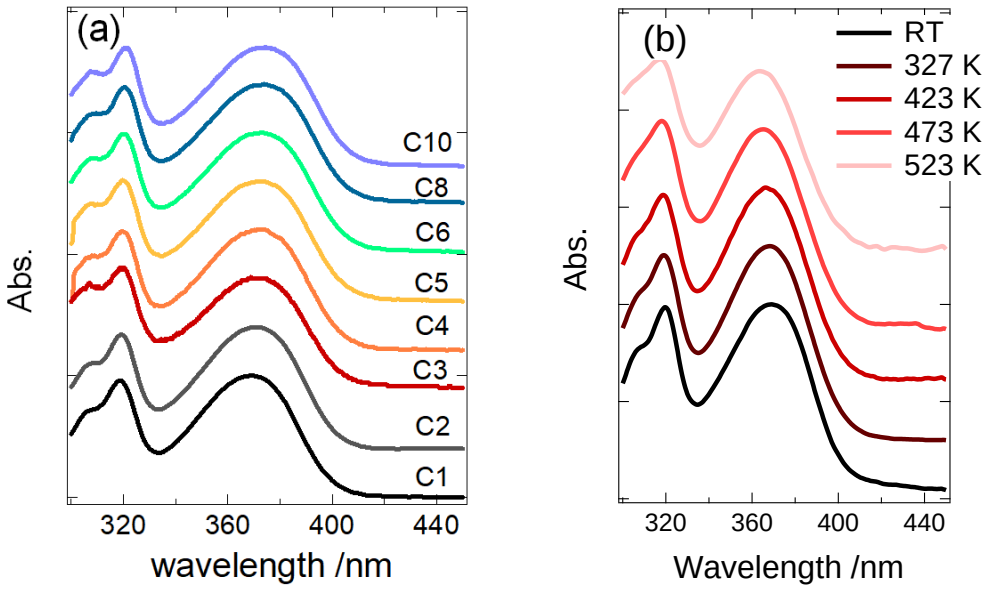

Figure 2-5. Absorption spectrum of DCN2 in (a) n-alcohols at ambient conditions and (b) C_1OH at 30 MPa isobar at different temperatures from room temperature (294 K) to 523 K. Each spectrum is vertically shifted differently for the clarity.

ambient conditions. The band around 450 nm is the fluorescence from ROH* and that around 600 nm is the fluorescence from RO^-* generated by ESPT. Fluorescence from RO^-* was observed in all the C_nOH. It is apparent that the fluorescence intensity of RO^-* decreases as the alkyl chain length increases. In Table 2-1, the apparent peak positions of ROH* and RO^-* are summarized, together with the results in high-temperature and high-pressure methanol. The fluorescence peak positions in C_1OH at high temperature and pressure were determined by averaging the time-profile data for different delay times (the fitting details are described in section 2.3.2).

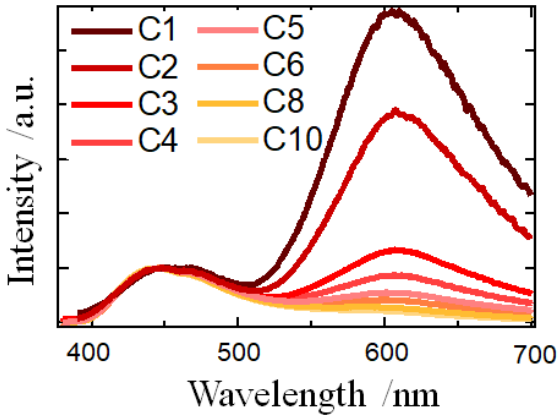

Figure 2-6. Steady-state fluorescence spectrum of DCN2 in n-alcohol under ambient conditions. Each spectrum is normalized at the intensity of the peak position of ROH^*.

Table 2-1. Peak position of DCN2 in C_nOH under ambient conditions and in C_1OH at high temperatures and high pressures. $\Delta\nu$ is the Stokes shift calculated from $\nu_{max}^{abs} - \nu_{ROH}^{flu}$ (unit 10^3 cm^{-1}).

n	T / K	P / MPa	ν_{max}^{abs} /10^3 cm^{-1}	ν_{ROH}^{flu} /10^3 cm^{-1}	ν_{RO}^{flu} /10^3 cm^{-1}	$\Delta\nu$ /10^3 cm^{-1}
1	294	0.1	26.88	21.78	16.42	5.10
2	294	0.1	26.81	21.93	16.45	4.88
3	294	0.1	26.75	22.36	16.46	4.39
4	294	0.1	26.7	22.37	16.46	4.33
5	294	0.1	26.67	22.37	16.56	4.30
6	294	0.1	26.63	22.42	16.69	4.21
8	294	0.1	26.66	22.47	17.03	4.19
10	294	0.1	26.57	22.52	–	4.05
1	294	30	27.32	21.7	16.7	5.62
1	373	30	27.36	21.9_9	16.6	5.37
1	423	30	27.42	22.0_2	16.5	5.40
1	473	30	27.55	21.9_5	16.3_7	5.6
1	513	30	–	22.4	16.4_3	–
1	523	30	27.66	–	–	–

2.3.2. Time-Resolved Fluorescence Spectra

Figure 2-7 shows the time-resolved fluorescence spectra of DCN2 in (a) C_1OH, (b) C_2OH, (c) C_4OH, and (d) C_8OH under ambient conditions. The horizontal scale is the wavenumber, and the fluorescence band at higher energy corresponds to that from ROH* (around 22000 cm^{-1}). It is apparent that the spectrum dynamics depend on the number of the alkyl carbons in C_nOH. For (a) C_1OH and (b) C_2OH, the fluorescence band at lower energy (around 17000 cm^{-1}), which corresponds to that from RO^-*, appears at relatively earlier delay times after the photoexcitation. On the other hand, for C_4OH, the fluorescence from RO^-* slowly appears at ~1 ns. The relative intensity of RO^-* to that

of ROH* is low, and the tail of the ROH* fluorescence band overlaps that of RO^-*. For C_8OH, the fluorescence band from RO^-* is not clearly distinguished from the tail of the ROH* band.

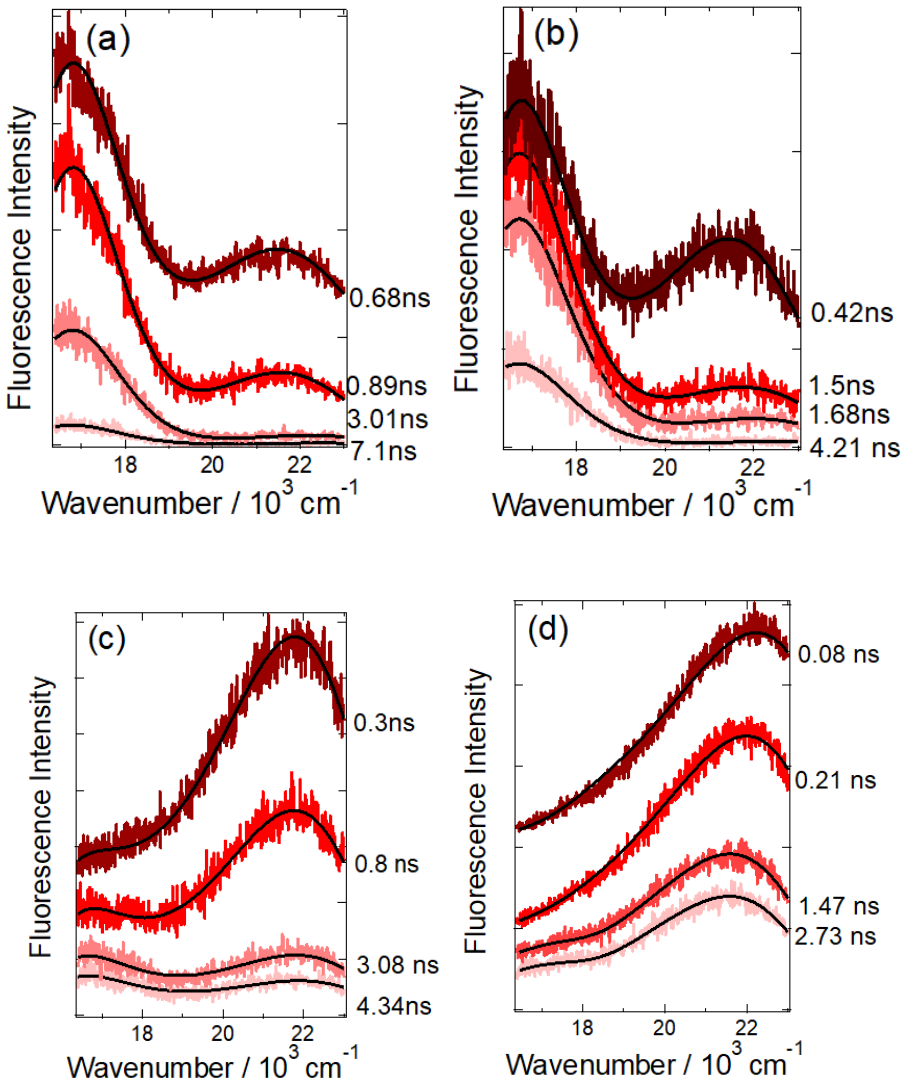

Figure 2-7. Time resolved fluorescence spectrum of DCN2 in (a) C_1OH, (b) C_2OH, (c) C_4OH and (d) C_8OH under ambient conditions. Each spectrum at different delay time is vertically shifted differently for clarity.

Figure 2-8 shows the time-resolved fluorescence spectra of DCN2 in C_1OH at 294 (a), 373 (b), 513 (c), and 543 K (d) and 30 MPa. For C_1OH at 294, 373, and 513 K,

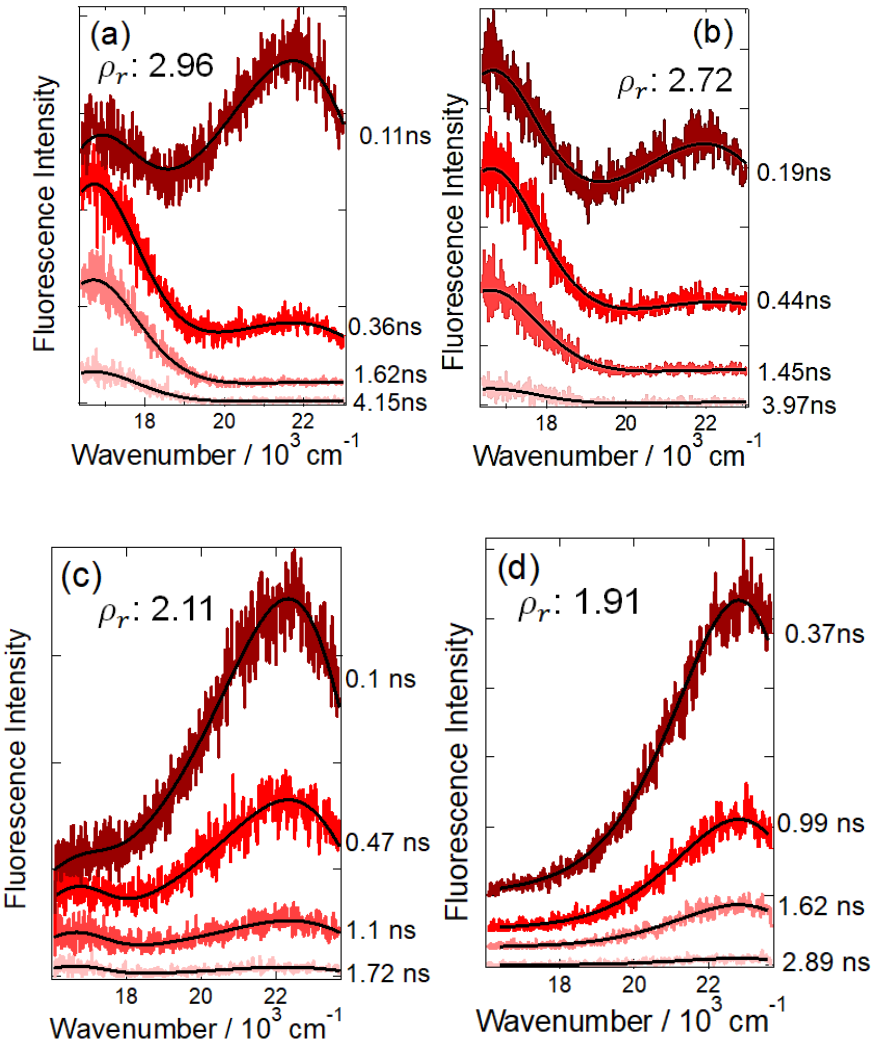

Figure 2-8. Time resolved fluorescence spectrum of DCN2 in C_1OH at 30 MPa and (a) room temperature (294 K), (b) 373 K, (c) 513 K and (d) 543K. Each spectrum at different delay time is vertically shifted differently for clarity.

fluorescence from both ROH* and RO^-* were observed. Upon excitation, the fluorescence from ROH* immediately appears, and the band from RO^-* gradually rises in the several nanoseconds after the excitation. At 294 and 373 K, the fluorescence from RO^-* appears rapidly, at ~0.2 ns. From 294 to 373 K, the fluorescence intensity of RO^-* increases with the temperature, indicating that the ESPT yield increases with the temperature. On the other hand, from 373 to 543 K, the fluorescence intensity of RO^-* decreases with an increase in the temperature. At 543 K, only the fluorescence band from

ROH* was observed, and no other species was detected over time, indicating that ESPT did not occur. In the previous study on 5CN2 in supercritical water, a unique fluorescence band which is ascribed to the solvent separated complex is observed near the critical density.[7] In our study, however, no such unique band was observed within the temperature and pressure range we surveyed.

To extract the time profile of each species (ROH* and RO^-*), the spectrum at different delay times was fitted with a sum of the log-normal functions as follows:

$$I_{\mathrm{fl}}(\nu) = \sum_{i=1}^{2} h_i \times \begin{cases} \exp[-\ln(2)\{\ln(1+\alpha_i)/\gamma_i\}^2] & \alpha_i > -1 \\ 0 & \alpha_i \leq -1 \end{cases} \qquad (2.1)$$

The subscript, *i*, denotes the chemical species, ROH* and RO^-*. For the spectra under the conditions where two fluorescence bands (ROH* and RO^-*) were observed, we first fitted the spectra for the long delay time where fluorescence from RO^-* dominates. Then, the parameters related to RO^-*, except h_{RO-*}, were determined by averaging the values obtained using the fit, assuming that the spectral shape was independent of the delay time. Using these parameters of RO^-*, the spectrum at the early delay time, where fluorescence from ROH* dominates, was simulated. Then, the parameters of ROH* were fixed at the averaged values, except h_{ROH*} and $\tilde{\nu}_{ROH*}$. Each spectrum under the same experimental conditions was simulated using the same fitting parameters, except the time- dependent parameters: $\tilde{\nu}_{ROH*}$, h_{ROH*}, and h_{RO-*}. The black solid lines in Figures 2-7 and 2-8 indicate the fitting results. As shown in the figures, the spectrum simulation works well.

Figure 2-9 shows the time profiles of the populations of ROH*and RO^-* in C_1OH under various thermal conditions. As shown in the figure, the time profile of ROH* decays with more than two different time constants, and that of RO^-* shows rise and decay behavior. As the fastest decay time of ROH* in Figure 2-9 (a) 373 K, 30 MPa and

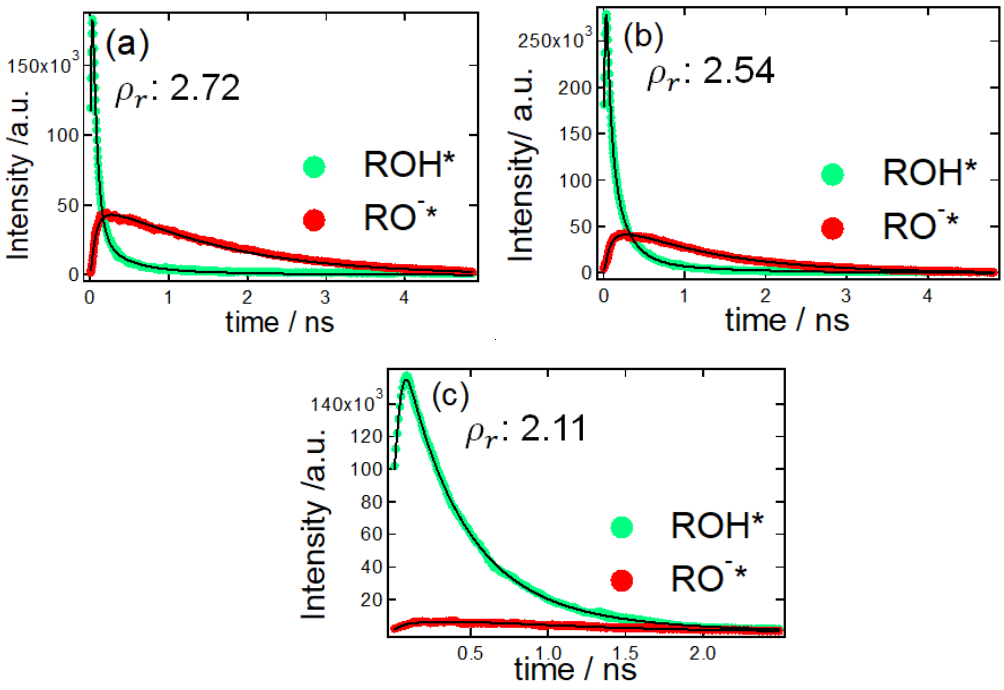

Figure 2-9. Time profile of the fluorescence intensity of DCN2 in C_1OH (a) 373 K, (b) 423 K and (c) 513 K. The black lines in each profile represent the fitting results by a multi-exponential function.

(b) 423 K, 30 MPa is similar to the rise of RO^-*, ESPT occurs in this time constant, at about sub nanoseconds. There seems to be another rise component of RO^-* that also corresponds to the reaction path to generate RO^-*. Finally, after equilibrium is attained, ROH* and RO^-* decay with a time constant of several nanoseconds. Although the fluorescence intensity of RO^-* is low at elevated temperatures (Figure 2-9 (c), 513 K, 30 MPa), almost the same trend might be applicable. To extract the kinetics of each population, the time profile of the decay process was simulated using a multi-exponential function as follows:

$$I_i(\mathrm{t}) = A_1 e^{-k_1 t} + A_2 e^{-k_2 t} + A_3 e^{-k_3 t} \qquad (2.2)$$

where I_i(t) is the time profile of the integrated fluorescence intensity of the molecular species *i* (ROH* or RO−*). In the fitting, eq (2.2) was convoluted with the system response function, assuming the Gaussian response function. For DCN2 in C_1OH at high

temperature and pressure, we first fitted the time profiles of ROH* and RO^-* simultaneously with tri-exponential functions, by linking the two faster time constants that reflect the PT dynamics. Since the population of ROH* is thought to exist for a longer time than that of RO^-*, we assumed that ROH* and RO^-* have different decay time constants (slowest time constant) to relax to the ground state. For C_nOH under ambient conditions, nearly the same procedure was applied. The time profiles of DCN2 in C_nOH, and examples of the fitting results are shown in the Appendix A2 (Figure A1). The PT rate constants obtained by the multiexponential function are summarized Appendix A2. (Tables A1 and A2)

For PT in C_nOH and C_1OH, the fast decay of ROH* or the fast rise of RO^-* in several nanoseconds are well-expressed by a double exponential function. However, the slowest decays of ROH* and RO^-* could not be simulated using an exponential function. We found a deviation from the experimental obtained time-profile in the long time; calculation results predicted smaller yield of ROH* than the experimental one. This deviation suggests that there is a back-PT reaction by which ROH* form is regenerated.[3] Agmon et al. studied the fluorescence dynamics of 5-cyano-2-naphthol in various solvents, using time-resolved fluorescence measurements, and analyzed the spectrum data by considering the two-step PT reaction scheme (see Scheme 2-1).

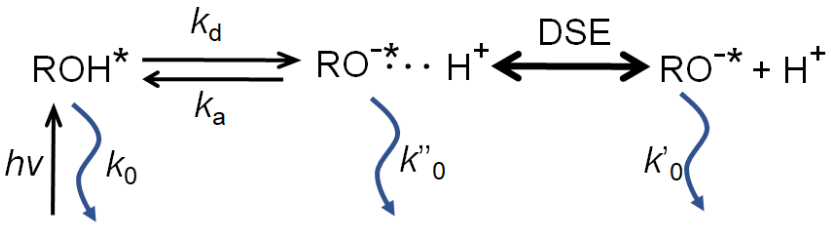

Scheme 2-1. ESPT scheme considering the diffusion process in the Coulomb field leading to back PT reaction to repopulate ROH*.

In this scheme, a proton is dissociated from an excited-state acid ROH* to produce a

geminate ion pair $RO^{-}{*}\cdots H^{+}$, which results in either the recombination or dissociation process to produce ROH* or $RO^{-}{*}$ by diffusional motion, respectively. This diffusional process is modeled by the Debye−Smoluchowski theory. In our cases, it is probable that the fast diffusional process at high temperatures affects the population kinetics. To elucidate this point, we tried to simulate the experimental time profile using numerical solutions of the time-dependent Debye−Smoluchowski equation (DSE), by applying the spherically symmetric diffusion problem (SSDP) provided by Agmon et al.

Herein, we briefly explain the model used for the calculation. In scheme 2-1, proton dissociation from the excited acid (ROH*) produces a geminate ion pair ($RO^{-}{*}\cdots H^{+}$) separated by a contact radius (a /Å) with rate constants k_d. This ion pair either recombines to generate ROH* with rate constant k_a (recombination process) or separates to form $RO^{-}{*}$ by diffusion. The diffusional process of ion pair is modeled by a transient numerical solution of the DSE.

$$\frac{\partial}{\partial \mathrm{t}} p(\mathrm{ROH}^{*}, t) = 4\pi \int W_a(r) p(\mathrm{RO}^{-*}(r), t) r^2 dr - (k_d + k_0) p(\mathrm{ROH}^{*}, t) \tag{2.3}$$

$$\begin{aligned} \frac{\partial}{\partial \mathrm{t}} p(\mathrm{RO}^{-*}(r), t) \\ = r^{-2} \frac{\partial}{\partial r} D_{\mathrm{RO+H}} r^2 e^{-V(r)} \frac{\partial}{\partial r} e^{V(r)} p(\mathrm{RO}^{-*}(r), t) - [W_a(r) \\ + W_q(r) + k'_0] p(\mathrm{RO}^{-*}(r), t) + W_d(r) p(\mathrm{ROH}^{*}, t) \end{aligned} \tag{2.4}$$

where p(ROH*, t) represents the probability of finding the excited acid at t, after excitation, and $p(RO^{-}{*}(r), t)$ is that of finding the anion at $r > a$. $D_{RO+H} = D_{H^+} + D_{RO^-}$ is the mutual diffusion coefficient of the proton and base, and $V(r)$ is the Coulomb attractive potential between the excited base and proton.

$$V(\mathrm{r}) = -R_{\mathrm{D}}/r \tag{2.5}$$

R_{D} is the Debye radius which is given by eq (2.6)

$$R_{\mathrm{D}} \equiv |z_1 z_2| e^2/(k_B T \varepsilon) \tag{2.6}$$

z_1 and z_2 are the charges of the proton and RO^{-}*, respectively, and ε is the static dielectiric constant. In eqs (2.3) and (2.4), the W_{d}, W_{a}, and W_{q} terms represent the decay processes that occur when RO^{-}* and H^{+} are within the contact radius a. W_{d}, W_{a}, and W_{q} indicate the proton dissociation process (k_{d}), proton association process (k_{a}) and quenching of the geminate ion pair by protons (k_{q}), respectively. We assumed the delta function of these processes, as in the case of earlier study[3]:

$$W_{\mathrm{i}}(r) = \frac{k_{\mathrm{i}}\delta(r-a)}{4\pi a^2} \tag{2.7}$$

where the subscript i represents d, a, or q.

To solve the equations numerically, several parameters were determined. First, the dielectric constant of C_1OH under various thermal conditions were obtained via the interpolation of the reference data[11] (see Appendix A3.1). Using the dielectric constants, we determined the Debye radius (R_{D}) defined by eq (3.6). The mutual diffusion coefficients $D_{\mathrm{RO+H}}$ of the base (RO^{-*}) and geminate proton under the 30 MPa isobar were also estimated using empirical relations. A detailed procedure to obtain the $D_{\mathrm{RO+H}}$ is described in the Appendix A3.2. The non-reactional decay of RO^{-}* (k'_0) was set to the experimentally determined values (k_3 in Table A1). We fixed the value of the non-reactive decay of ROH* (k_0) using the fluorescence decay rate of methoxy-analogues of DCN2 (5,8-dicyano-methoxynaphthalene) (k_0 = 0.1 ns^{-1}) in C_1OH under ambient conditions, which does not undergo a reaction process at the excited states, as was done in an earlier study.[3] We assumed that this rate constant was independent of the thermal condition of C_1OH, and adopted it for the non-reactional decay of ROH* for all the thermal conditions. The dissociation rate constant (k_{d}) was also set to the experimentally determined value (k_1) in Table A1. The initial distribution of ROH* and RO^{-}* was set to 1 and 0,

Table 2-2. Dielectric constant ε of C_1OH at 30 MPa isobar from 294 K to 513 K, Debye radius R_D between RO^-* and H^+, and mutual diffusion coefficient of RO^-* and H^+. Numerical solution was conducted by varying recombination rate κ_r with the proton dissociation rate constant k_d as a fixed parameter. The details to determine the D_{RO+H} is described in Appendix. Recombination rate is defined by $\kappa_r = k_a/4\pi a^2$.

T /K	P /MPa	ε	R_D / Å	D_{RO+H} / 10^{-5} cm^2 s^{-1}	k_d/ns^{-1}	κ_r/ Å ns^{-1}	pK_a*
294	30	31.4	15.2	2.56	14.3	10	0.40
373	30	22.8	16.6	7.09	18.5	33	0.92
423	30	17.7	18.8	12.0	16.5	40	1.23
473	30	12.8	23.2	19.1	14.5	62	1.82
513	30	9.2	29.9	26.6	3.07	7.5	2.11

respectively. The contact radius a was set to the typical literature value, 5.5 Å.[3] These parameters for the SSDP calculations are summarized in Table 2-2. By varying the recombination rate constants κ_r ($= k_a/4\pi a^2$), the recombination and survival probabilities of the geminate ion pair were solved in the time range from 0.01 to 10 ns, and compared with the experimentally obtained time profiles of ROH* and RO^-*. Although the quenching of the geminate ion pair by protons was also considered in the earlier study, we did not assume that path because the survival time profile without considering the quenching process sufficiently simulated the experimentally obtained decay profile of RO^-*.

Examples of the fitting based on the DSE model, using the program proposed by Agmon et al.,[12] are shown in Appendix A3.3 (Figure A4). Since the numerically obtained curves (black curves in Figure A4) well-simulated the experimentally obtained profiles (blue circles in Figure A4), we confirmed that the fastest time constant from the experiment (k_1, in Table A1) corresponded to the proton dissociation rate (k_d). In Table 2-2, the numerically obtained recombination rate κ_r and pK_a* values are summarized.

pK_a* was calculated using eq (2.8),[3]

$$\mathrm{p}K_\mathrm{a}^* = -\log\frac{10^{27}k_\mathrm{d}\exp(-R_\mathrm{D}/a)}{k_\mathrm{a}N_\mathrm{A}} \quad (2.8)$$

where N_A is Avogadro's number.

We also numerically solved the DSE equation for the PT in C_nOH under ambient conditions, and confirmed that the experimentally obtained profile of ROH* and RO^-* were well-simulated by the same model described above. In some case, for C_5OH, C_6OH and C_8OH, the k'_0 was adjusted to adequately fit the experimentally obtained profile. The parameters for the calculation, the recombination rate κ_r and the calculated pK_a* value in C_nOH, are summarized in Table 2-3. Examples of the fitting using the DSE model[12] are presented in Figure A5.

Table 2-3. Dielectric constant ε of C_nOH under ambient conditions, Debye radius R_D between RO^-* and H^+, and mutual diffusion coefficient of RO^-* and H^+ in C_nOH. Numerical solution was conducted by varying recombination rate κ_r with the proton dissociation rate constant k_d as a fixed parameter. The details to determine D_{RO+H} is described in Appendix A3. Recombination rate is defined by $\kappa_r = k_a/4\pi a^2$.

n	ε	R_D / Å	D_{RO+H} / 10^{-5} cm^2 s^{-1}	k_d/ns^{-1}	κ_r/ Å ns^{-1}	pK_a*
1	27.8	17.2	2.79	14.5	11	0.60
2	24.6	19.5	1.26	12.9	14	0.93
3	20.5	23.4	0.63	9.84	15	1.39
4	17.5	27.4	0.47	6.89	17	1.92
5	13.9	34.5	0.35	5.23	8.3	2.28
6	13.3	36.0	0.25	2.65	5	2.48
8	9.82	48.8	0.15	2.02	1.6	3.11

As shown in Table 2-2, the κ_r increases with temperature except for the highest temperature. The proton dissociation rate (k_d in Table 2-2) shows a unique temperature dependence. In the range 294–373 K, the k_d increases with temperature (Arrhenius

behavior), whereas it decreases with the increase in the temperature in the range 373–513 K. In the case of 5CN2 in supercritical water, the PT rate monotonically decreases with decreasing density.[7] ESPT was observed for ε = 23, and from ε = 17.1 to 11.4, the crossover of the PT and the formation of solvation separated complex was observed. In the present case, we observe PT in the solvent condition with lower dielectric constant (ε = 9.2) due to the higher acidity of DCN2. The non-Arrhenius behavior of DCN2 at high temperatures[13] is discussed in relation with the activation free energy in Section 4.3.

For PT in C_nOH, as shown in Table 2-3, the κ_r increases with the alkyl chain length from C_1OH to C_4OH. On the other hand, it decreases from C_5OH to C_8OH, which may reflect the increase in the HB basicity for longer-chain alcohols. The dramatical decrease of κ_r in the low dielectric solvent (methanol at 513 K and 30MPa, in C_6OH and C_8OH) is related to the competing solvation effects (dipolar solvation and hydrogen-bond donating) which will be discussed for k_d and pK_a* in Sec. 2.4. When focusing the pK_a* value in Table 2-2 and 2-3, it increases with decreasing k_d. This behavior is consistent with the previous report by Solntsev et. al.[3] in which k_d of mono-cyano naphthol (5CN2, pK_a* (in water): – 0.75) in various solvent decreases with an increase in the pK_a* value.

2.4. Discussion

2.4.1. Effect of Solvation Energy on Electronic State of DCN2

Before the discussion on the ESPT dynamics, we herein review the static solvent effect on the electronic state of DCN2. Since the PT reaction is driven by the solute-solvent interaction, it is important to consider the equilibrium states of the solutes when they are surrounded by solvents. Based on the analysis of the absorption spectrum of DCN2, we discuss how the electronic states of DCN2 are affected by the interactions with various alcohols.

As described in section 2.3.1, the peak position of the absorption spectrum for C_nOH under ambient conditions (Figure 2-5 (a)) shifts to a lower energy with an increase in the alkyl chain length. In the spectrum in C_1OH at high temperature at 30 MPa isobar, the peak position shows the higher-energy shift with an increase in the temperature. Since the absorption band shift reflects the change in the transition energy of ROH by the solute-solvent interaction, we correlate the peak shift with the empirical solvent polarity scale (E_T^N) and hydrogen bond acceptance parameter (β^R, the superscript R indicates that the parameters were determined using Raman spectroscopy). Since the E_T^N values for C_1OH at high temperature and pressure were not available in the literature, we determined them by the absorption peak shift of Reichardt's dye, which are summarized in Appendix A4 (Tables A3 and A4). E_T^N of C_1OH at high temperature and pressure almost linearly correlates with the solvent density (see Figure A6 (b)). Although, conventionally, β values are determined from the absorption spectrum of *p*-nitroaniline and *N, N*-diethyl-*p*-nitroaniline, in this study, we determined β using the Raman shift of the NH_2 stretching vibration of 4-aminobenzene (ABN; ν_{NH2}),[25] considering that the Raman shift of NH_2 stretching band directly reflects the hydrogen bonding between the solute and solvent. By

The procedure to estimate the β^R using the Raman spectrum of ABN in C_nOH under ambient conditions, and C_1OH at 30 MPa isobar between 294 and 543 K, is described in the Appendix A4.2. The obtained β^R values are summarized in Tables A3 and A4. The correlations of β^R with the number of the alkyl carbons in C_nOH and the reduced density of high temperature and high-pressure C_1OH are shown in Figure A8.

Among the several parameters we tested, β^R is the best parameter that gives a linear correlation with the spectral shift. Figure 2-10 shows the plot of the absorption peak position against β^R. The β^R value shows a good correlation with the peak position of the absorption spectrum of ROH. Regardless of the thermal conditions of the solvent, the peak position shifts to a lower energy as the β^R increases, indicating that the surrounding alcohols stabilize the electronic excited state of the normal form of DCN2 more than the ground state by the formation of HB (ROH···OHS (S represents solvent)). The values of the Stokes shift in Table 2-1 also show the similar linear correlation. Since the electronic charge distribution of DCN2 is more polar in the excited states than in the ground state, with the

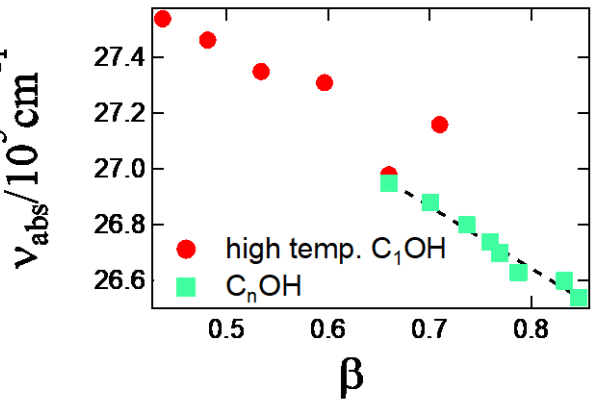

Figure 2-10. Correlation between the peak position of absorption spectrum (ν_{Abs}) vs hydrogen bonding basicity of the solvent. Green squares are results in n-alcohols under ambient conditions, and red circles represent the results in C_1OH at high temperature and pressure.

negative charge localized on the O atom, the stabilization of ROH by the HB basicity is considered to be more significant in the excited states than in the ground state. This energy shift might lead to a decrease in the energy gap between ROH* and RO^{-}*, that is, the free energy gap for the ESPT reaction.

The correlation of the spectral shift of cyano-naphthols with β has been already indicated by Solntsev et al.[3] In their report, the emission peak position of 5CN2 excluding the effect of α of protic solvents shows a linear correlation with β. They also indicated that the π* value is not successful to make a correlation and that the emission band of RO^{-}* is correlated with α if the band position in hydrogen-bonding solvents are compared with non-hydrogen-bonding solvents. In the present work, we tried to correlate the fluorescence band shift of ROH* with other solvent parameters, but no good linear correlation was obtained.

Figure A9 (Appendix A5) shows the plot of the peak position of the absorption spectrum of DCN2 against the E_T^N value. For high-temperature and high-pressure C_1OH, the absorption peak position shifts to a lower energy with an increase in the E_T^N value, whereas for C_nOH under ambient conditions, it shows a slight blue shift when the E_T^N value is high. We also tried to correlate the fluorescence band shift of RO^{-}* with hydrogen-bonding acidity (α), but there was no meaningful correlation within the solvents we studied. From these results, we concluded that the stabilization of ROH* by HB with alcohols has a large influence on the occurrence of ESPT.

2.4.2. Effect of Solvation Dynamics on ESPT kinetics

PT dynamics have often been discussed in relation to the charge transfer or torsional motion of solutes before the PT. In the case of PT in the excited states, these processes are affected by solvent reorganization upon excitation. In this section, solvation dynamics

upon the photoexcitation is discussed by the dynamic spectrum shift of ROH* in C_nOH. Figure A10 (Appendix A5) shows the time profiles of the fluorescence peak position of ROH* in C_nOH under ambient conditions. In all the cases, the peak position of ROH* shows a red shift with time, which indicates that dynamic solvent reorganization around ROH* occurs within the lifetime of the excited states. By fitting the time-resolved spectrum to log-normal function as described in section 2.3.2, we extracted the time-profiles of the fluorescence peak position of ROH* in C_nOH as shown in Figure A10. The time profiles in various solvent were simulated with exponential function, and time constants for the spectrum shift were determined. In C_1OH, C_2OH, and C_3OH, time-profiles were fitted with a single exponential function, and those in C_4OH, C_5OH, C_6OH, C_8OH, and $C_{10}OH$ were simulated using a double exponential function (represented by black solid line Figure A10). In Table 2-4, the time constants of the solvation are summarized, along with the viscosity of C_nOH.[14] For C_nOH (n = 4, 5, 6, 8, and 10), the solvent relaxation time is obtained using the weighted averaging of the two time-constants. Since the time resolution of the streak camera is ~30 ps and faster solvation dynamics

Table 2-4. Solvation relaxation times of C_nOH around DCN2 under ambient conditions together with the viscosity of the solvent. In the case of n = 4, 5, 6, 8 and 10, τ_s is obtained by weighted average of two time-constants.

n	η/ mPa s	τ_1/ ns	τ_2/ ns	A_1	A_2	τ_s/ ns	τ^{ref} / ns
1	0.58	0.01	–			0.01	0.005
2	1.15	0.04	–			0.04	0.016
3	2.16	0.05	–			0.05	0.026
4	2.85	0.03	0.13	1	0.89	0.07	0.063
5	3.76	0.07	0.22	1	0.69	0.13	0.103
6	5.18	0.11	0.31	1	0.76	0.20	-
8	8.9	0.14	0.51	1	1.15	0.34	-
10	12.8	0.17	0.81	1	1.21	0.52	0.245

might be missed. As shown in Figure A11 (Appendix A5), the solvation time of C_nOH monotonically increases with the viscosity of the solvent, which might be because it takes a longer time to orient the alkyl chain to form HB as the alkyl chain length increases. The time constant for solvent reorganization estimated here are compared to those measured for non-PT solute, coumarin153 represented as τ^{ref} in Table 2-4. Horing et al. shows that experimentally determined solvent relaxation time of C_nOH shows good coincidence with the dielectric relaxation time of the pure solvent.[15] The averaged solvation time of C_nOH reported in their paper is almost consistent with the value we obtained although in shorter alcohols (C_1OH, C_2OH, and C_3OH), the solvent relaxation time is about 2 times slower than the reference value partially because we missed the very fast component due to the limitation of the time response of the streak camera. However, the slowest component of the solvation dynamics of ours are mostly slower than those in ref.60, which may suggest the contribution from the solute−solvent hydrogen-bonding.

In Figure 2-11, the rate constant of the solvation reorganization ($k_s = 1/\tau_s$) and that of the proton dissociation (k_d) are plotted against the number of alkyl carbons in C_nOH. When comparing the rates for the solvation dynamics with those of the PT, in all C_nOH, the PT dissociation rate is slower than that of the solvation dynamics. This indicates that ESPT mostly occurs after the solvent relaxation around the ROH* is completed. Our result is consistent with previous studies on the pressure effect on the PT dynamics.[16,17] In the report by the group of Huppert about the effect of pressure on the proton transfer dynamics of DCN2 in methanol, ethanol, and propanol, they found that PT reaction rate constants show similar dependence on the pressure (from atmosphere to 2.2 GPa) in each alcohol. The pressure effect on the rate constant is explained by the opposite dependence of the rate constants for solvent coordinate and proton coordinate on the

pressure. Comparing the pressure region from atmosphere to ~1 GPa that corresponds to our experimental condition, the solvation rate is much faster than the proton dissociation rate, which agrees with our results.

When analyzed in detail, there is a difference in the conditions between shorter alkyl alcohols and longer ones. For the longer alcohols (C_5OH, C_6OH, and C_8OH), the difference between the k_{PT} and k_s is small, suggesting that the PT process may be affected by the solvation dynamics. On the other hand, the shorter alkyl alcohols (C_1OH, C_2OH, C_3OH, and C_4OH) show a large difference between the k_{PT} and k_s. This indicates that solvent reorganization is completed much faster than the proton dissociation process, and the PT reaction is not be affected by the dynamic solvent reorganization. In this case, it is considered that the static factor of the solvent that lowers the activation free energy $\Delta G^{\neq}$ of the PT might drive the ESPT.

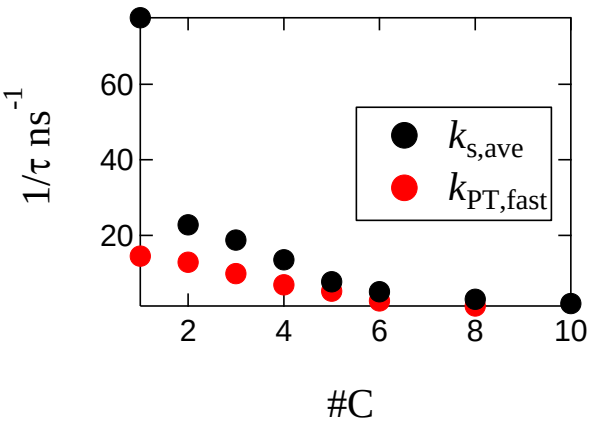

Figure 2-11. Rate constants of proton dissociation (k_d) and solvation dynamics (k_s) vs the number of carbon atoms in C_nOH. For $C_{10}OH$, we could not determine the proton dissociation rate.

2.4.3. Correlation of Proton Dissociation Rate with Solvation Energy

As discussed in the previous section, the proton dissociation rate is considered to be influenced by the activation free energy. Generally, the rate constant is related to the

activation free energy, as shown in the following equation.

$$\ln k = \ln A + (-\Delta G^{\neq}/RT) \tag{2.9}$$

where $\ln A$ is the frequency factor and R is the gas constant. We tried to model the $\Delta G^{\neq}$ using the solvent parameters that linear solvation energy relationships (LSERs) suggested by Kamlet and Taft[18], $\Delta G^{\neq}$can be modeled as follows:

$$\Delta G^{\neq} = \Delta G^{\neq}_{\mathrm{C_1OH}} + b\left(\pi^* - \pi^*_{\mathrm{C_1OH}}\right) + c(\beta^R - \beta^R_{\mathrm{C_1OH}}) \tag{2.10}$$

We set the reaction rate in C_1OH under ambient conditions as the reference and considered the difference in the activation energy from that. Although the LSERs indicates that the $\Delta G^{\neq}$ is related to three Kamlet−Taft parameters, hydrogen-bonding acidity (α), basicity (β), and dipolarity/polarizability (π*), we assumed that the PT kinetics are controlled by the β^R and π* of the solvent, since the α of the alcohols does not show any meaningful correlations with the proton dissociation rate constants. The difference in the rate constant from the standard state is expressed as follows:

$$\ln k_{\mathrm{d}} - \ln k_{\mathrm{d,C_1OH}} = -\Delta G^{\neq}/RT + \Delta G^{\neq}_{\mathrm{C_1OH}}/RT_0 \tag{2.11}$$

where $k_{\mathrm{d,C_1OH}}$ is the proton dissociation rate constant of DCN2 in C_1OH under ambient conditions, and T_0 is the room temperature (294 K). Substituting eq (2.11) with eq (2.10), the ratio of the proton dissociation rate constants in various alcohols to that in the reference state is represented by eq (2.12),

$$\ln \frac{k_{\mathrm{d}}(T, \pi^*, \beta^R)}{k_{\mathrm{d,C_1OH}}} = \frac{1}{RT}\left\{\Delta G^{\neq}_{\mathrm{C_1OH}}\left(\frac{T}{T_0} - 1\right) - b\left(\pi^* - \pi^*_{\mathrm{C_1OH}}\right) - c(\beta^R - \beta^R_{\mathrm{C_1OH}})\right\} \tag{2.12}$$

where $\Delta G^{\neq}_{\mathrm{C_1OH}}$ = 2.1 kJ/ mol,[19] $\pi^*_{\mathrm{C_1OH}} = 0.6$[20], and $\beta_{\mathrm{C_1OH}} = 0.66$.[20]

In Figure 2-12, the $\ln(k_{\mathrm{d}}/k_{\mathrm{d,C1OH}})$ determined from the experimentally obtained rate

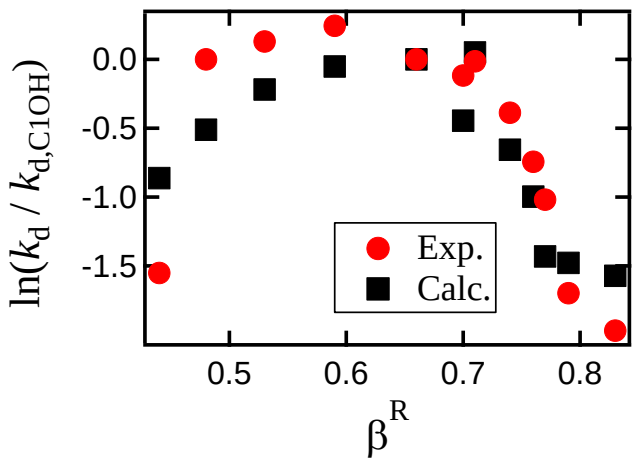

Figure 2-12. Plot of the ratio of proton dissociation rate constants (k_d) of DCN2 in various alcohols and that in C_1OH under ambient conditions against β^R. Red circles represent experimentally obtained values and black squares are numerically determined values. β^R in C_1OH under ambient condition is 0.66.

constants (k_d in Tables 2-2 and 2-3) are plotted against β^R (red circles). By fitting eq (2.12) to this plot, the coefficients b and c were determined. The optimized parameters are b = −14.4 and c =5.7. By substituting obtained value of b and c for eq (2.12), the ratio of the proton dissociation rate constants, $\ln(k_d/k_{d,C1OH})$ was calculated (black squares). It appeared that the experimentally obtained rate constants were simulated using eq (2.12) fairly well, indicating that $\ln(k_d/k_{d,C1OH})$ is well represented by two factors, the solvent polarity and HB basicity. According to the fitting parameters (b and c), the influence of the solvent parameters (π^*, β^R) on the PT kinetics is expected to be different: the solvent dipolarity/polarizability positively correlates with $\ln(k_d/k_{d,C1OH})$, whereas the solvent HB basicity negatively contributes to $\ln(k_d/k_{d,C1OH})$. This is because the π^* stabilizes an ionic species ($RO^{-}{}^{*}\cdots H^{+}$). On the other hand, the β^R plays a role in stabilizing ROH*, as mentioned in section 2.4.1, which indicates the stabilization of the initial states of the PT (see Figure 2-13). Therefore, the PT kinetics are controlled by the concerted effect of π^* and β^R on activation free energy, based on the change of π^*, β^R from the standard point

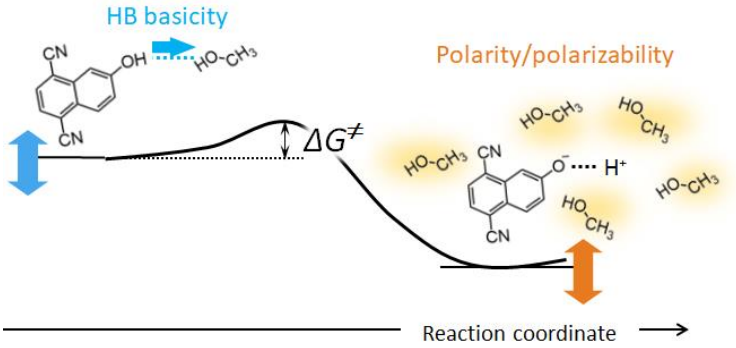

Figure 2-13. PT reaction and the effect of solvent parameters (π*, β^R) on the activation free energy.

(C_1OH at ambient condition). In Figure 2-14, we plot the π* against β^R in all solvents used in this study. The region where β^R value is higher than that of C_1OH under ambient conditions (β^R = 0.66) corresponds to the C_nOH under ambient conditions. β^R increases and π* decrease as the number of alkyl chain length increases. This results in the increase $\Delta G^{\neq}$, and PT rate constants decrease compared with the rate constants in C_1OH at ambient conditions. On the other hand, the region where the β^R is lower than 0.66 corresponds to the PT in high-temperature and high-pressure C_1OH. Both β^R and π* decrease with increasing the temperature from the ambient condition. Since π* decreases more steeply against the solvent density, and the ionic species, RO^-*···H^+ is considered to be located

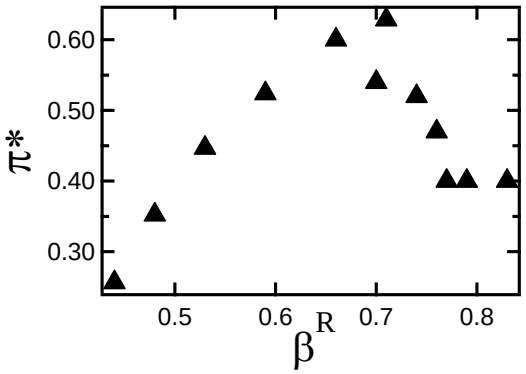

Figure 2-14. π* and β^R of C_1OH at high-temperature and high pressure, and C_nOH at ambient conditions. β^R in C_1OH under ambient condition is 0.66.

in the close of activated state in the PT reaction coordinate, PT rate constants would decrease as increasing temperature.

Of course, $\Delta G^{\neq}$ is expected to be dependent on the other parameter, density and the number of alkyl chain length. In Figure A12, $\Delta G^{\neq}$ is plot against β^{R}. $\Delta G^{\neq}$ has maximum against β^{R}, and the dependence is similar to that of $\ln(k_d/k_{d,C1OH})$. Thus, $\Delta G^{\neq}$ also depends on the Kampet-Taft parameters as is the case for the rate constant $\ln(k_d/k_{d,C1OH})$. We can conclude the change of solvation energy by π^* and β^{R} is the main factor to control the PT rate constant in various alcohol.

Before concluding this section, we herein discuss the pK_a* values shown in Tables 2-2 and 2-3, adopting the same procedure described above. pK_a* is related to the free energy by the following equation.

$$\mathrm{p}K_a^* = -\ \ln K_a^*\ /\ \ln 10 = \Delta G/2.30RT_0 \qquad (2.13)$$

By taking the ratio of the $\ln K_a^*$ in various alcohols and that in C_1OH under ambient conditions, and assuming that the ΔG is modeled based on the LSER defined by eq (2.10), the pK_a* value is represented as follows:

$$\ln\frac{K_a^*(T,\pi^*,\beta^R)}{K_a^{*\mathrm{C_1OH}}} = \frac{1}{RT}\left\{\Delta G_{\mathrm{C_1OH}}\left(\frac{T}{T_0}-1\right) - b'\left(\pi^* - \pi^*_{\mathrm{C_1OH}}\right) - c'(\beta^R - \beta^R_{\mathrm{C_1OH}})\right\} \qquad (2.14)$$

where $\Delta G_{\mathrm{C_1OH}}$ = 3.38 kJ/mol, obtained by substituting pK_a*= 0.6 (pK_a* value of DCN2 in C_1OH under ambient conditions), T_0 = 294 K, and the gas constant R in eq (2.13). The other parameters and coefficients in this equation are the same as those represented in eq (2.12). In Figure 2-15, the $\ln(K_a^*/K_a^{*\mathrm{C_1OH}})$ values are plotted against the β^R values. At first glance, $\ln(K_a^*/K_a^{*\mathrm{C_1OH}})$ has almost the same dependence on the β^R value as the

behavior of $\ln k_{\mathrm{d}}/k_{\mathrm{d,MeOH}}$. By fitting this plot with eq (2.14), the parameters b' and c' were determined to be -52.7 and 6.09, respectively. The black squares in Fig. 2-13 represent the plot of the right side of the eq (2.14) against β^Rvalue using the fitting coefficients, b' and c'. Since the experimentally determined pK_a* values show a good coincidence of the calculated value, $\ln(K_{\mathrm{a}}^*/K_{\mathrm{a}}^{*\mathrm{C_1OH}})$ is well simulated by the two solvation parameters, $\beta^R$and π^*. Similar to the case of the proton dissociation rate, $\ln(K_{\mathrm{a}}^*/K_{\mathrm{a}}^{*\mathrm{C_1OH}})$ shows an increase and a decrease with an increase in β^R. Since the coefficients for π^* and β^R in eq (2.14) have different signs, there is a competing effect of β^R and π^*. In C_nOH under ambient conditions where β^R increases with the number of alkyl carbons, the effect of β^R dominate, which lead to decrease of the ability to dissociate proton. On the other hand, in the case of high temperature and pressure C_1OH where π^* shows a significant decrease with decreasing density, the effect of π^* surpasses that of β^R, which finally decrease the ability to dissociate proton. For $\ln(K_{\mathrm{a}}^*/K_{\mathrm{a}}^{*\mathrm{C_1OH}})$, the contribution of the π^* is much larger than that of β^R. This is reasonable, considering that the stability of the proton-dissociated state is mostly affected

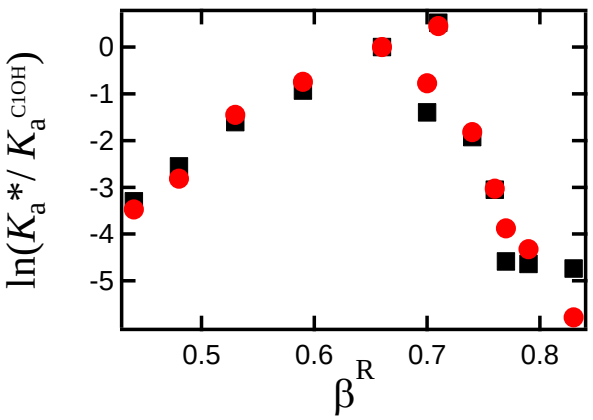

Figure 2-15. Plot of the ratio of proton dissociation constant K_a of DCN2 in various alcohols and that in C_1OH under ambient conditions against β^R. Red circles represent experimentally obtained values and black squares are numerically determined values.

by the polarity of the solvent.

2.5. Conclusions

In this study, we investigated the solute-solvent intermolecular PT between DCN2 and high-temperature and high-pressure (30 MPa isobar between 294 and 543 K) methanol, by measuring the time-resolved fluorescence spectrum. Up to 513 K and 30 MPa, the fluorescence from RO^{-}* was detected, which indicates that the ESPT occurred. At high-temperature and high-pressure, diffusional process of RO^{-}*···H^{+} and back PT reaction couldn't be neglected. The fluorescence time profiles obtained using the global fit to the time-resolved spectrum were analyzed based on the Debye–Smoluchowski diffusional model, where back PT is included as the recombination rate constant, κ_r. We successfully extracted the proton dissociate rate constant, k_d in alcohols at various thermal conditions. PT kinetics were discussed based on the linear solvation energy relationships (LSERs), that relates reaction rate constants with the change in the solvation energy by Kamlet-Taft prameters. We found that PT kinetics was explained by the concerted effect of Kamlet-Taft prameters, hydrogen-bond basicity and polarity to stabilize the initial state of PT (ROH*). It is also noted that the effect of solvation dynamics on the kinetics of PT was not large. In the future, it will be desirable to obtain a more detailed picture using the information obtained from the radial distribution function and reaction free energy, by applying theoretical calculations such as RISM-SCF.

Appendix A

Table of Contents

A1. Synthesis of 5,8-discyano-2-naphthol

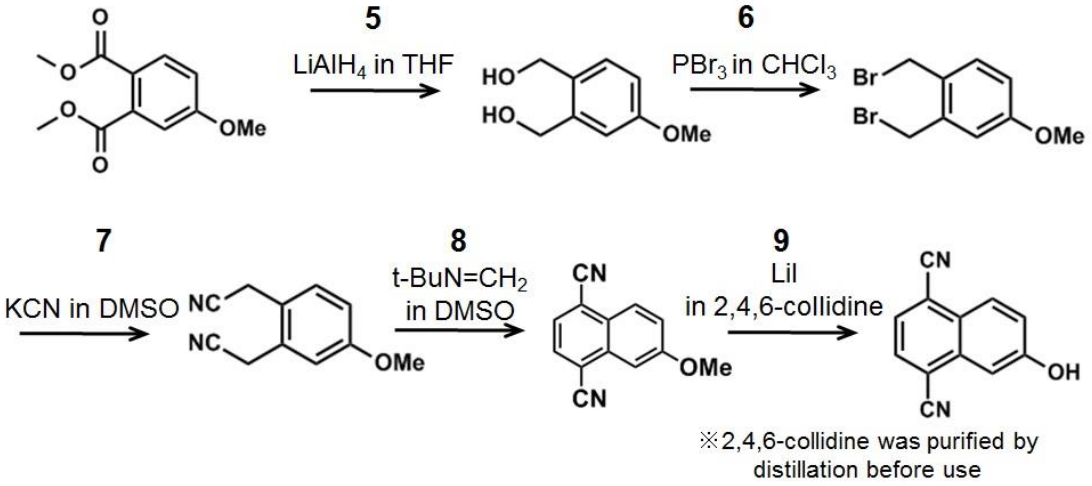

Scheme A1. Synthesis of DCN2. For experimental details, see: ref. 8 (reactions 5–7) and ref. 5 (reactions 8, 9).

A2. Results of the Time-resolved Fluorescence Measurements

A2.1. Time Profile of the Fluorescence Intensity

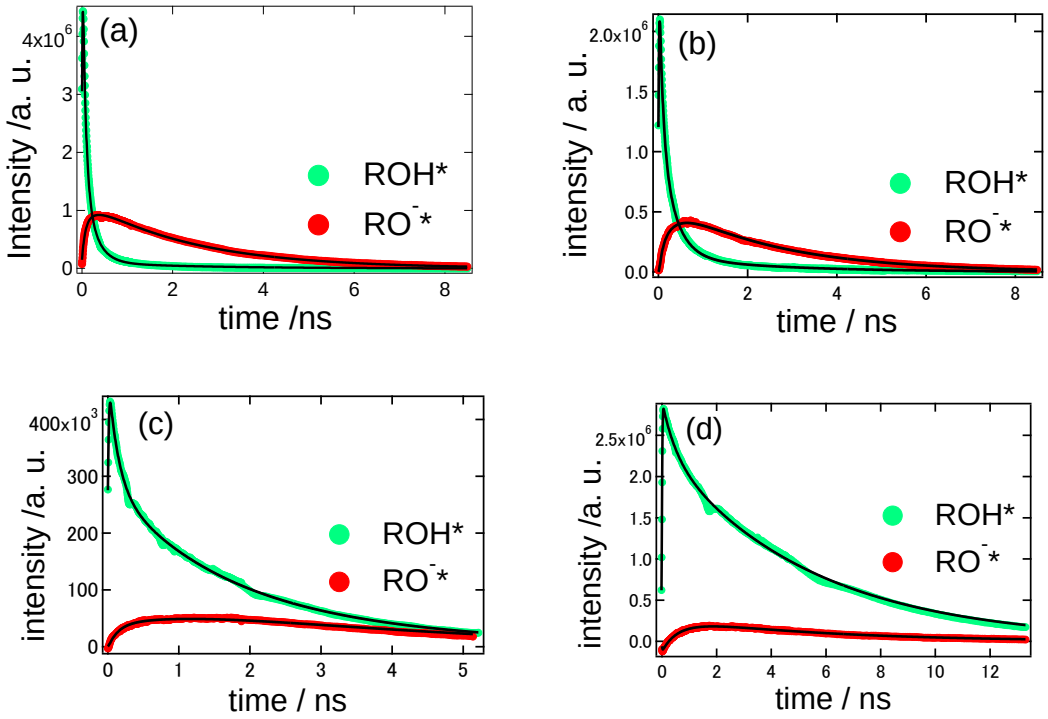

Figure A1. Time-profile of fluorescence intensity of ROH and RO in (a) C_1OH, (b) C_2OH, (c) C_4OH and (d) C_8OH under ambient conditions.

A2.1. Rate Constants of ESPT

Table A1. Rate constants of ESPT of DCN2 in C_1OH along 30 MPa isobar at high temperatures determined by multi-exponential fit of the time profiles of the fluorescence intensity

Temp./K	species	A_1	A_2	A_3	k_1 / ns^{-1}	k_2 / ns^{-1}	k_3 / ns^{-1}
294	ROH*	1	0.69	–	14.3	6.09	
	RO^-*	−0.08	−0.32	0.42			0.51
373	ROH*	1	0.28	0.02	18.5	4.14	
	RO^-*	−0.18	−0.09	0.23			0.69
423	ROH*	1	0.45	0.03	16.5	4.04	
	RO^-*	−0.14	−0.08	0.22			0.79
473	ROH*	1	1.92	0.29	14.5	4.01	
	RO^-*	−0.31	−0.24	0.54			0.95
513	ROH*	1		0.46	3.03	–	
	RO^-*	−0.09		0.12		–	1.14
543	ROH*					1.13	

Table A2. Rate constants of ESPT of DCN2 in C_nOH under ambient conditions determined by multi-exponential fit of the time profiles of the fluorescence intensity.

n	species	A_1	A_2	A_3	k_1 / ns^{-1}	k_2 / ns^{-1}	k_3 / ns^{-1}
1	ROH*	1	0.38		14.5	4.24	
	RO^-*	−0.13	−0.11	0.28			0.43
2	ROH*	1	0.74		12.9	3.11	
	RO^-*	−0.12	−0.22	0.39			0.41
3	ROH*	1	0.83	0.55	9.84	1.63	0.5
	RO^-*	−0.07	−0.33	0.42			0.36
4	ROH*	1	0.19	1.2	6.89	1.05	0.46
	RO^-*	−0.14	−0.38	0.53			0.32
5	ROH*	1	–	1.26	5.23	0.99	0.41
	RO^-*	−0.18	−0.22	0.41			0.28
6	ROH*	1	–	2.28	2.65	0.66	0.27
	RO^-*	−0.27	−0.28	0.49			0.27
8	ROH*	1		4.29	1.30	1.10	0.19
	RO^-*	−0.33	−0.25	0.57			0.19
10	ROH*	–	1	2.73	–	1.87	0.17

A3. Spherically Symmetric Diffusional Problem (SSDP) Analysis

A3.1. Dielectric Constants of C_1OH under 30 MPa isobar between 294 and 543 K

The dielectric constant of C_1OH under the experimental conditions have been determined by the reference data[11] as is described in the text.

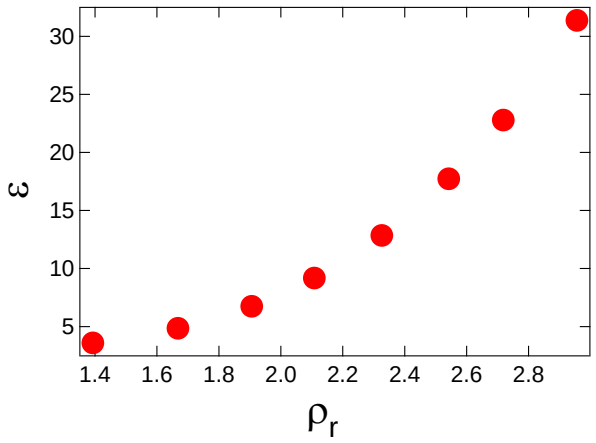

Figure A2. Dielectric constants of C_1OH under 30 MPa isobar between 294 and 543 K versus reduced density.

A3.2. Determination of Self-diffusion Coefficients

Self-diffusion coefficient of C_1OH at high temperature and pressure

We first make a correlation of self-diffusion coefficients of C_1OH at 30 MPa taken from the literature[20] with the reciprocal of temperature. By fitting the plot with the exponential function, we obtained the self-diffusion coefficients under experimental conditions by interpolating the data at corresponding temperatures.

Mutual diffusion coefficient of RO^{-}* and H^{+} in C_1OH at high temperature and pressure

To make a correlation of diffusion coefficient with viscosity of C_1OH, we first determined the viscosity of C_1OH at 30 MPa between 294 and 513 K by interpolating the reference data[22] at 30 MPa for the temperature at which spectrum measurements were conducted. Then we took a correlation of a ratio of the self-diffusion coefficients under experimental conditions (D_{exp}) to those under ambient conditions (D_{amb}) with the reciprocal of viscosity (see Figure A2), and simulated the graph with quadruple function. By assuming that the mutual diffusion at various thermal conditions with respect to that under ambient conditions depends on the reciprocal of viscosity in the same way as those of self-diffusion coefficients, a ratio of the mutual diffusion coefficients under experimental conditions ($D_{\mathrm{exp}}^{\mathrm{RO+H}}$) to those under ambient conditions ($D_{\mathrm{amb}}^{\mathrm{RO+H}}$) with the function of viscosity were expressed with the viscosity as follows;

$$D_{\mathrm{exp}}/D_{\mathrm{amb}} \cong D_{\mathrm{exp}}^{\mathrm{RO+H}}/D_{\mathrm{amb}}^{\mathrm{RO+H}} = 0.55\eta^{-1} + 0.03\eta^{-2} \qquad \text{(A.1)}$$

Finally, by substituting $D_{\mathrm{amb}}^{\mathrm{RO+H}} = 2.8 \times 10^{-5}$ cm^2 s^{-1} given in the reference[23] and viscosity values at experimental conditions for the eq (A.1), $D_{\mathrm{exp}}^{\mathrm{RO+H}}$ were determined.

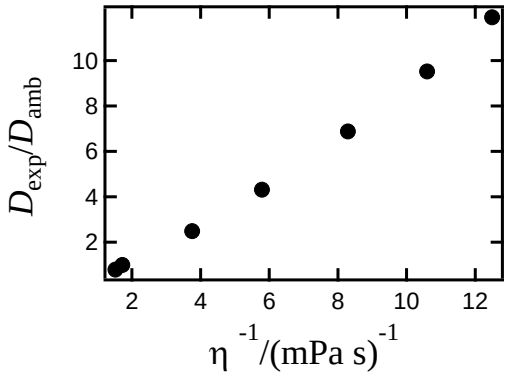

Figure A3. Ratio of the diffusion coefficient of C_1OH under high-temperature and high-pressure to that of C_1OH under ambient conditions against reciprocal of the viscosity.

A3.3. Numerically Obtained Time Profile of the Survival Probability of ROH* and RO^{-}*

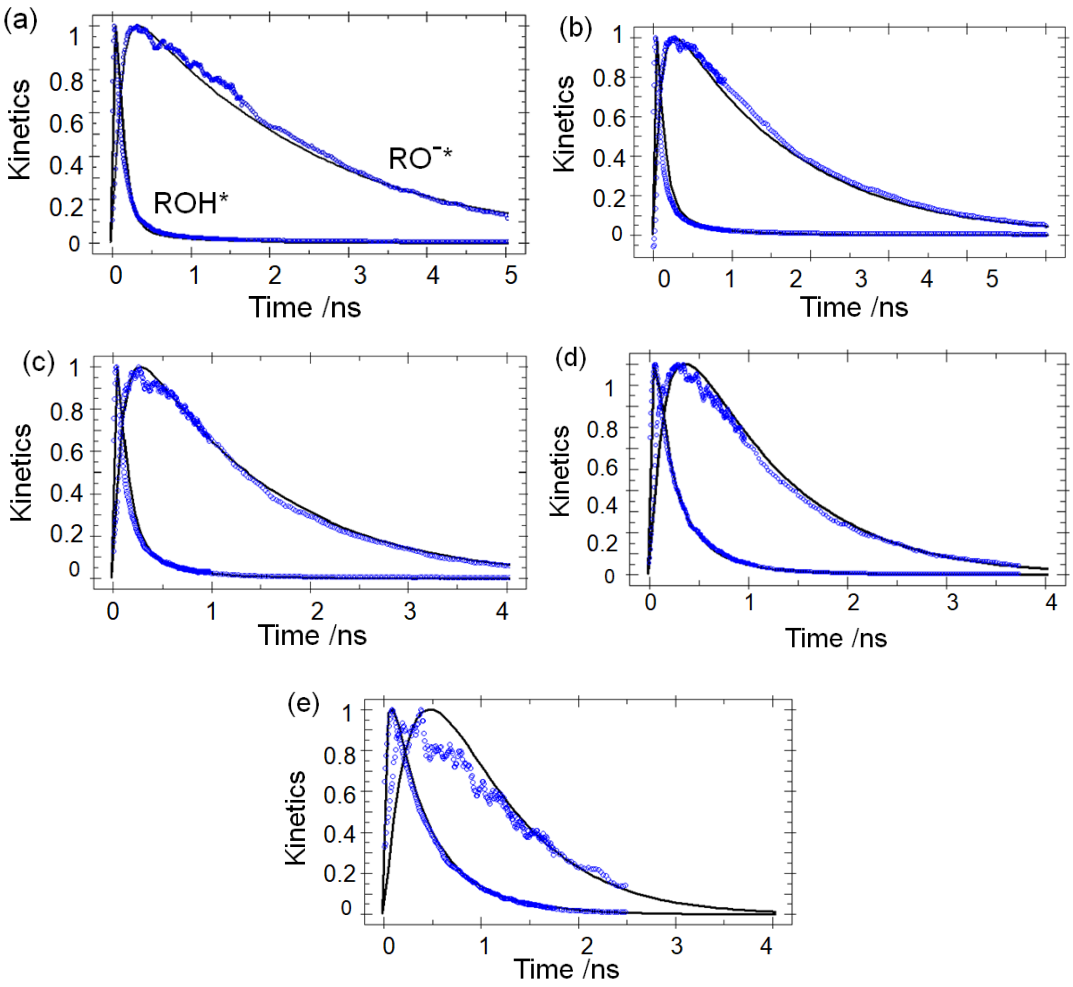

Figure A4. Numerically obtained time profile of the probability of finding ROH* and RO^{-}* in C_1OH 30 MPa isobar at (a) 294, (b) 373, (c) 423, (d) 473 and (e) 513 K.

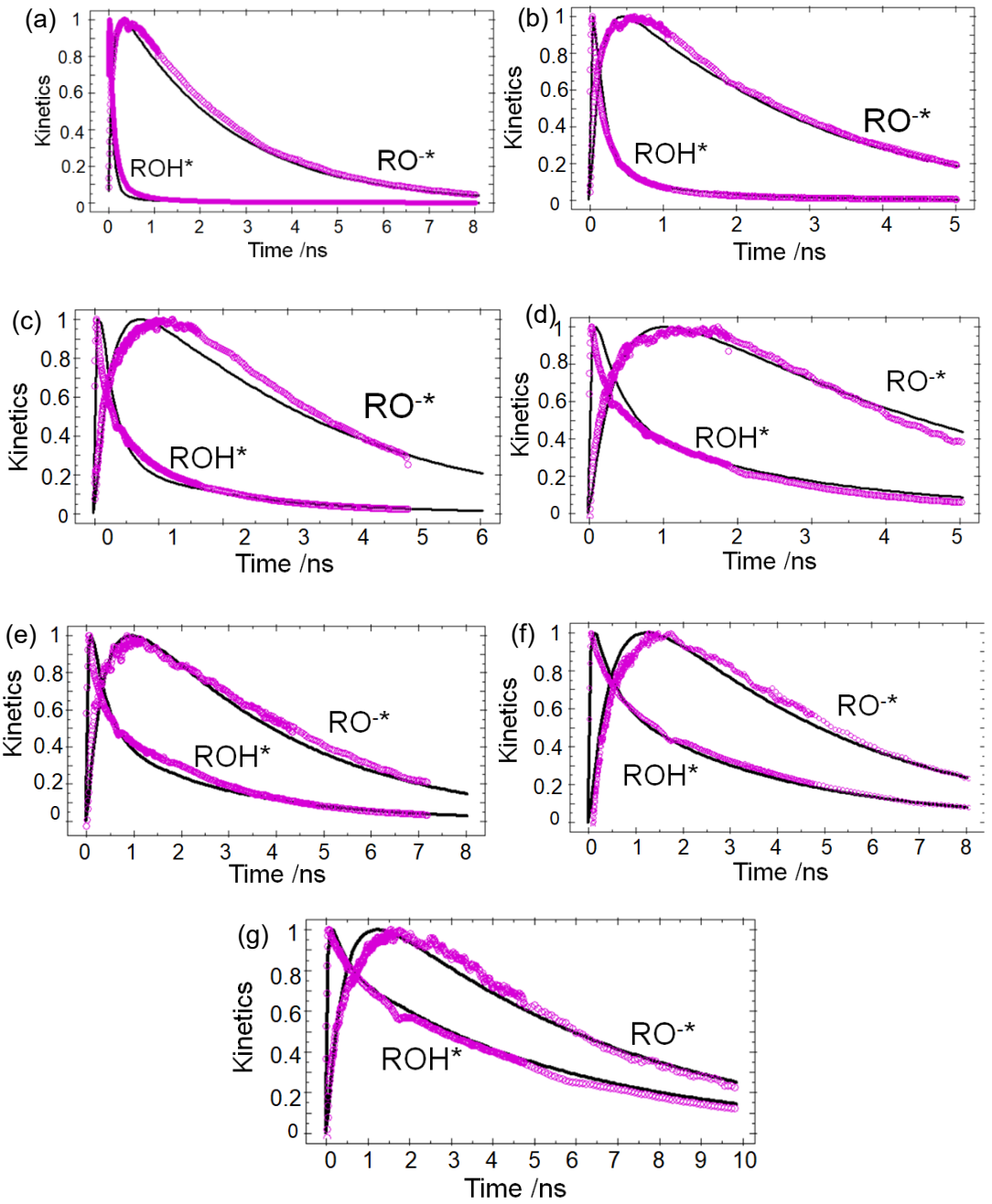

Figure A5. Numerically obtained time profile of the probability of finding ROH* and RO^{-}* in (a) C_1OH, (b) C_2OH, (c) C_3OH, (d) C_4OH, (e) C_5OH, (f) C_6OH and (g) C_8OH under ambient conditions.

A4. Determination of Solvent Parameters

A4.1. Determination of E_T^N

E_T^N value in various C_nOH are taken from the literature.[20] E_T^N values in C_1OH at high temperatures and high pressures which are not available, were determined by measuring the absorption of Reichardt's Dye. From the absorption center ν_R^A/cm^{-1}, we have evaluated E_T^N in C_1OH under various thermal conditions from the following equation.

$$E_T(\text{solvent})(\text{kcal/mol}) = hc\nu_R^A N_A = (2.8591 \times 10^{-3})\nu_R^A \quad \text{(A.2)}$$

$$E_T^N = [E_T(\text{solvent}) - E_T(\text{TMS})]/[E_T(\text{water}) - E_T(\text{TMS})] = \frac{E_T(\text{solvent}) - 30.7}{32.4} \quad \text{(A.3)}$$

In eq (A.2), $E_T(\text{solvent})$ value is defined as the transition energy for Reichardt's Dye measured in kcal/mol. Eq (A.3) is a normalized E_T^N values using E_T value in water ($E_T(\text{water})$= 1.000) and tetramethylsilane (TMS) ($E_T(\text{TMS})$=0.000). In Figure A6 (a), E_T^N values in C_nOH under ambient conditions are plotted against the number of the alkyl chain length of C_nOH. Correlations of E_T^N value in C_1OH at high temperatures and high pressures with the reduced density of C_1OH are shown in Figure A6 (b).

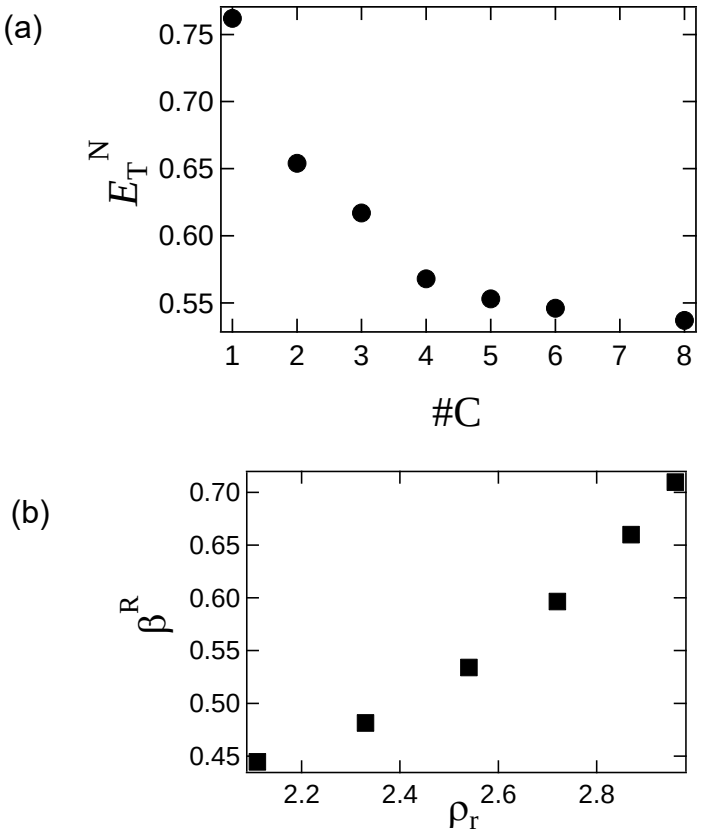

Figure A6. Correlation of E_T^N value (a) in C_nOH under ambient conditions with the number of carbon atoms of solvent n-alcohols and (b) in C_1OH under high-temperatures and high-pressures with the reduced density.

A4.2. Determination of β^{R}

Hydrogen-bonding basicity of C_nOH under ambient conditions were determined by Raman shift of the NH_2 stretching vibration of 4-aminobenzonitrile (ABN) by following equation.[24] Examples of Raman spectrum of ABN is shown in Figure A7.

$$\begin{aligned}\beta^{R} &= 0.45(\nu_{\mathrm{NH_2}} + \nu_{\mathrm{NH_2}}(\mathrm{CCl_4}))/(\nu_{\mathrm{NH_2}}(\mathrm{EtOAc}) - \nu_{\mathrm{NH_2}}(\mathrm{CCl_4}) \\ &= 48.327 - 0.014150 \times (\nu_{\mathrm{NH_2}}/\mathrm{cm^{-1}})\end{aligned} \quad \text{(A.4)}$$

In this equation, carbon tetrachloride (CCl_4, β^{R} = 0.0) and ethylacetate (EtOAc, β^{R} = 0.45) are used as a standard. By making a linear correlation of a function of $\nu_{\mathrm{NH_2}}$, β^{R} in any solvent is determined.

Hydrogen-bonding parameters of C_1OH at high temperature and high pressure was evaluated from the literature,[25] assuming that the shift of $\nu_{\mathrm{NH2}}(\rho)$ from the vapor ($\nu_{\mathrm{NH2}}(\rho = 0)$) reflects the degree of HB interaction by the following equation.

$$\beta^{R} = \beta_{\mathrm{amb}} \frac{\nu_{\mathrm{NH2}}(\rho) - \nu_{\mathrm{NH2}}(\rho = 0)}{\nu_{\mathrm{NH2}}(\rho_{\mathrm{amb}}) - \nu_{\mathrm{NH2}}(\rho = 0)} \quad \text{(A.5)}$$

where $\nu_{\mathrm{NH2}}(\rho = 0)$ is Raman shift of ABN in the gas phase (ν_{NH2} = 3423.1 cm^{-1}), and $\nu_{\mathrm{NH2}}(\rho_{\mathrm{amb}})$ is that in C_1OH under ambient conditions (ν_{NH2}=3351.4 cm^{-1}). β_{amb} is β value at room temperature and is taken from the literature.[26] β^{R} under various thermal conditions were plotted against the density of C_1OH and fit by third-polynomial function. Finally, β^{R} under 30 MPa between 294 and 543 K were obtained by interpolation.

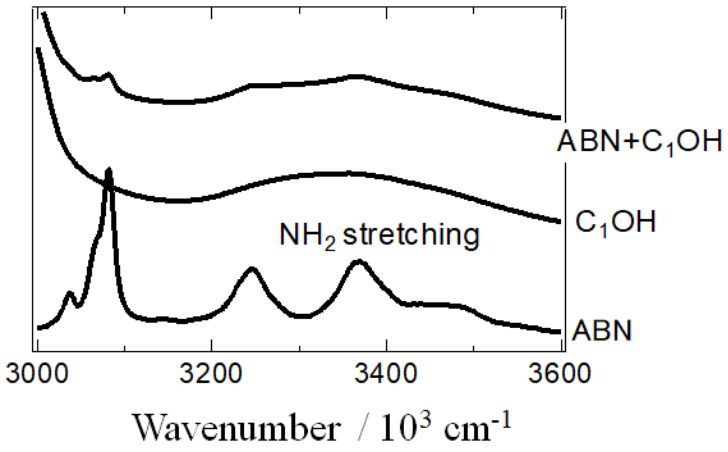

Figure A7. Raman spectrum of 4-aminobenzonitrile (ABN) in C_1OH. Peak around 3400 cm^{-1} is NH_2 stretching mode.

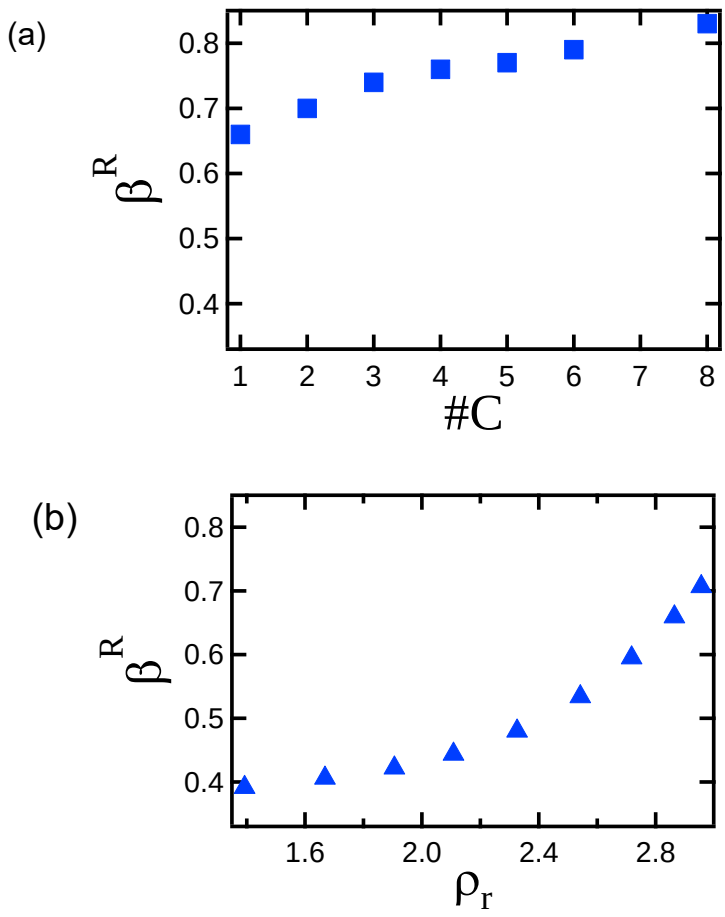

Figure A8. β^R value estimated by Raman shift of NH_2 band (ν_{NH2}) of 4-aminobenzonitrile (ABN). (a) β^R of C_nOH under ambient conditions against the number of carbon atoms of solvent n-alcohols. (b) β^R value of C_1OH at 30 MPa isobar from 294 K to 513 K against reduced density (ρ_r).

A4.3. Summary of E_T^N and β^R

Table A3. E_T^N and β^R of C_nOH determined from absorption band of Reichardt's Dye (ν_R^A) and Raman shift of ABN (ν_{NH2}). π^* values are taken from the literature.[25]

n	E_T^N	ν_{NH2}/cm^{-1}	β^R	π^*
1	0.76	3368.7	0.66	0.6
2	0.65	3365.8	0.70	0.54
3	0.62	3363.3	0.74	0.52
4	0.59	3361.7	0.76	0.47
5	0.57	3361	0.77	0.4
6	0.56	3359.7	0.79	0.4
8	0.54	3356.5	0.83	0.4
10	0.53	3355.5	0.85	0.4

Table A4. E_T^N and β^R of C_1OH determined from absorption band of Reichardt's Dye (ν_R^A) and Raman shift of ABN (ν_{NH2}). π^* values were calculated using the equation taken from the literature.[1]

Temp. /K	Press. /MPa	ν_R^A /nm	E_T^N	ν_{NH2}/cm^{-1}	β^R	π^*
294	30	513.2	0.77	3365.2	0.71	0.63
373	30	540	0.69	3373.2	0.59	0.52
423	30	563.3	0.62	3377.6	0.53	0.45
473	30	596.8	0.53	3381.3	0.48	0.35
513	30	635.3	0.47	3383.9	0.44	0.26

A5. Supplementary Figures

A5.1. Correlation of the peak position of the absorption spectrum of DCN2 in various alcohols with E_T^N

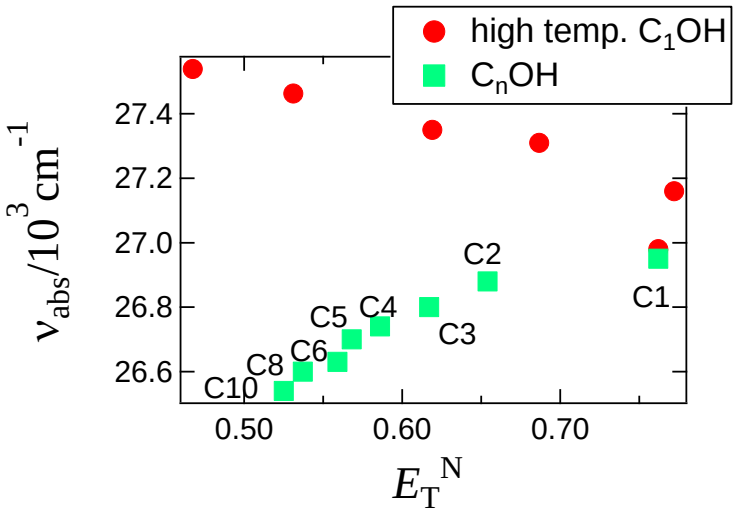

Figure A9. Correlation of the peak position of the absorption spectrum of DCN2 in various alcohols with E_T^N value of the solvent.

A5.2. Dynamic Stokes shift of ROH* in C_nOH under ambient condition

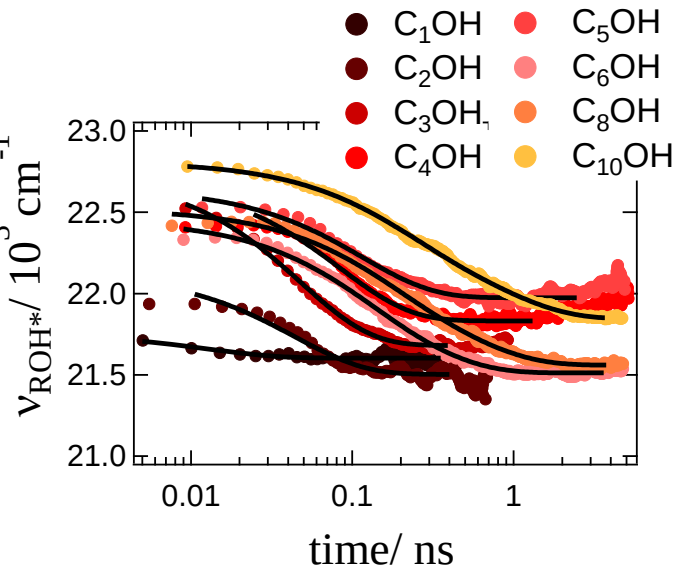

Figure A10. Time profile of the peak position of fluorescence spectrum of DCN2 in C_nOH under ambient conditions. Black solid lines are the results of fitting by a multi (single or double)-exponential function.

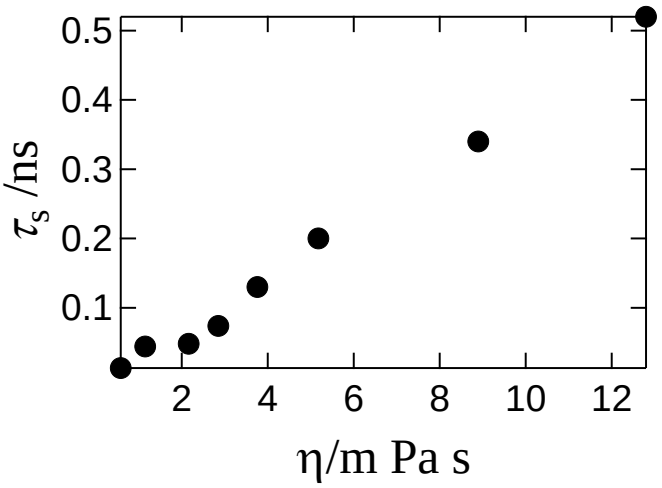

Figure A11. Averaged time-constant for solvation dynamics in various C_nOH under ambient condition plotted against the viscosity.

A5.3. Plot of the Activation Gibbs Free Energy against the β^R

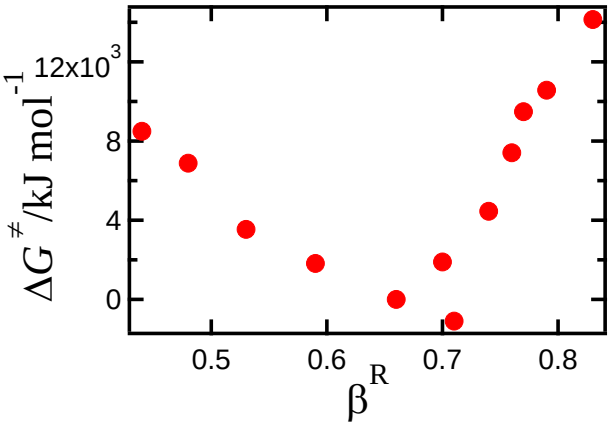

Figure A12. Plot of the activation Gibbs free energy of PT against the β^R of the solvent.

References

1. Kimura, Y.; Fukura, T.; Asada, Y.; Ueno, M.; Yasaka, Y., Raman spectroscopic study on the acceptor number of supercritical methanol and ethanol. *Journal of Molecular Liquids* **2017,** *245*, 11-16.

2. Osawa, K.; Hamamoto, T.; Fujisawa, T.; Terazima, M.; Sato, H.; Kimura, Y., Raman Spectroscopic Study on the Solvation of p-Aminobenzonitrile in Supercritical Water and Methanol. *The Journal of Physical Chemistry A* **2009,** *113* (13), 3143-3154.

3. Solntsev, K. M.; Huppert, D.; Agmon, N., Photochemistry of "Super"-Photoacids. Solvent Effects. *The Journal of Physical Chemistry A* **1999,** *103* (35), 6984-6997.

4. Solntsev, K. M.; Huppert, D.; Agmon, N.; Tolbert, L. M., Photochemistry of "Super" Photoacids. 2. Excited-State Proton Transfer in Methanol/Water Mixtures. *The Journal of Physical Chemistry A* **2000,** *104* (19), 4658-4669.

5. Tolbert, L. M.; Haubrich, J. E., Photoexcited Proton Transfer from Enhanced Photoacids. *Journal of the American Chemical Society* **1994,** *116* (23), 10593-10600.

6. Green, S.; Xiang, T.; Johnston, K. P.; Fox, M. A., Excited-state Deprotonation of .beta.-Naphthol in Supercritical Water. *The Journal of Physical Chemistry* **1995,** *99* (38), 13787-13795.

7. Kobayashi, I.; Terazima, M.; Kimura, Y., Study of the Excited-State Proton-Transfer Reaction of 5-Cyano-2-naphthol in Sub- and Supercritical Water. *The Journal of Physical Chemistry B* **2012,** *116* (3), 1043-1052.

8. Gingrich, D. E.; Lisko, J. G.; Curry, M. A.; Cheng, M.; Quail, M.; Lu, L.; Wan, W.; Albom, M. S.; Angeles, T. S.; Aimone, L. D.; Haltiwanger, R. C.; Wells-Knecht, K.; Ott, G. R.; Ghose, A. K.; Ator, M. A.; Ruggeri, B.; Dorsey, B. D., Discovery of an Orally Efficacious Inhibitor of Anaplastic Lymphoma Kinase. *Journal of Medicinal Chemistry* **2012,** *55* (10), 4580-4593.

9. Kimura, Y.; Amita, F.; Fujisawa, T., Non-linear Laser Spectroscopy in Supercritical Fluids. *REVIEW OF HIGH PRESSURE SCIENCE AND TECHNOLOGY* **2006,** *16* (2), 87.

10. Gardecki, J.; Maroncelli, M., Set of secondary emission standards for calibration of the spectral responsivity in emission spectroscopy. *Applied Spectroscopy* **1998,** *52* (9), 1179-1189.

11. Hiejima, Y.; Kajihara, Y.; Kohno, H.; Yao, M., Dielectric relaxation measurements on methanol up to the supercritical region. *Journal of Physics: Condensed Matter* **2001,** *13* (46), 10307-10320.

12. Krissinel, E. B.; Agmon, N., Spherical symmetric diffusion problem. *Journal of Computational Chemistry* **1996,** *17* (9), 1085-1098.

13. Ryan, E. T.; Xiang, T.; Johnston, K. P.; Fox, M. A., Excited-State Proton Transfer Reactions in Subcritical and Supercritical Water. *The Journal of Physical Chemistry* **1996,** *100* (22), 9395-9402.

14. Viswanath, D. S.; Ghosh, T. K.; Prasad, D. H.; Dutt, N. V.; Rani, K. Y., *Viscosity of liquids: theory, estimation, experiment, and data*. Springer Science & Business Media: 2007.

15. Horng, M. L.; Gardecki, J. A.; Papazyan, A.; Maroncelli, M., Subpicosecond Measurements of Polar Solvation Dynamics: Coumarin 153 Revisited. *The Journal of Physical Chemistry* **1995,** *99* (48), 17311-17337.

16. Genosar, L.; Leiderman, P.; Koifman, N.; Huppert, D., Effect of Pressure on Proton Transfer Rate from a Photoacid to a Solvent. 3. 2-Naphthol and 2-Naphthol Monosulfonate Derivatives in Water. *The Journal of Physical Chemistry A* **2004,** *108* (10), 1779-1789.

17. Genosar, L.; Leiderman, P.; Koifman, N.; Huppert, D., Effect of Pressure on the Proton-Transfer Rate from a Photoacid to a Solvent. 2. DCN2 in Propanol. *The Journal of Physical Chemistry A* **2004,** *108* (2), 309-319.

18. Kamlet, M. J.; Abboud, J. L. M.; Abraham, M. H.; Taft, R. W., Linear solvation energy relationships. 23. A comprehensive collection of the solvatochromic parameters, .pi.*, .alpha., and .beta., and some methods for simplifying the generalized solvatochromic equation. *The Journal of Organic Chemistry* **1983,** *48* (17), 2877-2887.

19. Cohen, B.; Huppert, D., Evidence for a Continuous Transition from Nonadiabatic to Adiabatic Proton Transfer Dynamics in Protic Liquids. *The Journal of Physical Chemistry A* **2001,** *105*, 2980-2988.

20. Reichardt, C., *Solvents and Solvent Effects in Organic Chemistry, Third, Updated and Enlarged Edition*. WILEY-VCH: 2004.

21. Bulgarevich, D., S.; Sako,T.; Sugeta, T.; Otake,K.; Takebayashi, Y.; Kamizawa, C.; Uesugi, M.; Kato, M., Microscopic solvent structure of subcritical and supercritical methanol from ultraviolet/visible absorption and fluorescence spectroscopies. *American Institute of Physics* **1999,** *111*, 4239-4250.

22. Karger, N.; Vardag, T.; Lüdemann, H. D., Temperature dependence of self-diffusion in compressed monohydric alcohols. *Journal of Chemiocal Physics.,* **1990,** *93* (5), 3437-3444.

23. Genosar, L.; Leiderman, P.; Koifman, N.; Huppert, D., Effect of Pressure on the Proton Transfer Rate from a Photoacid to a Solvent. 4. Photoacids in Methanol. *The Journal of Physical Chemistry A* **2004,** *108*, 309-319.

24. Kobayashi, A.; Osawa, K.; Terazima, M.; Kimura, Y., Solute-solvent hydrogen-bonding in room temperature ionic liquids studied by Raman spectroscopy. *Physical Chemistry Chemical Physics* **2012,** *14* (39), 13676-13683.

25. Fujisawa, T.; Terazima, M.; Kimura, Y., Solvent effects on the local structure of p-nitroaniline in supercritical water and supercritical alcohols. *The Journal of Physical Chemistry A* **2008,** *112* (24), 5515-5526.

26. Ghanadzadeh G, A.; Taghvaei, V.; Moradi R, E.; Mirzaei, M., Photo-physical and structural studies of some synthesized arylazoquinoline dyes. *Spectrochim Acta A Mol Biomol Spectrosc.,* **2017,** *185*, 111-124.

Chapter 3

Proton Transfer Dynamics in Protic Ionic Liquids

3.1. Introduction

Among various kinds of ionic liquids (ILs), protic ionic liquids (PILs) have been attracted as a new class of solvent for acid-base reaction.[1] PILs are composed of conjugate base of AH (A) and acid B (BH^+) and can undergo proton transfer (PT) in solutions with solute molecules dissolved in them. Until now, numerous researches on the physicochemical property[1-5] and PT mechanism of PILs have been conducted by computational methods,[6,7] thermal analysis[8] and several spectroscopies such as NMR spectroscopy[9,10] and Raman spectroscopy.[11,12] Among these studies, the basicity of anion can be expected to have a large impact on the behavior of PILs, especially on the PT reaction yield in them. However, there are few studies focused on the real-time analysis of PT dynamics in PILs. In this study, we investigate PT dynamics in three different PILs by probing the fluorescence dynamics of photoacids dissolved in them and clarify how PT kinetics is described with physicochemical properties of solvent PILs.

We investigated the ESPT dynamics of 5-cyano-2-naphthol (5CN2) and 5,8-dicyano-2-naphthol (DCN2) in three PILs composed of different anions, trifluoro-methanesulfonate ($[CF_3SO_3]$), methanesulfonate, ($[CH_3SO_3]$) and trifluoroacetate ($[CF_3COO]$), by measuring steady-state and time-resolved fluorescence spectra. Since the pK_a values of conjugate acids are quite different from one another in aqueous solution, (pK_a = -12 (CF_3SO_3H), -2 (CH_3SO_3H) and 0.23 (CF_3COOH)),[13] we expected that the dynamics of photoacids should be variant, that is, an appearance of RO^-* may depend on the basicity of anions.

3.2. Experiment

3.2.1. Materials

5CN2 were synthesized according to references.[14,15] Reaction schemes are shown in the Appendix B1. The crude products of 5CN2 was purified by sublimation.

Figure 3-1 shows the structures of PILs. All PILs were synthesized in our laboratory. Triethylamine, trifluoromethanesulfonic acid, methanesulfonic acid, and trifluoroacetic acid (guaranteed grade) were purchased from Nakalai Tesque. Triethylamine was purified by distillation before use. To prepare the PILs, the corresponding acid was added dropwise to the 1.1 eq of triethlyamine at 0℃ under Ar atmosphere. The ice bath was removed and the reaction mixture was stirred at room temperature for 3h (in the case of $[N_{222}H][CF_3SO_3]$), overnight (in the case of $[N_{222}H][CH_3SO_3]$) or 8h (in the case of $[N_{222}H][CF_3COO]$), respectively. In the case of $[N_{222}H][CH_3SO_3]$ and $[N_{222}H][CF_3COO]$, crude products were purified by recrystallization from 1,2-dimethoxyethane at 213 K. The recrystallized samples were treated under vacuum at room temperature for 24 h to remove the residual solvent. Since $[N_{222}H][CF_3SO_3]$ was yellowish, it was treated by charcoal and successfully decolorized. The purities of these ionic liquids were confirmed by ^1H and ^{13}C NMR spectroscopy. In the case of $[N_{222}H][CF_3SO_3]$, the purities was also checked by fluorescence spectrum, and we confirmed that fluorescence from

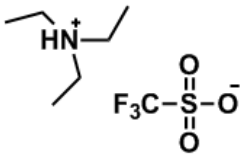

$[N_{222}H][CF_3SO_3]$ (-12)

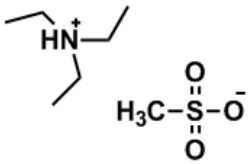

$[N_{222}H][CH_3SO_3]$ (-2)

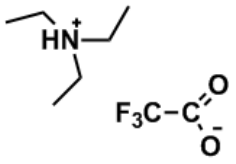

$[N_{222}H][CF_3COO]$ (0.23)

Figure 3-1. The structure of protic ionic liquids. Values in parenthensis are pK_a of conjugate acid of anion composed of PILs.[13]

$[N_{222}H][CF_3SO_3]$ was negligible.

Before spectroscopic measurements, all PILs were evacuated at room temperature for $[N_{222}H][CH_3SO_3]$ and $[N_{222}H][CF_3COO]$, and at 333 K for $[N_{222}H][CF_3SO_3]$. The amount of water contamination was confirmed to be below 300 ppm by Karl-Fisher titration. Water content of each sample are summarized in Table 3-1. After drying PILs, a certain amount of 5CN2 or DCN2 was dissolved in each PIL in a glovebox.

3.2.2. Absorption and Fluorescence Measurements

Absorption and fluorescence spectra were measured at room temperature by standard spectrometers (Shimadzu UV-2500PC and JASCO, FP-6500), respectively. For time-resolved fluorescence measurement, we used the same setups as described in the last chapter. Briefly, an excitation light of 800 nm from an amplified Ti:sapphire laser (Spectra physics, Spitfire Xp) was converted to 340 nm (for 5CN2 measurements) or 370 nm (for DCN2 measurements) by an OPA (Spectra physics, TOPAS-800C) and a BBO crystal. Fluorescence from a sample solution in a 1 mm path length quartz cell was detected by a streak camera (Hamamatsu, C4334) attached to a spectrometer (Princeton Instruments, Acton SP2150).

For the measurement of the ultrafast dynamics within a hundred picosecond, we used the optical Kerr gate system for the fluorescence measurement with time resolution of a few hundred femtosecond.[16] The experimental details are given in Appendix B2. The excitation pulse (370 nm) was produced by OPA operated by the fundamental pulse of the Ti;Sapphire amplifier, and a portion of fundamental pulse (800 nm) was used as a gate pulse. The optical Kerr gate was operated by using benzene as a Kerr medium and the gated fluorescence was detected by a time-gated image intensifier (Lavision, Picostar HR).

The time resolution of the system was ca. 0.5 ps as FWHM.

3.3. Results

3.3.1. Steady State Absorption and Fluorescence Spectra

Figure 3-2 shows absorption spectra of (a) 5CN2 and (b) DCN2 in PILs. The spectral shapes of 5CN2 and DCN2 in three PILs were almost the same and were identical to those of normal form (the non-dissociated form in the electronic ground state) reported previously.[17] Therefore we conclude that 5CN2 and DCN2 don't undergo PT in PILs in the ground states.

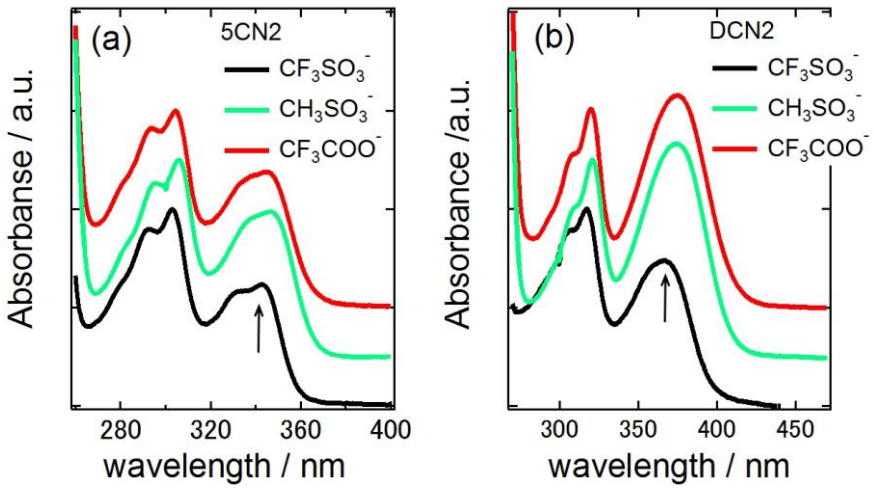

Figure 3-2. Absorption spectra of (a) 5CN2 and (b) DCN2. Each spectrum is normalized by the peak intensity around 300nm and shown with an arbitrary vertical offset.

Figures 3-3 shows the steady-state fluorescence spectra of 5CN2 and DCN2 in PILs. The horizontal scale of each figure is in wavenumber, and the fluorescence at higher wavenumbers corresponds to that from ROH* (25000 cm^{-1} for 5CN2 and 23000 cm^{-1} for DCN2) and that located at lower wavenumber (18000 cm^{-1} for 5CN2 and 16000 cm^{-1} for DCN2) is fluorescence from anionic form. For 5CN2, except in $[N_{222}H][CF_3COO]$, fluorescence from ROH* was dominant. In $[N_{222}H][CH_3SO_3]$, weak fluorescence from RO^-* appeared, which indicates the occurrence of ESPT of 5CN2 in $[N_{222}H][CH_3SO_3]$. On the other hand, the fluorescence spectrum in $[N_{222}H][CF_3COO]$ was quite different

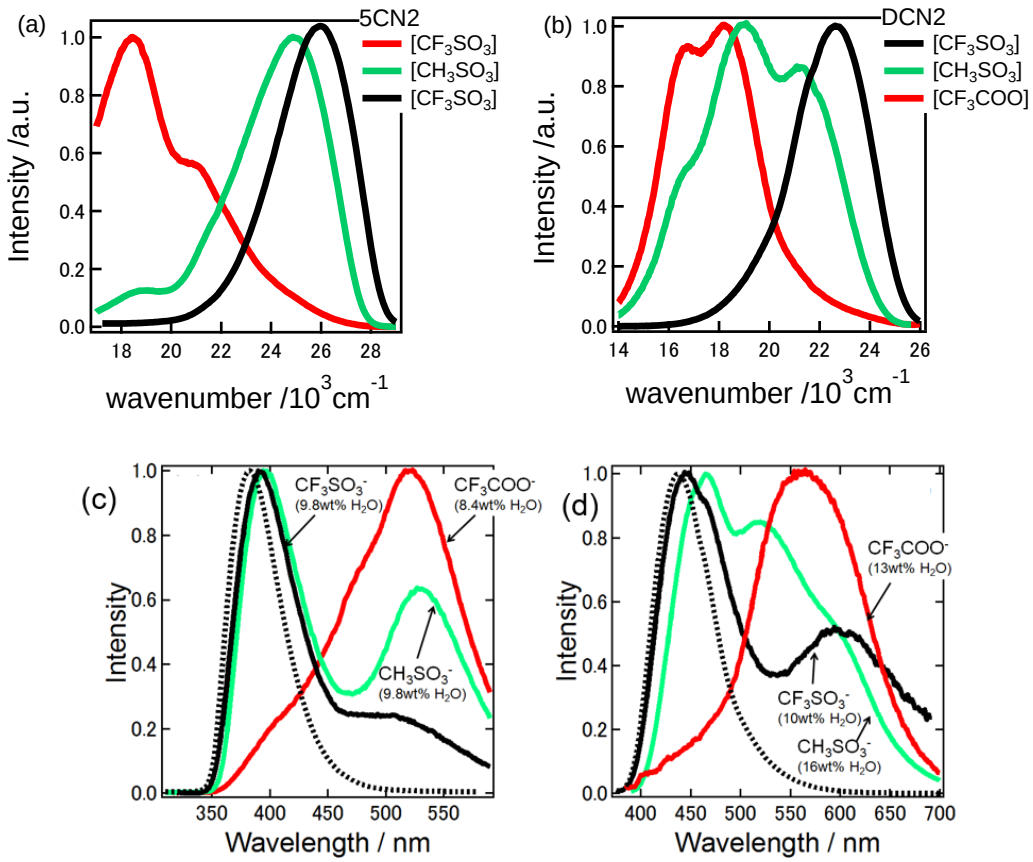

Figure 3-3. Steady-state fluorescence spectra of (a) 5CN2 and (b) DCN2. Figures (c) 5CN2 and (d) DCN2 are those with more than 10wt% of water. These spectra were normalized at the peak position that was maximum intensity. Spectra with dashed line represent (a) 5CN2 and (b) DCN2 in $[N_{222}H][CF_3SO_3]$ shown in (a) and (b).

from those in other PILs. The fluorescence from ROH* almost disappeared and two bands appeared around 470 nm and 550 nm. The intensity of the band at the shorter wavelength decreased with an addition of water to the solution while that of the longer wavelength increased with an addition of water (Figure 3-3(c) and (d).) Considering the peak position[18,19], the band around 18000 cm^{-1} should be assigned to the fluorescence from RO^-*, while the band around 22000 cm^{-1} infers presence of unknown species. Hereafter we denote the fluorescent species around 22000 cm^{-1} as Y^-* and expect it to be negatively charged since the peak position is close to that of RO^-*.

For DCN2, we found the same trend of fluorescence spectrum depending on the anion species of PILs. In $[N_{222}H][CF_3SO_3]$, the fluorescence from ROH* was dominant and no other species was observed. However in $[N_{222}H][CH_3SO_3]$ and $[N_{222}H][CF_3COO]$, the fluorescence bands from Y^-* (18000 cm^{-1}) and RO^-* (16000 cm^{-1}) were apparent.

In order to obtain the fluorescence peak position of each component, the fluorescence spectrum in Figures 3-3 were simulated by a sum of log-normal functions as follows:

$$I_{\mathrm{fl}}(\nu) = \sum h_{\mathrm{i}} \times \begin{cases} \exp[-\ln(2)\{\ln(1+\alpha_{\mathrm{i}})/\gamma_{\mathrm{i}}\}^2] & \alpha_{\mathrm{i}} > -1 \\ 0 & \alpha_{\mathrm{i}} \le -1 \end{cases} \tag{3.1}$$

where $I_{\mathrm{fl}}(\nu)$ is the fluorescence intensity as a function of wavenumber ν, $\alpha_i = 2\gamma_i(\nu_i - \nu_{\mathrm{p}i})/\Delta_i$, h_i is the scaling factor, $\nu_{\mathrm{p}i}$ is the peak position of the spectrum, γ_i is the asymmetric factor, and Δ_i is the band width parameter, respectively. The suffix, i, denotes the chemical species. Typical examples of the spectral decomposition are shown in Figure 3-4. In the case of 5CN2 and DCN2 in $[N_{222}H][CF_3COO]$, since the intensity ROH* was too small, it was difficult to decompose the spectrum into three species. Therefore, we fixed the peak position of ROH* to the value obtained by the analysis of the time-resolved spectrum where the intensity of ROH* was strong in earlier delay time

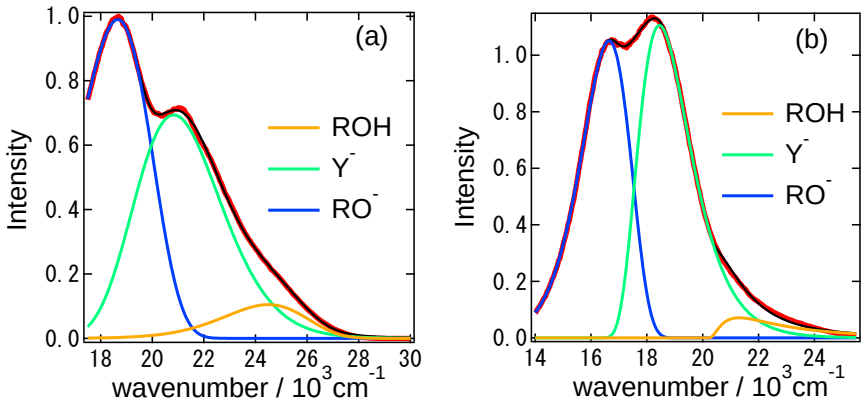

Figure 3-4 Spectral decomposition of steady-state fluorescence spectrum of (a) 5CN2 and (b) DCN2 in $[N_{222}H][CF_3COO]$. Black solid lines are the result of the fitting. Yellow, green and blue solid lines indicate the spectra of ROH*, Y^-* and RO^-*, respectively.

(~1ns) which are shown in Figures 3-4 (c) and 3-5 (c), as will be discussed in the next section. Table 3-1 summarizes peak positions of fluorescence bands together with the absorption peak positions of the lowest transition energy.

Table 3-1. Peak positions of the absorption (ν^{abs}) and steady-state fluorescence spectrum of each species ($\nu_{\mathrm{p,ROH^*}}, \nu_{\mathrm{p,Y^{-*}}}, \nu_{\mathrm{p,RO^{-*}}}$) of 5CN2 and DCN2. ν_{abs} are indicated by the arrows in Figure 3-2. $\Delta\nu$ is the Stokes-shift calculated from $\Delta\nu = \nu^{\mathrm{abs}} - \nu_{\mathrm{p,ROH^*}}$.

	Water contamination /ppm	ν^{abs} /10^3 cm^{-1}	$\nu_{\mathrm{p,ROH^*}}$ /10^3 cm^{-1}	$\nu_{\mathrm{p,Y^{-*}}}$ /10^3 cm^{-1}	$\nu_{\mathrm{p,RO^{-*}}}$ /10^3 cm^{-1}	$\Delta\nu$
			5CN2			
$CF_3SO_3^-$	260	29.15	25.98	-	-	3.17
$CH_3SO_3^-$	130	28.78	24.91	-	18.43	3.88
CF_3COO^-	300	28.92	24.50	20.80	18.16	4.42
			DCN2			
$CF_3SO_3^-$	230	27.17	22.68	-	-	4.49
$CH_3SO_3^-$	70	26.60	21.21	18.5	16.31	5.39
CF_3COO^-	220	26.55	21.30	18.44	16.64	5.25
					10^3 cm^{-1}	

3.3.2. Time-resolved Fluorescence Spectra

Figures 3-5 (a)-(c) show time-resolved fluorescence spectra of 5CN2 in PILs. As is expected from the steady-state fluorescence spectrum, time-resolved spectra also show remarkable dependence on the solvent anion species. In the case of 5CN2 in $[N_{222}H][CF_3SO_3]$ (Figure 3-5 (a)), only the fluorescence from ROH* was observed and no other species was apparent even if time passed by. This indicates that 5CN2 did not undergo ESPT in $[N_{222}H][CF_3SO_3]$, because the acidity of CF_3SO_3H is larger than that of 5CN2, and ROH* is not able to give proton to the anionic species. In $[N_{222}H][CH_3SO_3]$ (Figure 3-5 (b)), as expected from the steady-state spectrum in Figure 3-3, fluorescence from RO^{-}* gradually increased over several nano seconds after excitation, although the intensity of RO^{-}* was quite small. Interestingly, time resolved fluorescence in $[N_{222}H][CF_3COO]$ showed appearance and disappearance of a newly found species. Upon

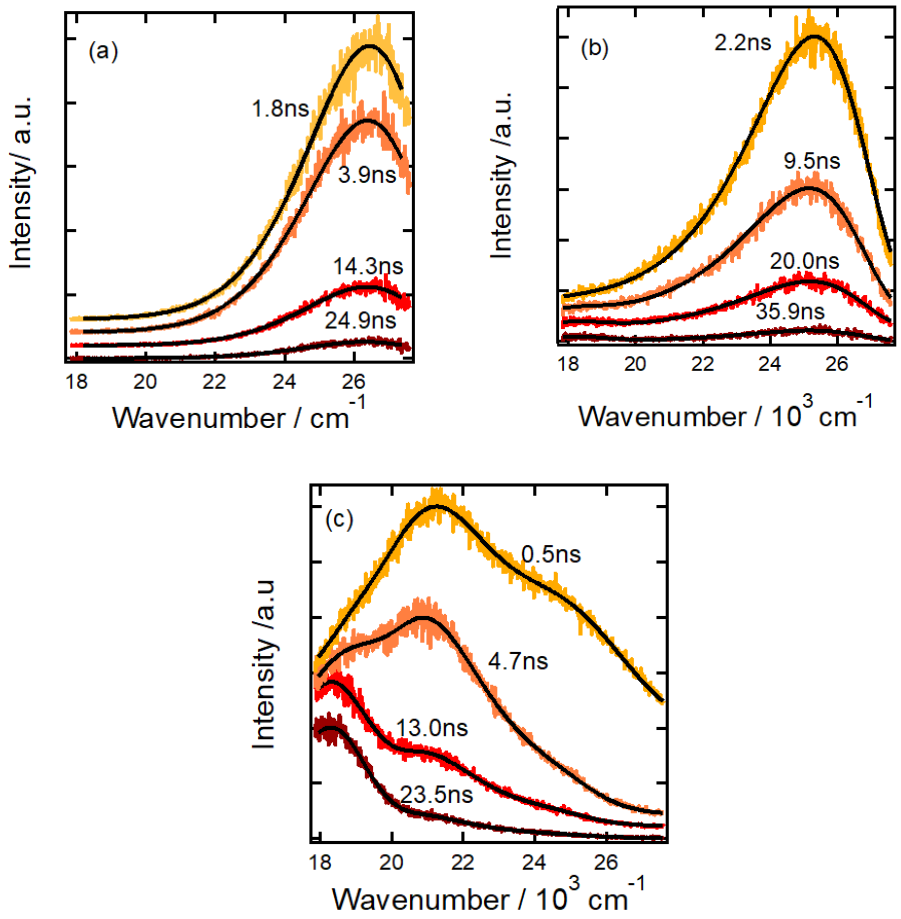

Figure 3-5. Time-resolved flureoscence spectrum of 5CN2 in (a) $[N_{222}H][CF_3SO_3]$, (b) $[N_{222}H][CH_3SO_3]$ and (c) $[N_{222}H][CF_3COO]$.

excitation, not only a fluorescence band from ROH* but also a new fluorescent band around 21000 cm^{-1} emerged within 0.5 ns. Then this new fluorescence component Y^-* disappeared and the fluorescence from RO^-* increased by ca~10 ns.

For DCN2 as shown in Figs. 3-6 (a)-(c), almost the same story can be true for the solution of $[N_{222}H][CF_3SO_3]$, where only the fluorescence from ROH* was observed. However, the contribution from Y^-* dramatically changed the time-resolved fluorescence spectra in $[N_{222}H][CF_3COO]$ and $[N_{222}H][CH_3SO_3]$.

In order to extract the time profile of each component, the time dependent fluorescence spectrum was simulated by a sum of log-normal functions as was done for

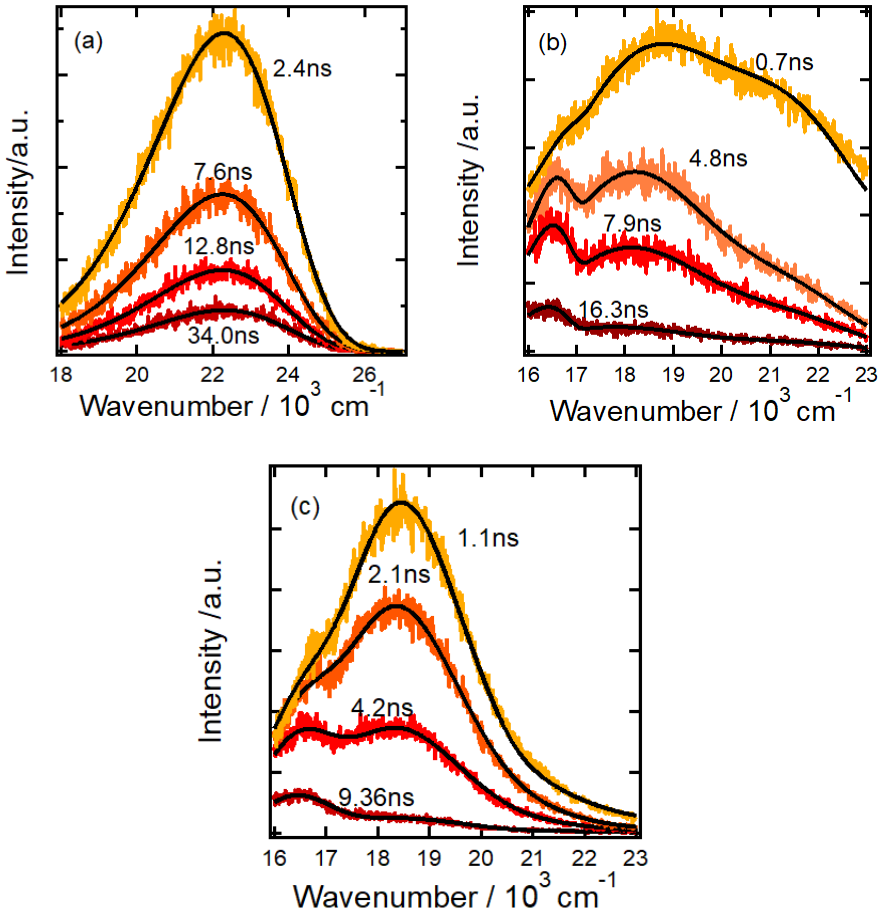

Figure 3-6. Time-resolved fluorescence spectrum of DCN2 in (a) $[N_{222}H][CF_3SO_3]$, (b) $[N_{222}H][CH_3SO_3]$ and (c) $[N_{222}H][CF_3COO]$.

the steady state fluorescence spectrum (eq. (3.1)). In this case, the parameters in the equation are expected to depend on the delay time after the photoexcitation. However, we have made some restrictions on the parameters except for the intensity parameter (h_i) since the number of the fitting parameters is be too large for the case where three fluorescence components exist. Fitting procedures for each combination of solute and solvent are as follows. For both 5CN2 and DCN2 in $[N_{222}H][CF_3SO_3]$ where only the fluorescence from ROH* was observed, the time dependent spectrum was stimulated by a single log-normal function assuming that all parameters were time-dependent. For 5CN2 in $[N_{222}H][CH_3SO_3]$ in which ROH* and RO^-* appeared, two log-normal functions

were used to stimulate the spectrum. Since the contribution of RO^{-}* was quite small, the parameters of $\nu_{pi}(t), \Delta_i(t)$ and $\gamma_i(t)$ of RO^{-}* were fixed to the values determined at the longer delay time after the photoexcitation, where the contribution of RO^{-}* was large. Here the parameters of Δ_i and γ_i of ROH* were also fixed to the values determined in the earlier delay time neglecting the contributions of RO^{-}*. For 5CN2 in $[N_{222}H][CF_3COO]$ and DCN2 in $[N_{222}H][CH_3SO_3]$ and $[N_{222}H][CF_3COO]$, where three components are expected, three log-normal functions were used to stimulate the spectrum. Since the rise of Y^{-}* and the decay of ROH* were very fast, we first determined the parameters related to these species by fitting the spectrum at earlier delay time (~1 ns) where fluorescence bands from ROH* and Y^{-}* were dominant. Then using the parameters obtained by the fit, the spectrum at the longest delay time, where fluorescence bands from Y^{-}* and RO^{-}* were dominant, was simulated by using the parameters Δ_i and γ_i of ROH* determined in the earlier delay time. Finally, all time-dependent data were fitted by assuming that parameters of each species were time-independent except for the peak position of Y^{-}* and intensities of all species. The black solid lines in Figures 3-5 and 3-6 are the results of fitting, and the spectral simulation worked quite well in each case.

Time profiles of fluorescence intensities of species, ROH*, Y^{-}* and RO^{-}* evaluated by the integral of each fluorescence component are shown in Figures 3-7 and 3-8. The time profile of each component was generally simulated by a multi-exponential function (at most 3 exponents) as follows;

$$I_X(t) = A_1\, e^{-k_1 t} + A_2 e^{-k_2 t} + A_3 e^{-k_3 t}, \tag{3.2}$$

where $I_X(t)$ means the time profile of the integrated fluorescence intensity of molecular species of X. Here X represents ROH*, Y^{-}* or RO^{-}*. In the cases of 5CN2 and DCN2 in $[N_{222}H][CF_3SO_3]$, the integrated intensity of ROH* was simulated by a single exponential

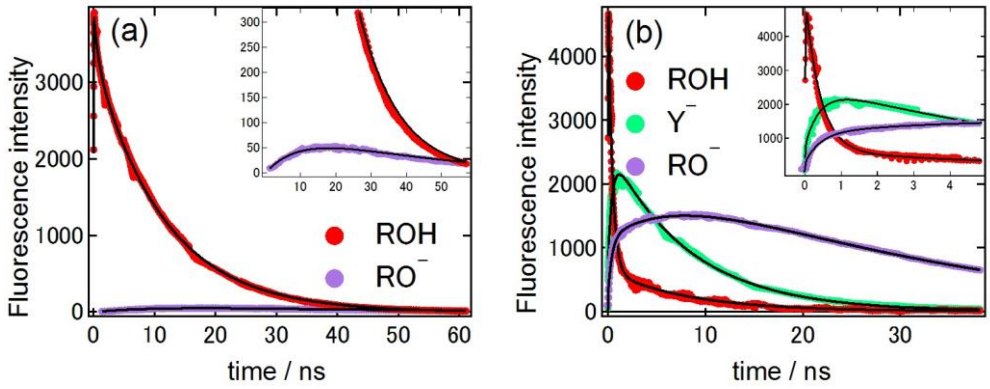

Figure 3-7. Time profiles of fluorescence intensity of 5CN2 in (a) $[N_{222}H][CH_3SO_3]$ and (b) $[N_{222}H][CF_3COO]$. Solid line is a fitting curve of convolution exponential function. Inset graph represents the fluorescence decay in early delay time.

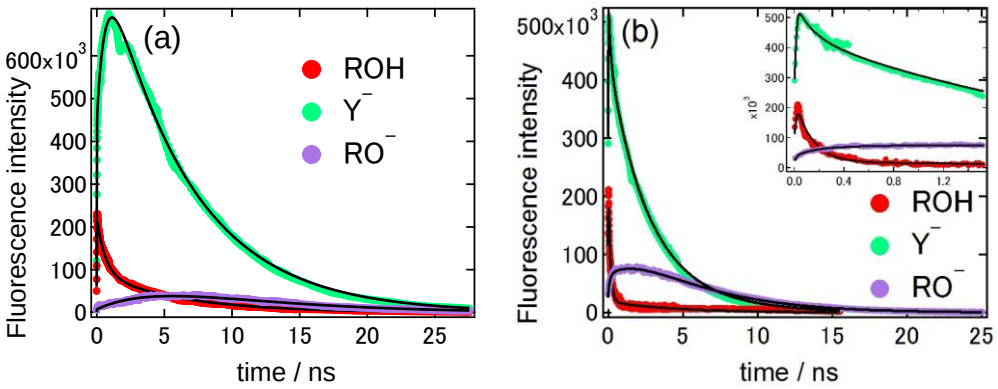

Figure 3-8. Time profile of fluorescence intensity of DCN2 in (a) $[N_{222}H][CH_3SO_3]$ and (b) $[N_{222}H][CF_3COO]$. Solid line is a fitting curve of convolution exponential function. Inset graph represents the fluorescence decay in early delay time.

decay (not shown in Figures 3-7 and 3-8). In the case of 5CN2 in $[N_{222}H][CH_3SO_3]$, as shown in Figure 3-7 (a), ROH* showed a double exponential decay with a small contribution of the very fast component, and a large contribution of the slower component (see Table 3-2). On the other hand, RO^-* kinetics showed an exponential rise and decay (see inset graph in this figure). Since the time constant of the rise was similar to that of the slow decay of ROH*, we fit these two profiles by linking this time constant. The results of the fittings are shown by the solid lines in Figure 3-7 (a). The fitting almost

captures the time profile of each species, although slight deviation is seen in longer time region of ROH*. In the cases of 5CN2 in $[N_{222}H][CF_3COO]$ and, DCN2 in $[N_{222}H][CH_3SO_3]$ and $[N_{222}H][CF_3COO]$ (Fig. 3-7(b) and Figs. 3-8(a) and (b)), the fastest decay constant of ROH* seems to be equal to the rise time constant of Y^-*, and the decay time of Y^-* to be the rise time constant of RO^-*. Considering these factors, we fit these profiles to eq. (3.2) by linking the three time-constants. The parameters obtained by the fitting are summarized in Tables 3-2 (5CN2) and 3-3 (DCN2).

Table 3-2. Rate constants of ESPT of 5CN2 determined by multi-exponential fitting to the time-profile of fluorescence intensity of each species. The amplitude parameters are normalized by the value of the fastest component of ROH*.

anion	species	A_1	A_2	A_3	k_1/ ns^{-1}	k_2/ ns^{-1}	k_3/ ns^{-1}
$CF_3SO_3^-$	ROH*	1			0.13		
$CH_3SO_3^-$	ROH*	1	6.28	0	1.36	0.09	0.03
	RO^-*	0	-0.26	0.26			
CF_3COO^-	ROH*	1	0.15	0	2.40	0.14	0.03
	Y^-*	-0.41	0.54	0.04			
	RO^-*	-0.22	-0.34	0.59			

Table 3-3. Rate constants of ESPT of DCN2 determined by multi-exponential fitting to the time-profile of fluorescence intensity of each species. The amplitude parameters are normalized by the value of the fastest component of ROH*.

anion	species	A_1	A_2	A_3	k_1 /ns^{-1}	k_2 / ns^{-1}	k_3 /ns^{-1}
$CF_3SO_3^-$	ROH*	1			0.09		
$CH_3SO_3^-$	ROH*	1	0.71	0	1.61	0.16	0.17
	Y^-*	-3.67	7.11	0			
	RO^-*	0	22.2	-22.2			
CF_3COO^-	ROH*	1	0	0.09	7.12	0.41	0.22
	Y^-*	0.51	1.66	0.46			
	RO^-*	-0.13	-0.72	1.04			

3.4. Discussion

3.4.1. Modeling of Reaction Kinetics

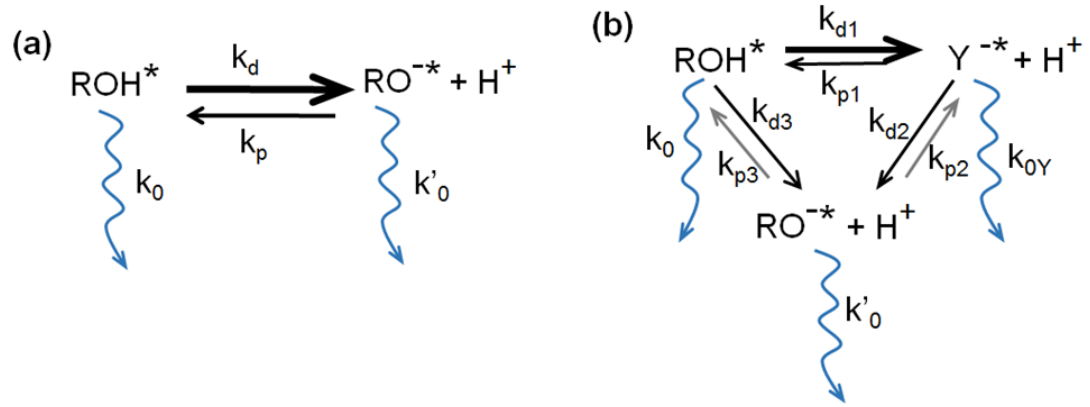

Scheme 3-1. ESPT schemes of (a) 5CN2 in $[N_{222}H][CH_3SO_3]$ and (b) 5CN2 in $[N_{222}H][CF_3COO]$, DCN2 in $[N_{222}H][CH_3SO_3]$ and DCN2 in $[N_{222}H][CF_3COO]$.

In this section, we discuss the reaction scheme of each case from the observed fluorescence kinetic in the previous section. Scheme 3-1(a) shows a standard PT reaction of 5CN2 as reported previously.[3] In the present work, the reaction of 5CN2 in $[N_{222}H][CH_3SO_3]$ corresponds to this case, although, at present, the chemical species of the proton acceptor is not clear. As will be discussed later, we consider that water contaminated in PILs is the acceptor of proton. According to the reaction scheme 3-1(a), the time-profile of the concentration of each species is given as follows by assuming that k_d, $k_p[H^+] >> k_0$, k'_0,[20]

$$[ROH^*] = [ROH^*]_0 \frac{k_d}{k_1}\left\{\exp(-k_1 t) + \frac{k_p[H^+]}{k_d}\exp(-k_s t)\right\} \quad (3.3)$$

$$[RO^{-*}] = [ROH^*]_0 \frac{k_d}{k_1}\{-\exp(-k_1 t) + \exp(-k_s t)\} \quad (3.4)$$

where,

$$k_1 = k_p[H^+] + k_d \quad (3.5)$$

$$k_s = \frac{k'_0 k_\mathrm{d} + k_0 k_\mathrm{p}[\mathrm{H}^+]}{k_\mathrm{d} + k_\mathrm{p}[\mathrm{H}^+]} \tag{3.6}$$

The equation of RO^{-}* (eq (3.4)) successfully describes the experimentally observed fluorescence intensity where the rise and decay amplitudes are the same. The observed rise components corresponds to the PT rate (0.09 ns^{-1}) in $[N_{222}H][CH_3SO_3]$, which is quite slow in comparison with that in the aqueous system (0.07 ps^{-1}).[21] On the other hand, there are some discrepancy on the experimentally observed fluorescence intensity dynamics of ROH* from eq. (3.3). In experimental observation, as is shown in Figure 3-7 (a), a quite fast decay component (1.36 ns^{-1}) was observed for ROH*. We are not sure of the origin of this constant, which may be due to some relaxation process specific to PILs. In addition, the slowest decay component (0.03 ns^{-1}) corresponding to the decay kinesis of RO^{-}* was absent in the kinetics of ROH*. This may be ascribed to the small contribution of the backward PT, and to the difficulty of the spectral separation of spectrum of very weak intensities by log-normal functions.

For the cases where three species exist, we consider Scheme 3-1 (b) as the most general one. According to the Scheme 3-1 (b), rate equations are given as follows;

$$\frac{d}{dt}[\mathrm{ROH}^*] = -(k_{\mathrm{d}1} + k_0 + k_{\mathrm{d}3})[\mathrm{ROH}^*] + k_{\mathrm{p}1}[\mathrm{H}^+][\mathrm{Y}^{-*}] + k_{\mathrm{p}3}[\mathrm{H}^+][\mathrm{RO}^{-*}] \tag{3.7}$$

$$\frac{d}{dt}[\mathrm{Y}^{-*}] = k_{\mathrm{d}1}[\mathrm{ROH}^*] - \left(k_{\mathrm{p}1}[\mathrm{H}^+] + k_{\mathrm{d}2} + k_{0\mathrm{Y}}\right)[\mathrm{Y}^{-*}] + k_{\mathrm{p}2}[\mathrm{RO}^{-*}] \tag{3.8}$$

$$\frac{d}{dt}[\mathrm{RO}^{-*}] = k_{\mathrm{d}3}[\mathrm{ROH}^*] + k_{\mathrm{d}2}[\mathrm{Y}^{-*}] - (k_{\mathrm{p}3}[\mathrm{H}^+] + k_{\mathrm{p}2} + k'_0)[\mathrm{RO}^{-*}] \tag{3.9}$$

The general solutions of these equations are quite complicated and useless. We have made some simplification to extract the essential parts of the reaction. First, we have neglected the backward reactions from RO^{-}* ($k_{\mathrm{p}3} = k_{\mathrm{p}2} = 0$). By considering that the appearance of Y^{-}* and RO^{-}* was faster than the fluorescence decay due to the radiative and nonradiative decay processes, we have also neglected k_0 and $k_{0\mathrm{Y}}$. Further we have assumed that the

concentration of proton ([H^+]) is time-independent, that the initial concentrations of Y^{-}* and RO^{-}* are zero, and that $k_{d1} >> k_{d2}$, k_{d3}, $k_{p1} >> k'_0$. Based on these assumptions, eqs (3.7), (3.8), (3.9) are approximately solved to give the following answers;

$$[\mathrm{ROH}^*] = [\mathrm{ROH}^*]_0 \frac{1}{k_{\mathrm{d1}} + k_{\mathrm{p1}}[\mathrm{H}^+]} \left\{ k_{\mathrm{p1}} [\mathrm{H}^+] \exp(-k_{\mathrm{d2}} t) + k_{d1} \exp(-k_{\mathrm{m}} t) \right\} \quad (3.10)$$

$$[\mathrm{Y}^*] = [\mathrm{ROH}^*]_0 \frac{k_{d1}}{k_{\mathrm{d1}} + k_{\mathrm{p1}}[\mathrm{H}^+]} \{ \exp(-k_{d2} t) - \exp(-k_m t) \} \quad (3.11)$$

$$[\mathrm{RO}^{-*}] = [\mathrm{ROH}^*]_0 \{ P \exp(-k'_0 t) + Q \exp(-k_{\mathrm{d2}} t) + R \exp(-k_{\mathrm{m}} t) \} \quad (3.12)$$

where

$$k_{\mathrm{m}} = k_{\mathrm{d1}} + k_{\mathrm{d3}} + k_{\mathrm{p1}}[\mathrm{H}^+] \quad (3.13)$$

$$P = -Q - R \quad (3.14)$$

$$Q = \frac{(k_{\mathrm{d3}} k_{\mathrm{p1}}[\mathrm{H}^+] + k_{d1} k_{\mathrm{d2}})}{(k_{\mathrm{d1}} + k_{\mathrm{p1}}[\mathrm{H}^+])(k'_0 - k_{\mathrm{d2}})} \quad (3.14)$$

$$R = \frac{k_{\mathrm{d1}}(k_{\mathrm{d3}} - k_{\mathrm{d2}})}{(k_{\mathrm{d1}} + k_{\mathrm{p1}}[\mathrm{H}^+])(k'_0 - k_{\mathrm{m}})} \quad (3.14)$$

The fitting result for 5CN2 in [N_{222}H][CF_3COO] seems to correspond to the model case calculated here, although there are some discrepancies of the coefficients. In this case, the fastest rate constant corresponds to k_{m} (= 2.40 ns^{-1}), and the second fastest rate constant corresponds to k_{d2} (= 0.14 ns^{-1}). For other cases, similar correspondence should be applicable, although the discrepancies from the model are more apparent.

3.4.2. Assignment of the New Components

From the analysis of the kinetics, Y^{-}* is considered to be a reaction intermediate. Furthermore, the stability of Y^{-}* is strongly affected by water contaminated in PILs. As is mentioned in Introduction, the pK_a* values of 5CN2 and DCN2 in aqueous solution have been reported to be -0.75[17] and -4.5,[19] respectively. The pK_a values of conjugate acids of the anions used here are -12 (CF_3SO_3H), -2 (CH_3SO_3H), 0.23 (CF_3COOH). If

this acidity holds in PILs, CF_3COO^- can be a proton acceptor from 5CN2, and $CH_3SO_3^-$ and CF_3COO^- can be proton acceptors from DCN2. These cases for the prediction of the occurrence of PT correspond to the experimental cases where Y^-* is observed. Therefore, we consider that Y^-* is the species which resulted from the direct PT from the solute to the solvent anion; the complex RO^-* with the protonated anion. The complex is temporally solvated and stabilized by surrounding cation and anion. Then the question is what is the origin of the fluorescence band assigned to RO^-*. Since the species generally appeared after the formation of Y^-*, we consider this species is RO^-* which has no specific interaction with a protonated conjugate acid. The species may be derived from the dissociation of the complex Y^-* or from the direct PT of ROH* to H_2O contaminated in PIL. As mentioned in the steady-state fluorescence, the intensity of Y^-* decreased and that of RO^-* increased with an addition of water. The spectral position of RO^-* is close to that in aqueous solutions. All these facts support the idea.

3.4.3. Formation of New Components: Comparison with Solvation Dynamics

Since the proton transfer reaction is short ranged one, the formation of the encounter complex can be the rate limiting. If the formation of the encounter complex is diffusion controlled, the rate coefficient k_D (s^{-1}) can be estimated to be

$$k_D = \frac{2}{3}\frac{k_B T}{\eta}[M], \tag{3.15}$$

where k_B is Boltzmann constant, T the absolute temperature, η is viscosity of the solvent, and [M] the concentration of the proton acceptor. If the proton acceptor is the anion, the value of k_D is estimated to be an order of 10^{-1} ns^{-1}, considering that the concentration of anion in $[N_{222}H][CH_3SO_3]$ is about 5 M and the viscosity of $[N_{222}H][CH_3SO_3]$ at room temperature is 100 mPa s.[22] The value is close to k_1 estimated

from the time profile of the fluorescence, indicating the validity of assignment of the species Y^{-}*.

Considering that the formation of Y^{-}* is diffusion-limited process of ROH* and proton acceptor, it could compete with solvation dynamics upon photoexcitation of ROH*. Although peak position of ROH* should red-shifted due to solvation dynamics upon photoexcitation, we couldn't extract whole time-profile of the dynamic Stokes shift of ROH* from the time-resolved spectrum where Y^{-}* was observed, because their band positions are neighboring (see Figure 3-5 and 3-6). To discuss how solvation dynamics affected to the formation kinetics of Y^{-}*, we measured time-resolved spectrum of methoxy form of DCN2 (MeDCN, see Figure 3-9) that does not undergo PT. In order to determine the solvation dynamics with enough time resolution, we applied the optical Kerr-gate system whose time-resolution is approximately 0.2 ps.

Figure 3-9 is time-resolved fluorescence spectrum of MeDCN in $[N_{222}H][CH_3SO_3]$

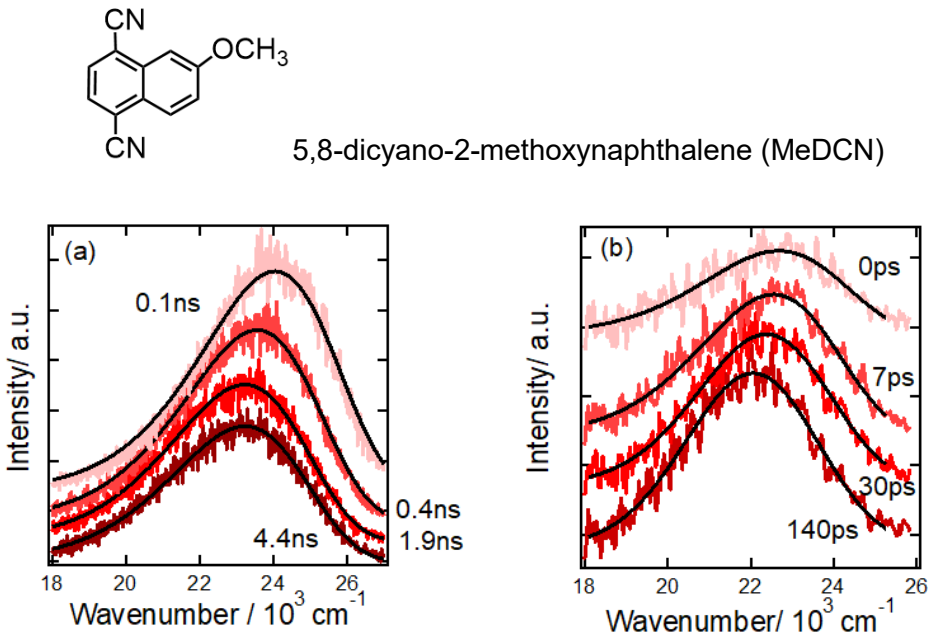

Figure 3-9. Time-resolved fluorescence spectrum of MeDCN in $[N_{222}H][CH_3SO_3]$ obtained by (a) streak camera measurements and (b) optical Kerr-gate measurements.

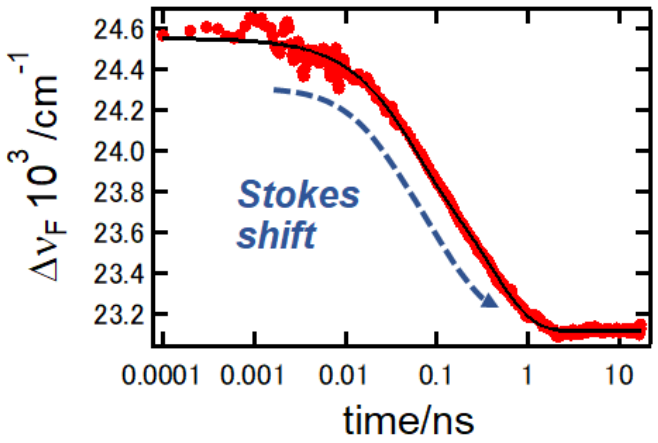

Figure 3-10. Dynamic Stokes shift of MeDCN in $[N_{222}H][CH_3SO_3]$.

measured by streak camera (time resolution is ~20ps) and Kerr-gated method. Peak position of MeDCN shows bathochromic shift with time upon the photoexcitation. Figure 3-10 (a) shows time-profile of peak position obtained from the fitting the spectrum at each time to log-normal function (eq. (3.1)). This time-profile was fit to double exponential function. We got time constants for reorientation of solvent PILs (τ_1 = 60 ps and τ_2 = 470 ps)

Figure 3-11 is time-resolved fluorescence spectrum of DCN2 in $[N_{222}H][CH_3SO_3]$ obtained by Kerr-gate method. Upon the photo-excitation, fluorescence from ROH* appeared in 3 ps and are replaced by fluorescence from Y^-* in several hundred picoseconds. By simulating the time-resolved spectrum with sum of log-normal function as noted above, we obtained the time-profile of fluorescence intensity. Figure 3-11 (b) shows time-profile of fluorescence intensity of ROH* and Y^-*. The time-profile of each species were fit by tri-exponential function. Fitting results are summarized in Appendix B3. We found that fastest time-constant for decay of ROH* and rise of Y^-* is identical (τ_1 = 72 ps), which demonstrates Y^-* is not existed in the ground state and generated from ROH* after the excitation. It is also noted that the fastest time constant is approximately

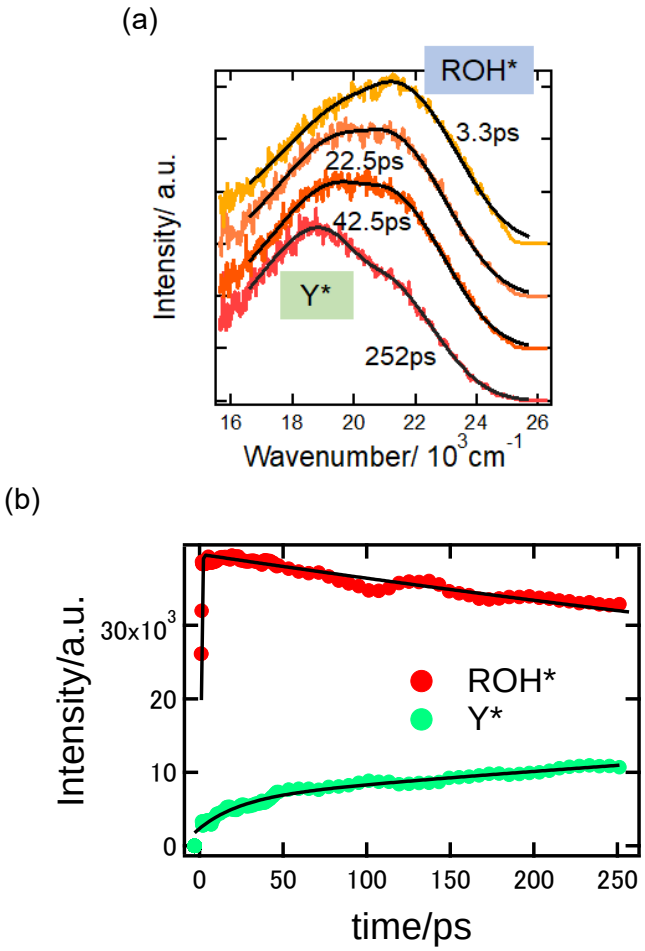

Figure 3-11. Time-resolved fluorescence spectrum of DCN2 obtained by Kerr-gate method (a) and time-profile of fluorescence intensity of DCN2 in $[N_{222}H][CH_3SO_3]$ (b).

the same as that is obtained as solvation dynamics. Therefore, we concluded solvation dynamics around ROH* contributes the formation kinetics of Y^-*, which means that Y^-*is generated while anion of PIL reorients around ROH* upon the photoexcitation.

Before concluding this section, we mention the proton transfer dynamics observed for 5CN2 in $[N_{222}H][CH_3SO_3]$. According to the discussion in the previous paragraph, $CH_3SO_3^-$ is not the proton acceptor from 5CN2. Therefore, water contained in the PIL should be the proton acceptor in the case. By roughly estimating the water concentration (7.4 mol m^{-3}) and the viscosity of the PILs (100 mPa s),[8] the value of k_D is estimated to be 1.2×10^{-4} ns^{-1}. The value is about 10^4 times slower than the experimental value k_{d1}.

A plausible explanation to this is as follows. When the concentration of water is low, it locates between anion and cation of PILs due to the existence of the preferred interaction sites for water in PILs.[8, 23] The large difference between the theoretical and experimental value may reflect such heterogeneously located water molecules.

3.5. Conclusions

In this study, we investigated the ESPT dynamics of 5CN2 and DCN2 in three different PILs by steady-state and time-resolved fluorescence measurements. To sum up briefly, the occurrence of PT of these photoacids in PILs was simply explained by the basicity of the anions of PILs. In $[N_{222}H][CF_3SO_3]$ fluorescence from RO^-* was not observed for both 5CN2 and DCN2, indicating that ESPT did not occur in $[N_{222}H][CF_3SO_3]$. For 5CN2 in $[N_{222}H][CH_3SO_3]$, we confirmed the fluorescence from RO^-* by the steady-state and time-resolved fluorescence measurement. Most interestingly, in the case of 5CN2 in $[N_{222}H][CF_3COO]$ and DCN2 in $[N_{222}H][CH_3SO_3]$ and $[N_{222}H][CF_3COO]$, a new fluorescence component (Y^-*) at around 460 nm was observed. According to the analysis of the time dependent fluorescence spectra, we proposed the plausible reaction schemes of each case. From these schemes and the rate coefficients, it was suggested that Y^-* was generated by proton dissociation of ROH*, and the kinetics of Y^-* depended on the acidity of PILs and solute molecule. In the present case, the PT is slow comparable to the solvation dynamics of the solvent, and it was found that the complex formation is correlated with the solvation dynamics. Exploration of other kinds of PT reactions will enrich the field of the PILs as will be mentioned in the general conclusion (Chapter 6).

Appendix B

Table of Contents

B1. Synthesis of 5-cyano-2-naphthol

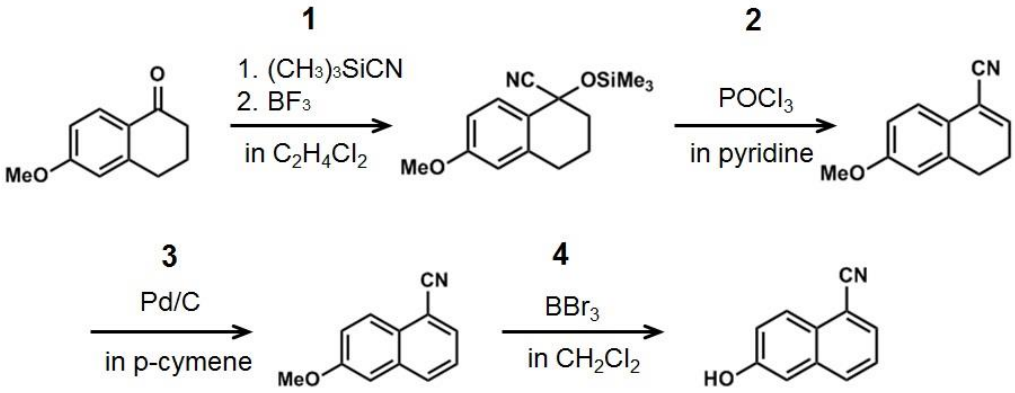

Scheme B1 Synthesis of 5CN2. For experimental details, see: ref. 25 (reactions 1, 2) and ref. 24 (reactions 3, 4).

B2. Experimental Setup for Kerr Gate Fluorescence Measurement

The details of the optical Kerr gate measurements are described elsewhere.[16] Briefly a part of output from the Ti:Sapphire Laser was used to operate OPA to produce the excitation pulse (370 nm). A part of fundamental output (800 nm) was used to operate optical Kerr gate. The fluorescence from the sample was initially undetected using a pair of polarizers of diagonal orientation. The fluorescence from the sample was focused on the Kerr media (benzene) between the two polarizers. When the gate pules (800 nm) was incident on the Kerr media, the fluorescence from the sample was rotated due to the temporal birefringence and passed through the second polarizer. The fluorescence was detected by the intensified CCD camera (Lavision, Picostar HR). By changing the timing between the excitation and gate pulses using the optical delay line, time resolved fluorescence was measured. A flow type optical cell with optical path lengths of 0.5 mm or 1 mm was used for the measurement. The sample solution was circulated using a micro-gear pump (mzr-2905, HNP Mikrosysteme) at a flow rate of 1 or 2 mL min^{-1}. All measurements were performed at room temperature (around 21.0 °C).

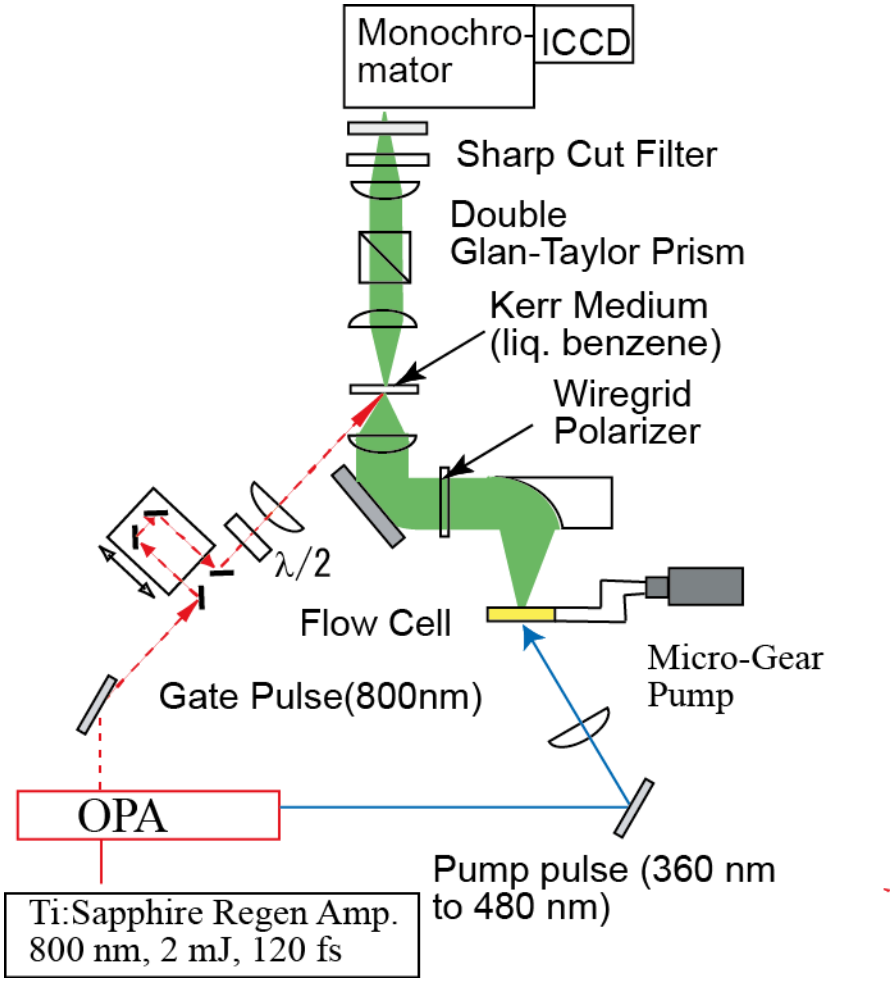

Figure B1. Schematic illustration of the experimental setup for the optical Kerr gate experiment.

B3. Rate Constants for Proton Transfer and Solvation dynamics

Table B1. Time constants of DCN2 for the PT reaction and of MeDCN for the solvation dynamics in $[N_{222}H][CH_3SO_3]$.

	A_1	A_2	A_3	τ_1 / ps	τ_2 / ps	τ_3 / ps
DCN2 (ROH*)	1	28.0	62.5	72	392	6000
DCN2 (Y^-*)	-18.4	0	25.2			
MeDCN	1	1.12	-	60	470	-

References

1. Belieres, J.-P.; Angell, C. A., Protic Ionic Liquids: Preparation, Characterization, and Proton Free Energy Level Representation. *The Journal of Physical Chemistry B* **2007,** *111* (18), 4926-4937.

2. Fumino, K.; Reimann, S.; Ludwig, R., Probing molecular interaction in ionic liquids by low frequency spectroscopy: Coulomb energy, hydrogen bonding and dispersion forces. *Physical Chemistry Chemical Physics* **2014,** *16* (40), 21903-21929.

3. Fumino, K.; Fossog, V.; Wittler, K.; Hempelmann, R.; Ludwig, R., Dissecting Anion–Cation Interaction Energies in Protic Ionic Liquids. *Angewandte Chemie International Edition* **2013,** *52* (8), 2368-2372.

4. Shmukler, L. E.; Gruzdev, M. S.; Kudryakova, N. O.; Fadeeva, Y. A.; Kolker, A. M.; Safonova, L. P., Thermal behavior and electrochemistry of protic ionic liquids based on triethylamine with different acids. *RSC Advances* **2016,** *6* (111), 109664-109671.

5. Watanabe, H.; Doi, H.; Saito, S.; Matsugami, M.; Fujii, K.; Kanzaki, R.; Kameda, Y.; Umebayashi, Y., Hydrogen bond in imidazolium based protic and aprotic ionic liquids. *Journal of Molecular Liquids* **2016,** *217*, 35-42.

6. Zentel, T.; Kühn, O., A network approach to unravel correlated ion pair dynamics in protic ionic liquids. The case of triethylammonium nitrate. *Journal of Molecular Liquids* **2017,** *226*, 56-62.

7. Huang, Y.; Zhou, G.; Li, Y.; Yang, Z.; Shi, M.; Wang, X.; Chen, X.; Zhang, F.; Li, W., Molecular dynamics simulations of temperature-dependent structures and dynamics of ethylammonium nitrate protic ionic liquid: The role of hydrogen bond. *Chemical Physics* **2016,** *472*, 105-111.

8. Murphy, T.; Varela, L. M.; Webber, G. B.; Warr, G. G.; Atkin, R., Nanostructure–Thermal Conductivity Relationships in Protic Ionic Liquids. *The Journal of Physical Chemistry B* **2014,** *118* (41), 12017-12024.

9. Davidowski, S. K.; Thompson, F.; Huang, W.; Hasani, M.; Amin, S. A.; Angell, C. A.; Yarger, J. L., NMR Characterization of Ionicity and Transport Properties for a Series of Diethylmethylamine Based Protic Ionic Liquids. *The Journal of Physical Chemistry B* **2016,** *120* (18), 4279-4285.

10. Hasani, M.; Yarger, J. L.; Angell, C. A., On the Use of a Protic Ionic Liquid with a Novel Cation To Study Anion Basicity. *Chemistry – A European Journal* **2016,** *22* (37), 13312-13319.

11. Martinelli, A., Conformational Changes and Phase Behaviour in the Protic Ionic Liquid 1-Ethylimidazolium Bis(trifluoromethylsulfonyl)imide in the Bulk and Nano-Confined State. *European Journal of Inorganic Chemistry* **2015,** *2015* (7), 1300-1308.

12. Watanabe, H.; Doi, H.; Saito, S.; Sadakane, K.; Fujii, K.; Kanzaki, R.; Kameda, Y.; Umebayashi, Y., Raman Spectroscopic Speciation Analyses and Liquid Structures by High-Energy X-ray Total Scattering and Molecular Dynamics Simulations for N-methylimidazolium-Based Protic Ionic Liquids. *Bulletin of the Chemical Society of Japan* **2016,** *89* (8), 965-972.

13. Kano, K. Theory of Organic Reaction. *Sankyo publishing, Tokyo,* **2006**.

14. Sabourin, E. T.; Onopchenko, A., A convenient synthesis of 4-ethynylphthalic anhydride via 2-methyl-3-butyn-2-ol. *The Journal of Organic Chemistry* **1983,** *48* (25), 5135-5137.

15. Gingrich, D. E.; Lisko, J. G.; Curry, M. A.; Cheng, M.; Quail, M.; Lu, L.; Wan, W.; Albom, M. S.; Angeles, T. S.; Aimone, L. D.; Haltiwanger, R. C.; Wells-Knecht, K.; Ott, G. R.; Ghose, A. K.; Ator, M. A.; Ruggeri, B.; Dorsey, B. D., Discovery of an Orally Efficacious Inhibitor of Anaplastic Lymphoma Kinase. *Journal of Medicinal Chemistry* **2012,** *55* (10), 4580-4593.

16. Suda, K; Terazima, M; Sato, H; Kimura, Y; Excitation Wavelength Dependence of Excited State Intramolecular Proton Transfer Reaction of 4´-*N*,*N*-diethylamino-3-hydroxyflavone in Room Temperature Ionic Liquids Studied by Optical Kerr Gate Fluorescence Measurement, *The Journal of Physical Chemistry B* **2013**, *117*, 12567-1258.2

17. Nunes, R. M. D.; Arnaut, L. G.; Solntsev, K. M.; Tolbert, L. M.; Formosinho, S. J., Excited-State Proton Transfer in Gas-Expanded Liquids: The Roles of Pressure and Composition in Supercritical CO2/Methanol Mixtures. *Journal of the American Chemical Society* **2005,** *127* (34), 11890-11891.

18. Solntsev, K. M.; Huppert, D.; Agmon, N., Photochemistry of "Super"-Photoacids. Solvent Effects. *The Journal of Physical Chemistry A* **1999,** *103* (35), 6984-6997.

19. Solntsev, K. M.; Huppert, D.; Agmon, N.; Tolbert, L. M., Photochemistry of "Super" Photoacids. 2. Excited-State Proton Transfer in Methanol/Water Mixtures. *The Journal of Physical Chemistry A* **2000,** *104* (19), 4658-4669.

20. Kobayashi, I.; Terazima, M.; Kimura, Y., Study of the Excited-State Proton-Transfer Reaction of 5-Cyano-2-naphthol in Sub- and Supercritical Water. *The Journal of Physical Chemistry B* **2012,** *116* (3), 1043-1052.

21. Huppert, D.; Tolbert, L. M.; Linares-Samaniego, S., Ultrafast Excited-State Proton Transfer from Cyano-Substituted 2-Naphthols. *The Journal of Physical Chemistry A* **1997,** *101* (25), 4602-4605.

22. Greaves, T. L.; Drummond, C. J., Protic Ionic Liquids: Evolving Structure–Property Relationships and Expanding Applications. *Chemical Reviews* **2015,** *115* (20), 11379-11448.

23. Yaghini, N.; Nordstierna, L.; Martinelli, A. Effect of Water on the Transport Properties of Protic and Aprotic Imidazolium Ionic Liquids- an Analysis of Self-Diffusivity, Conductivity, and Proton Exchange Mechanism. *Physical. Chemistry Chemical Physics.* **2014,** *16*, 9266-9275.

24. Reddy, P. A.; Reddy, A. B.; Reddy, G. R. Suzuki-Miyaura Cross-Coupling Reaction of Naphthyl Triflate with Indole Boronic Acids Catalyzed by a Recyclable Polymer-Supported N-Heterocyclic Carbene-Palladium Complex Catalyst: Synthesis of Naphthalene-Linked Bis-Heterocycles. *Journal of Heterocyclic Chemistry* **2013,** *50*, 1451-1453**.**

25. Jacobs, S. A.; Harvey, R. G. A Convenient Synthesis of 4-Ethynylphthalic Anhydride via 2-Methyl-3-Butyn-2-ol. *The Journal of Organic Chemistry* **1983,** *48*, 5135-5137.

Chapter 4

Solvation Dynamics of Ionic Liquids Viewed from Photodissociation Reaction

4.1. Introduction

In Chapters 2 and 3, we have taken up proton transfer kinetics and discussed how solvation and solvation dynamics affect the reaction kinetics. In viscous environment such as ionic liquids (ILs), chemical reaction would compete with reorientation process of solvent ILs, as we have seen in the last section of Chapter 3. In this chapter, we focus on that solvation dynamics of ILs triggered by photodissociation reaction.

We now have various experimental and theoretical methods to discuss solvation dynamics.[1-4] Experimentally, typical research on solvation phenomena has been done on the electronic spectra of probe molecules. One stream of these experimental researches has monitored the relaxation energy of fluorescent dye molecules upon photoexcitation, dynamic Stokes shift. Figure 4-1 is a schematic illustration of dynamic Stokes shift. When a solute molecule in the ground state (S_0 state) absorbs light whose wavenumber ($\Delta\nu$ cm^{-1}) corresponds to the energy gap between S_0 and S_1 state, the solute molecule is excited

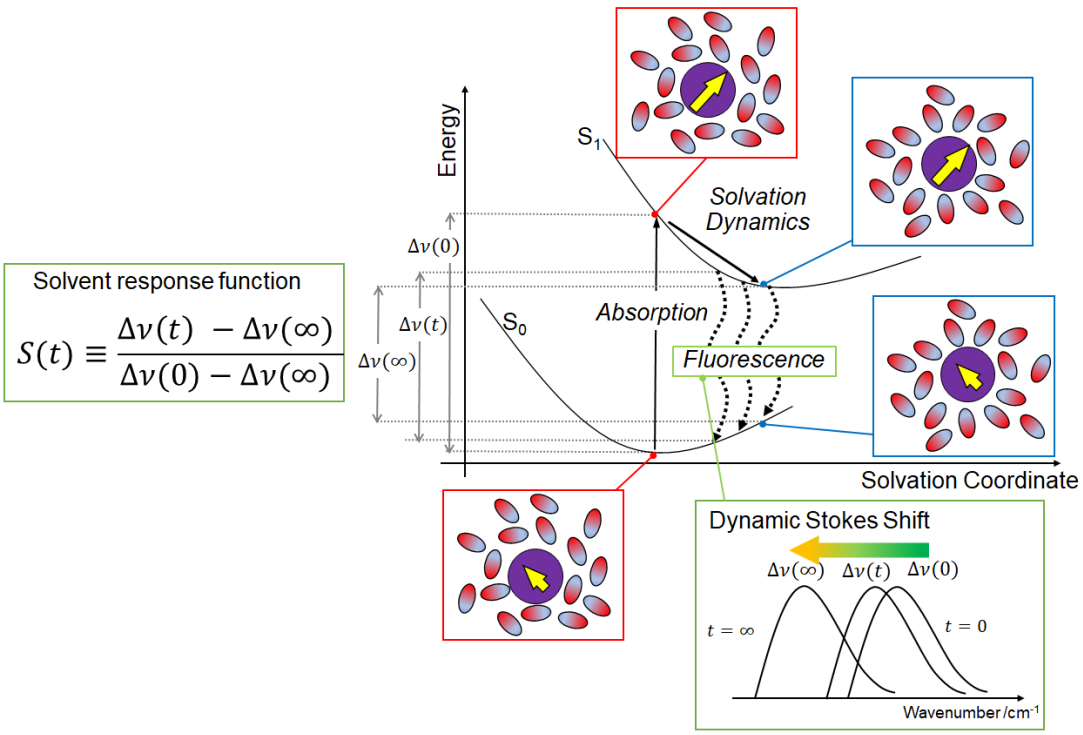

Figure 4-1 Solvation dynamics in the excited state probed by the dynamic Stokes-shift.

to Frank-Condon state, and charge redistribution inside the molecule is occurred. Since this event completes much faster than the motion of surrounding solvent molecules, surrounding solvent molecules start to reorient to lower the free energy in the solution. If the reorientation process, called solvation dynamics, undergoes within or coupled to the excited state lifetime of solute molecule, we observe the band position of fluorescence spectrum shifts to the lower energy with time (dynamic Stokes shift or red-shift). To assess the extent and time-profile of spectrum shift, solvent response function, $S(t)$ (functional form is shown in Figure 4-1), has been evaluated from the time profile of the fluorescence peak position. This response function, under the linear-response theory, is generally independent of the extent of perturbation under dipolar excitation, i.e., the extent of charge redistribution within solutes or types of solute molecule. However, more than a few groups have experimentally demonstrated the breakdown of this linear response theory[5] in the presence of specific solute–solvent interactions.[6-8] Chapman et al. examined the solute dependence of the solvation dynamics of 1-propanol.[6] Sixteen types of solute molecules with a wide range of chemical structures and physical properties, sizes, polarities, and changes in electronic distribution upon photoexcitation were tested, and the authors attributed the deviation from a linear response to the formation of hydrogen-bonding interactions between the solute and 1-propanol. Other groups have examined the dependence of probes on solvation dynamics in polar solvents by broadband fluorescence up-conversion methods, as well as how the orientational motion of the solute upon photoexcitation[7] or the formation of hydrogen bonds with the surrounding solvent drives the subsequent solvation dynamics.[8]

From theoretical side, molecular dynamics (MD) simulations are useful approach to testing the linear response theory and have been a long-standing theme since the 1990s.

Some of the pioneering works in the field were reported by Maroncelli and Fleming, in which the relaxation processes of water[9] and acetonitrile[10] around a monoatomic solute were examined by MD simulations. By applying various solute sizes, polarities, and charge jumps to the calculations, they proved that the solvent responds differently upon the electronic change ($S_0 \rightarrow S_1$ and $S_1 \rightarrow S_0$) when the charge jump is large enough, that is, linear response theory breaks down. Since then, MD simulations have been applied to more complex systems consisting of polyatomic solutes such as those used in spectroscopic studies to examine the solvent response function upon an electronic charge jump. Cichos et al.[11] investigated the solvation dynamics of methanol and acetonitrile around C153 and clarified the effect of the polarizability of the solute on the solvent response. They found that the time profiles of the solvent response function in the ground and excited states did not overlap in the case of methanol as a hydrogen-bonding solvent. Recently, the non-linearity of the solvent response has regained focus in several groups.[12-15]

Numerous theoretical studies on the solute dependence of the solvent response function have been reported. On the other hand, from the experimental side, most reports have focused on the probe dependence of solvation dynamics. To the best of our knowledge, there have been no reports on the solvation dynamics of both the ground and excited state of a particular molecule. One representative spectroscopic method to observe solvation dynamics in the ground state is to monitor the hole-burning process via the transient absorption spectra.[16-18] A narrow hole produced by light absorption is inhomogeneously broadened by solvent reorganization as the system reaches an equilibrium state. Despite its great importance, there have been few experimental studies on this phenomenon because probe molecules suitable for investigating the solvation of

both the ground and excited state are limited. Additionally, it is difficult to experimentally produce non-equilibrium transient species in the ground state and to extract spectral shifts from the time evolution of transient absorption spectra due to the different contributors to the transient absorption signal, such as induced emission and excited-state absorption.

In this study, we demonstrated the solvation dynamics of both the electronically excited state and ground state of the same molecule using transient absorption and time-resolved fluorescence spectroscopy. We chose bis(*p*-aminophenyl) disulfide (BPADS) as the probe molecule and monitored the time-resolved spectra after photodissociation. BPADS undergoes S–S bond dissociation by irradiation with a UV (~270 nm) pulse to generate a pair of *p*-aminophenylthiyl (PAPT) radicals (see Figure 4-2). This process is accompanied by a significant change in the dipole moment orientation of the probe molecule. As is shown in Figure 4-2, the PATP radical absorbs light at approximately 570 nm and is promoted to an electronically excited state (D_2 state), then relaxes to the ground state by emitting light at approximately 650 nm.[19-21] There have been several time-resolved spectroscopic studies on the photodissociation of BPADS.[22-30] Among them, Bultmann and Ernsting[27] performed detailed measurements of the transient absorption spectra after photodissociation in a polar solvent and elucidated the competing processes of solvent

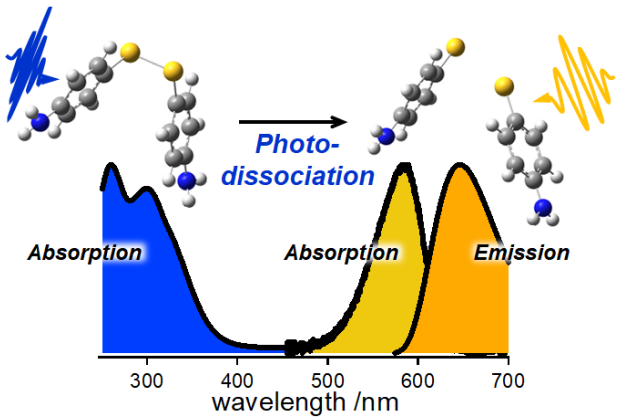

Figure 4-2. Photo-dissociation reaction of BPADS and change in the absorption spectrum.

reorganization and conformational changes of the geminate PAPT radicals. However, no study has measured the time-resolved spectra in both the ground state (D_0 state) and excited state (D_2 state).

To monitor the solvent relaxation process after photodissociation, we measured the time-resolved absorption spectra using conventional transient absorption spectroscopy after photodissociation of the disulfide bond of BPADS using a UV pulse. To observe the time-resolved emission spectra of the PAPT radical, we employed a two-step photoexcitation spectroscopic system. The PAPT radical generated by photodissociation is further excited to the D_2 state by another excitation pulse irradiated several picoseconds after photodissociation, and the time-resolved emission spectra are monitored by a streak camera.

Thus far, experimentally, solvation dynamics of ILs have been investigated by several groups. Ultrafast components whose time-range is several hundred femtoseconds, is assigned to the inertial motions of cations and anions. [37] The longer time-components of solvent response function, lying between several picoseconds to nanoseconds, are often simulated by a multi-exponential function or a stretched exponential function, where several dynamics of solvent, rotation or translation of cations and anions contributes to the signal. [38] Using analytical[39] and computational methods,[40,41] several groups have assigned these components to the specific motion of anions and cations.[42] Generally, the averaged solvation time is correlated with the solvent viscosity.

We observed unique energy relaxation around the photodissociated radical by time-resolved spectroscopic measurements. In the ground state, the solvent molecules reorganize to stabilize the photodissociated radicals, which results in a red-shift in the absorption spectrum of the radical. In the excited state, on the other hand, the emission

spectrum does not shift to a lower energy, indicating that no energy relaxation process occurs. To further examine the local solvation environment and energy relaxation processes in both the ground and excited state along the solvation coordinates, we conducted non-equilibrium MD simulations and discussed the experimental results by calculating the solute–solvent interaction energies and solvent distribution functions.

4.2. Experiment

4.2.1. Materials

BPADS was purchased from ALDRICH and recrystallized in MeOH before use. As solvents, we selected several phosphonium ILs (P_{nnnm}) and ammonium ILs (N_{nnnm}) with different alkyl chain lengths (*n* and *m* indicate the carbon number in the alkyl chain; see

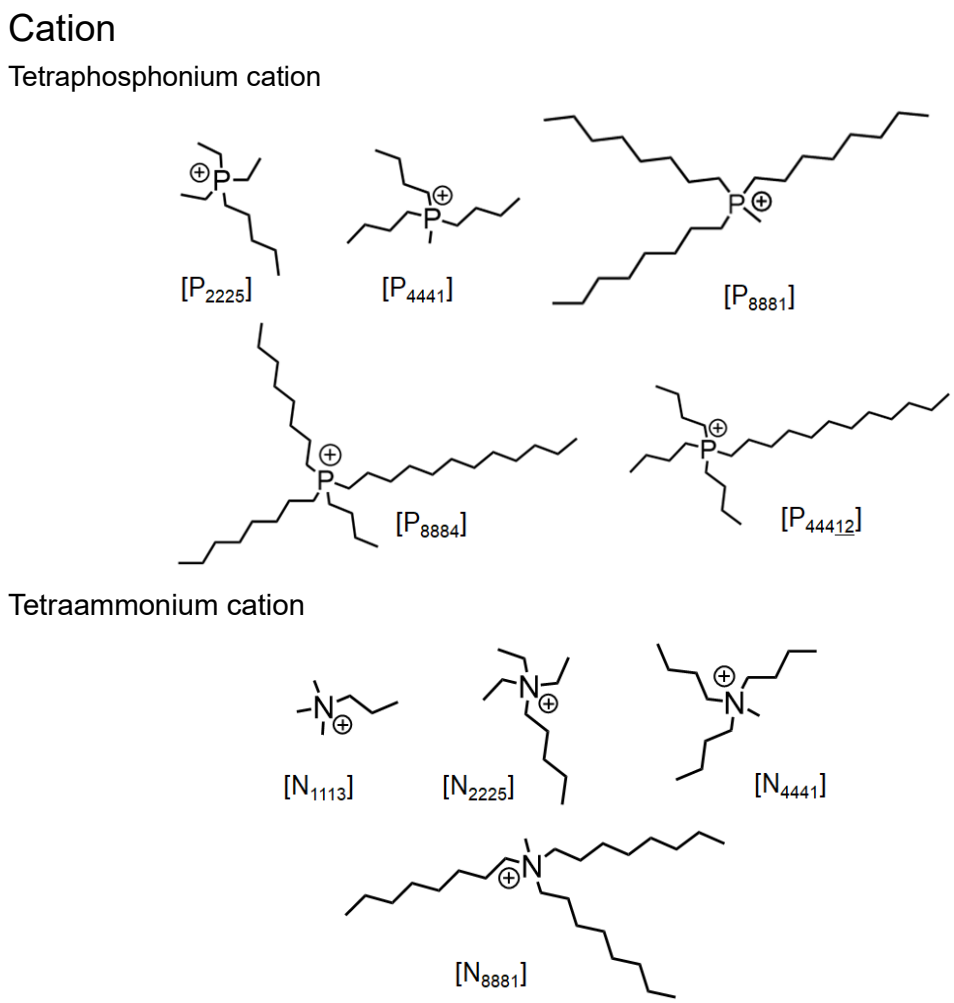

Figure 4-3. Structure of cation species of ILs. Anion is Bis(trifluoromethanesulfonyl) imide (NTf_2^-).

Figure 4-3), since they are transparent in the UV region. $[P_{2225}][NTf_2]$ and $[N_{1113}][NTf_2]$ (>99.9%) were purchased from KANTO CHEMICAL and used without further purification. The other ILs were synthesized in our laboratory according to our previous paper.[43] The procedures to obtain the ammonium ILs ($[N_{2225}][NTf_2]$, $[N_{4441}][NTf_2]$, and $[N_{8881}][NTf_2]$) are summarized in the Appendix C1. The purity of the synthesized ILs (>99.9%) was confirmed by ^{13}C and ^{19}F NMR spectroscopy. All ILs were dried in vacuum under 1 Pa at 65 ℃ before use.

4.2.2. Time-resolved Spectroscopic Measurements

Figure 4-4 shows systematic illustration of spectroscopic system for transient absorption and time-resolved emission spectrum measurements. Briefly, the light source used for the experiments was an amplified Ti:sapphire laser (800 nm, 1 kHz, 120 fs). For

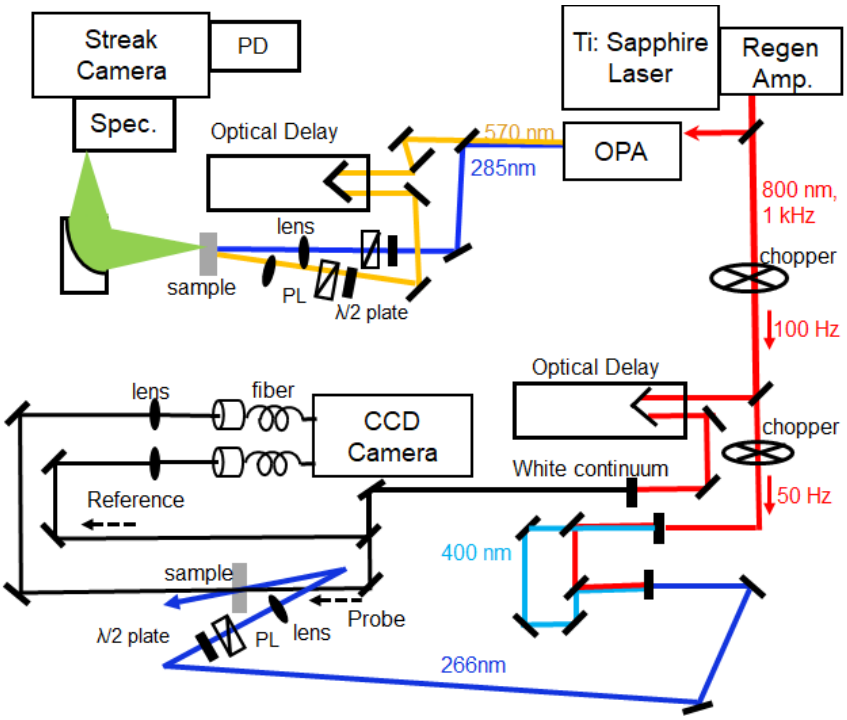

Figure 4-4. Spectroscopic system for the transient absorption (downward) and time-resolved emission spectrum measurement(upward).

the transient absorption measurements, the excitation pulse was the third harmonic output (266 nm), and the probe pulse was generated by focusing the fundamental pulse onto a CaF_2 plate. Time-resolved spectra with and without a pump pulse ($\Delta OD(\lambda,t)$) were obtained at different delay times after photoexcitation by a CCD camera (PIXIS 400, Princeton Instruments) attached to a spectrometer (Acton SpectraPro SP2150, Princeton Instruments). The time step of the delay of probe pulse (Δt) to the pump pulse was changed in three time-windows: Δt = 0.2 ps for −2 ps ~10 ps, Δt =2 ps for 10 ps~ 60 ps and Δt =20 ps for 60 ps~1000 ps. Spectroscopic data was analyzed by averaging 8 scans.

To measure the fluorescence from the transient radical, two-step excitation was employed. After excitation of the sample solution by a UV pump pulse (285 nm) produced by an optical parametric amplifier (OPA) and a BBO crystal, the produced radical was photoexcited by another excitation pulse (570 nm, output from OPA) after the selected time delay. The fluorescence from the radical was detected by a streak camera attached to a spectrometer. The color sensitivity and time shift of the streak camera were corrected as done previous section. Since the emission from PAPT radical was overloaded by background emissions caused by the UV pump pulse and/or the radical excitation pulse, we subtract the background emission measured at the same intensity of pump pulses from the spectrum that includes the radical emission. This treatment was conducted before the color-sensitivity and time shift correction of the detector.

4.2.3. Computational Methods

Non-equilibrium MD simulations of the photodissociation dynamics were carried out for the system of BAPDS or the PAPT radical pair in two ILs, $[P_{4441}][NTf_2]$ and $[P_{8881}][NTf_2]$. We first determined the structural and charge parameters of BPADS and

the PAPT radical by DFT calculations using the Gaussian 09 program[44]. The optimized structure of BPADS was obtained at the B3LYP /6-31G+(d, p) level. For the PAPT radical, unrestricted B3LYP was applied as the functional set, and the optimized structures in the electronically excited states were also calculated using the TD-DFT method. Table C2-1 (a–c) summarizes the optimized structures of these molecules (*xyz* coordinates and ESP (electrostatic potential) charge of each atom). To determine the potential parameters of each molecule for MD simulations, the structural parameters (bond lengths, dihedral angles, and ESP charges) of BPADS were corrected to have mirror symmetry across the vertical plane containing the C–N and C–S bonds of the phenyl rings, and the ESP charges of the S atoms of BPADS and the PAPT radical were slightly modified to neutralize the charge of the molecules (see Appendix C2).

MD simulations were performed for two ILs ($[P_{4441}][NTf_2]$ and $[P_{8881}][NTf_2]$) using GROMACS (version 2018. 7)[45,46]. OPLS-AA was used for the force field. The intramolecular force constants and Lennard-Jones parameters for BPADS and the PAPT radical were taken from conventional OPLS-AA parameters. The intramolecular force constants and Lennard-Jones parameters for BPADS and the PAPT radical were taken

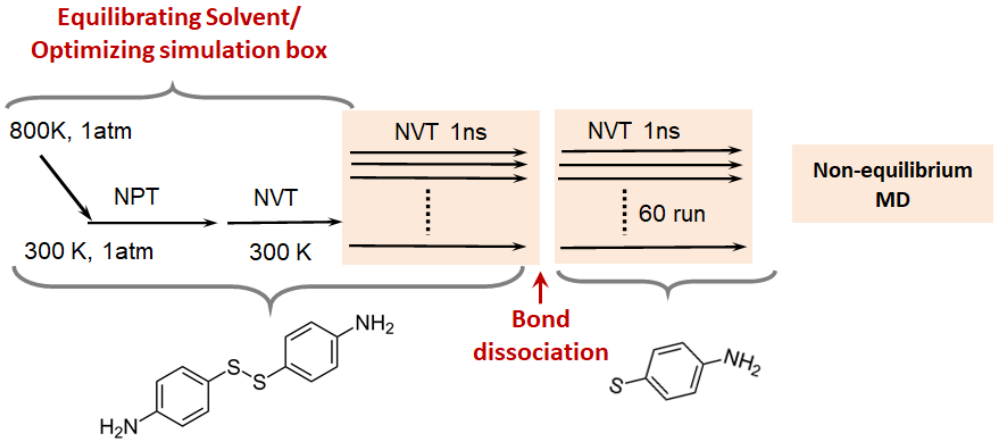

Scheme 4-1 Schematic illustration for the procedure of non-equilibrium MD simulation.

from conventional OPLS-AA parameters. Since the parameters of the sulfur radical was not found, we used the parameter for the sulfur atom of thiophenol. The potential parameters of cations and anions are taken from the work by Lopes and coworkers[47,48]. Scheme 4-1 illustrates the procedure to equilibrate solvent ILs and to simulate photodissociation process. A system of one solute molecule (BPADS) and 500 ion pairs were appropriately prepared by an annealing procedure, and simulation runs were performed in the NVT ensemble at 300 K (see details in the Appendix C2). From the long simulation run (30 ns), we obtained the self-diffusion coefficients of the P_{4441} cation, P_{8881} cation, and NTf_2 anion in each IL. The optimized box size and physicochemical parameters (density and self-diffusion coefficient) together with some experimental values are summarized in Appendix C2 (Table C2-2). As is shown in the Table C2-2, density and diffusion coefficients of $[P_{4441}][NTf_2]$ were reasonably reproduced by the simulation, while the diffusion coefficients of $[P_{8881}][NTf_2]$ were found to be larger than those of $[P_{4441}][NTf_2]$. Since the experimentally determined viscosity of $[P_{8881}][NTf_2]$ is larger than that of $[P_{4441}][NTf_2]$, the result of the simulation may be unreasonable, although the density of $[P_{8881}][NTf_2]$ was reasonably reproduced by the simulation. Therefore, we only discuss the equilibrium structure for $[P_{8881}][NTf_2]$, and the dynamics will be discussed only for $[P_{4441}][NTf_2]$,

To estimate the solvation dynamics in the ground and excited states, we prepared 60 simulation boxes containing a solution of BPADS with different configurations by the annealing procedure described in Appendix C2.2. After a 1 ns run for each simulation box, the potential parameters of BAPDS were replaced with those of the PAPT radical in the ground state (D_0^{eq} in Table 4-1) to simulate the photodissociation reaction. The solution of the PAPT radical pair was then simulated for 1 ns in the NVT ensemble. The

Table 4-1. Name of potential set of PAPT radical carried into MD simulation. The value inside the parenthesis represents dipole moment in each state.

		Electronic state	
		D_0	D_2
Structure optimized	D_0	D_0^{eq} (6.15 D)	D_2^{noneq} (8.7 D)
	D_2	D_0^{noneq} (6.13 D)	D_2^{eq} (9.3 D)

photoexcitation process of the PAPT radical to the electronically excited state (D_2 state) was simulated by a similar procedure as that for the photodissociation process. After a certain period of simulating the PAPT radical pair in the ground state, the potential set of the PAPT radical was replaced with that of the excited state (D_2^{eq} in Table 4-1). The timing to excite the PAPT radical was 10 or 1000 ps after dissociation.

To discuss the experimentally obtained spectral shifts, we extracted the time profiles of the solvation energy differences corresponding to the $D_0 \rightarrow D_2$ or $D_2 \rightarrow D_0$ vertical transition by the following procedure. For the $D_0 \rightarrow D_2$ vertical transition (absorption), we first calculated the ground-state solute–solvent interaction energy ($E_{GS}(t)$) according to the trajectory simulated with the optimized D_0^{eq} potential parameter. Then, the trajectory was retraced by replacing the D_0^{eq} potential with the D_2^{noneq} potential, and the interaction energy between the PAPT radical in the D_2 state and the solvent was extracted every 200 fs ($E_{ES\text{-}FC}(t)$, FC means Frank-Condon state). Subtracting these profiles ($E_{GS}(t) - E_{ES\text{-}FC}(t)$) yielded the time profile of the energy difference corresponding to absorption. A similar procedure was employed to obtain the energy profile for the $D_2 \rightarrow D_0$ vertical transition (emission). First, we calculated the time profile of the interaction energy between the PAPT radical in the D_2 state and the solvent ($E_{ES}(t)$) by the trajectory simulated with the optimized D_2 potential parameter (D_2^{eq} in Table 4-1). Then, the time profile of the interaction energy in the FC D_0 state ($E_{GS\text{-}FC}(t)$) with the solvent was

calculated by retracing the simulation trajectory and replacing the D_2^{eq} potential with the D_0^{noneq} potential. Finally, subtracting these profiles ($E_{ES}(t) - E_{GS\text{-}FC}(t)$) yielded the time profile of the energy difference corresponding to emission. These time profiles were averaged over 60 trajectories.

4.3. Results and Discussion

4.3.1. Spectrum Dynamics After the Photodissociation

Figure 4-5 shows the transient absorption spectra after photodissociation of the PAPT radical in (a) $[P_{4441}][NTf_2]$ and (b) $[P_{8881}][NTf_2]$. The band at approximately 17000 cm^{-1} corresponds to the PAPT radical generated by S–S bond dissociation. It is also apparent that the absorption peak shifts to a lower energy with time, indicating that solvent reorganization occurs to stabilize the solute molecules. Furthermore, the band intensity gradually decreases with time, implying that the radical pair undergoes geminate recombination. Other results are summarized in Appendix (Figure C1-1 and C1-2).

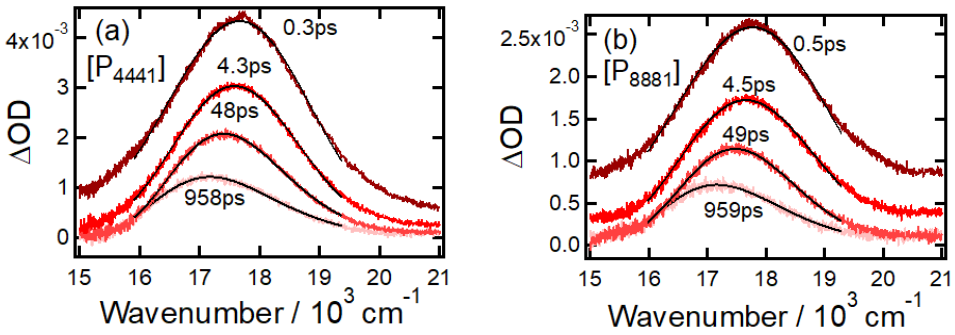

Figure 4-5. Absorption spectrum of PAPT radical generated after the photo-dissociation in (a) $[P_{4441}][NTf_2]$, (b) $[P_{8881}][NTf_2]$.

To extract the time profiles of the peak shift, we fitted the spectrum at each delay time to a log-normal function as follows:

$$\Delta\mathrm{OD}(t,\tilde{\nu}) = h(t) \times \begin{cases} \exp[-\ln(2)\{\ln(1+\alpha(t))/\gamma(t)\}^2 & \alpha(t) \geq -1 \\ 0 & \alpha(t) \leq -1 \end{cases}, \qquad (4.1)$$

where $\alpha(t) = 2\gamma(t)(\tilde{\nu} - \tilde{\nu}_p(t))/\Delta(t)$, $h(t)$ is a scaling factor, $\gamma(t)$ is the asymmetric parameter, $\Delta(t)$ is the bandwidth parameter, and $\tilde{\nu}_p(t)$ is the peak position. In the present case, we assumed that all parameters were time dependent.

As shown in Figure 4-5, the spectral band shape becomes unsymmetrical and broader with time, derived from the conformational change[27] in the geminate radical and interaction with surrounding solvent[49,50], respectively. Especially in the early time, the change in the spectrum shape seems complex, reflecting the competing process of paring conformational change and solvation dynamics. To extract the change in the spectral bandwidth, we conducted a moment analysis and calculated the time evolution of the spectral bandwidth (second moment of the absorption spectrum, $\mu_2(t)^2$) using eq. (4.2):

$$\mu_2(t)^2 = \frac{1}{I(t)} \int_{-\infty}^{\infty} (\tilde{\nu}(t) - \langle\tilde{\nu}\rangle(t))^2 \frac{\Delta\mathrm{OD}(t,\tilde{\nu})}{\tilde{\nu}} d\tilde{\nu}. \quad (4.2)$$

I(t) is the spectrum integral at each delay time:

$$I(t) = \int_{-\infty}^{\infty} \frac{\Delta\mathrm{OD}(t,\tilde{\nu})}{\tilde{\nu}} d\tilde{\nu}, \quad (4.3)$$

where $\langle\tilde{\nu}\rangle(t)$ is the mean (first moment) of the radical absorption at each delay time. Eqs. (4.2) and (4.3) can be solved analytically with the parameters obtained from fitting the transient absorption spectra with the log-normal function (eq. (4.1)). In this chapter, we focus on the peak shift and band-shape variation with time, and the intensity profile, which reflects the recombination dynamics, will be discussed in Chapter 5.

Figure 4-6 shows the time profile of the peak position, $\tilde{\nu}_\mathrm{p}(t)$, extracted from the transient absorption spectra of the PAPT radical in various ILs composed of (a) tetraphosphonium and (b) tetraammonium. In all ILs, $\tilde{\nu}_\mathrm{p}(t)$ gradually shifts ($\Delta\tilde{\nu}_\mathrm{p} \sim 600$ cm^{-1}) to a lower energy with time. At times earlier than ca. 1 ps after photodissociation, $\tilde{\nu}_\mathrm{p}(t)$ increases rapidly. This time window corresponds to the rise time of the concentration of PAPT radicals as shown in Figure C2. Thus, the initial blue shift of the absorption spectrum of PAPT radical is caused by tracing the energy difference along the solvation coordinate and bond dissociation coordinate, as stated in a previous work.[27]

Since a dynamic spectral shift in most cases is caused by solvent reorientation, the time constant for the energy relaxation process generally depends on the solvent viscosity. However, the time profiles in Figures 4-6 seem to be quite similar between various ILs whose viscosity covers a wide range (see Table C3). To obtain the time constants for the peak shifts, we fit the time profiles from ca. 1 ps to a multi-exponential function with three exponents. The fitting results are summarized in Table C3. The fastest time constant at approximately 1 ps and middle constant at several tens of picoseconds did not show any dependence on the cation species, which indicates that the solvent motion corresponding to these time constants is not correlated to the solvent viscosity. The slowest time constant, τ_3 was in the range of several hundred picoseconds. Although

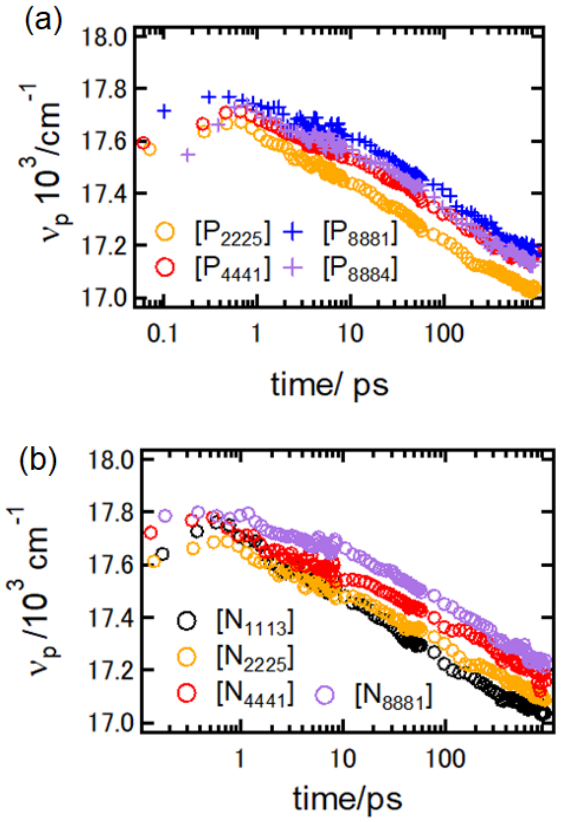

Figure 4-6. Spectrum shift in (a) phosphonium ILs and (b) ammonium ILs extracted from the transient absorption spectrum after the photo-dissociation.

τ_3 seems to reflect the diffusional motion of anions and cations, it is still 10 times faster than the time constant in a previous report on the diffusional motion of ILs.[33] One of the reasons for this is the time window for the transient absorption spectral measurements. The 1 ns range was not sufficient to discuss the nanosecond-scale solvation behavior.

Since the dynamic spectral shift of the photodissociated products is affected by the change in configuration of the geminate pair, the bandwidth of the PAPT radical absorption spectrum is dependent on time. Figure 4-7 shows $\mu_2(\mathrm{t})$ of the PAPT radical in phosphonium (a) and ammonium (b) ILs after photodissociation. While $\mu_2(\mathrm{t})$ decreased until 10 ps after photodissociation, it instead increased from 10 to 1000 ps. Generally, spectral broadening with time reflects the solvation process.[49,50] Since the extent of the broadening (10–1000 ps) was consistent with that observed in 2-propanol as

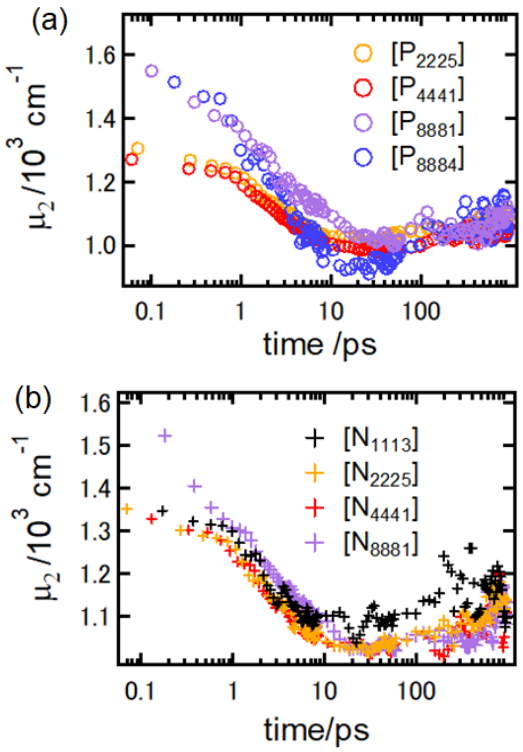

Figure 4-7. Time profile of spectrum bandwidth of PAPT radical after the photo-dissociation in (a) phosphonium ILs and (b) ammonium ILs.

reported by Ernsting et al., the time profile in this region could correspond to the solvation process.[27] On the other hand, spectral narrowing in the case of photodissociated products is assigned to pair conformational dynamics in the initial state of solvation, where the geminate radicals are confined in a solvent cage. In viscous liquids like ILs, this cage effect would be more prominent than in a molecular solvent. Thus, immediately after photodissociation, the configurational change of the radical pair is more dominant than solvent reorientation. As shown in the time profile of the spectral intensity obtained from spectral analysis according to eq. (4.3) (see Figure C2), the spectral intensity dramatically decreased (>50%) in 20 ps. Considering that $\mu_2(\mathrm{t})$ decreased in the first 10–20 ps, the spectral narrowing could be related to the pairing configuration dynamics that lead to recombination. We discuss further details on these recombination dynamics in Chapter 5.

Figure 4-8 shows the time-resolved emission spectra of the PAPT radical in ILs ([P_{2225}][NTf_2] and [P_{8881}][NTf_2]) excited at (a) 10 and (b) 500 ps after photodissociation. The band at approximately 15000–16000 cm^{-1} is emission from the D_2 state of the PAPT radical. In all cases, the band position does not seem to shift to a lower energy with time. The time-resolved spectra in the other ILs ([P_{2225}][NTf_2], [P_{44412}][NTf_2], and [P_{88812}][NTf_2]) excited at 10 and 500 ps are summarized in Appendix C5 (Figures C3 and C4). As is mentioned in the experimental section, the spectra for the radical emission contained the background scattering and fluorescence from the sample cell, and these backgrounds were subtracted from the data of radical emission. Due to the weakness of the radical emission (short lifetime of the radical excited state) and the subtraction procedure of the background signals, the S/N ratio of the radical emission spectrum was worse than that of the transient absorption spectrum. Therefore, we had to make the time-average over ±50ps to obtain the band-shape with reasonable accuracy.

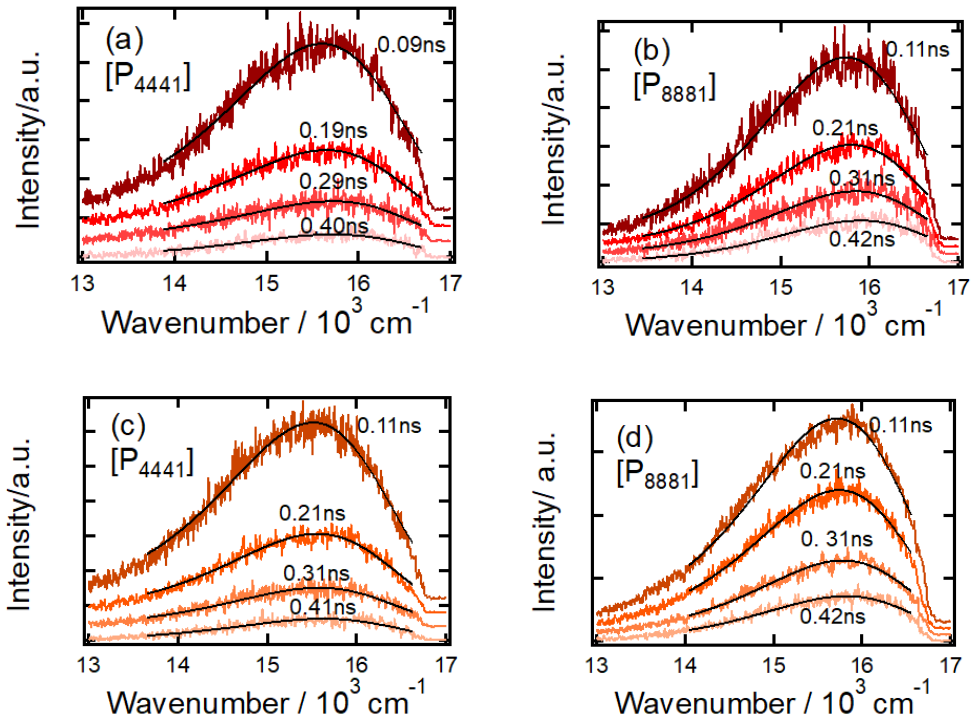

Figure 4-8. Time-resolved emission spectrum of PAPT radical in ILs ($[P_{4441}][NTf_2]$ and $[P_{8881}][NTf_2]$) excited at 10 ps ((a) and (b)) and at 500 ps ((c) and (d)) Each spectrum is the average of the spectrum at the indicated time ±0.05 ns.

To further analyze the spectral dynamics in the excited state, we fit the spectra at each time to a log-normal function (eq (4.1)) and extracted the time profile of the peak position. In the fitting, at first, we fit the spectrum at different delay time with all parameters (h, $\tilde{\nu}_p$, Δ, and γ) in eq (4.1). Then, we calculated the averaged value of the spectral band width (Δ) and re-fit the spectrum with fixing the parameter of Δ. Although the spectral band shape of the absorption changes dramatically within 10ps, it hardly matters in the present case since we took the time average of the spectrum. By fixing the band-width parameter, the peak position could be determined by a reasonable accuracy. Although the standard deviation depended on time and became large at the long delay time, the deviation was enough small to discuss the time profile the emission peak in comparison with the absorption peak shift in the initial 300ps (averaged accuracy over

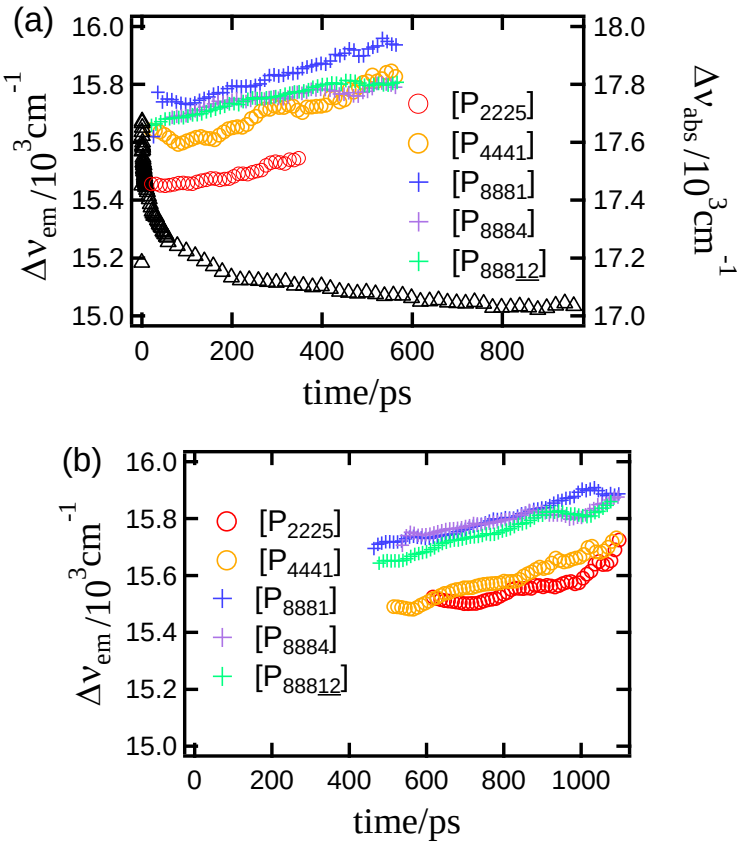

Figure 4-9. Time profile of the peak position in various ILs extracted from the time-resolved emission spectrum excited at 10 ps (a) and 500 ps (b) after the photo-dissociation. The open triangle represents the spectrum shift in the ground states of PAPT radical. In $[P_{2225}][NTf_2]$ excited at 10ps, profile in the long time region is not shown because of the worse S/N ratio.

the experimental time window was typically ±60 cm^{-1}).

Figure 4-9 shows the time profiles of the peak positions for excitation at (a) 10 and (b) 500 ps after photodissociation. Compared with the shift in the transient absorption spectra represented by open triangles, the emission band position in each IL shows clear difference; it does not shift to a lower energy with time, i.e., no energy relaxation process was observed in the D_2 state. In fact, the emission peak seems to shift to an even higher energy with time. The initial peak position of the fluorescence was slightly dependent on the delay time. With increasing the delay time, the peak position showed a slight red shift (except for $[P_{2225}][NTf_2]$) as expected from the absorption shift, but the extent of the shift

was quite small in comparison with the absorption shift. This point will be discussed in the following again.

The difference in the spectral dynamics of the PAPT radical between the ground and excited states is striking and may represent new insight into the photophysical processes of the molecule because within the linear response regime, the absorption and emission spectra should trace the same relaxation process. Below, we summarize our findings from the spectroscopic measurements and what differed from previous reports on solvation dynamics and photophysical processes.

1. The time profile of the absorption spectral shift after photodissociation showed red-shift by solvent reorganizing process. The time-profile in ILs composed of various cation species were quite similar, suggesting that solvation dynamics of ILs after the photodissociation is independent of the solvent viscosity.
2. When the photodissociated product was excited to the electronically excited state, no energy relaxation process was observed, indicating that solvation dynamics might not occur.

To elucidate these experimental results, we discuss the results obtained from MD simulations in the next section.

4.3.2. Non-Equilibrium Molecular Dynamics Simulation

We first demonstrate how the choice of functional set for DFT calculations affects the electronic states of the PAPT radical. We calculated the transition energy (UV-Vis spectra) of the PAPT radical in several solvents (PCM, polarizable continuum model) at the levels of U-B3LYP/6-31G+(d, p) and U-camB3LYP/6-31G+(d, p). Table C4 lists the calculated transition energies in several solvents from the D_0 to the D_2 state ($\tilde{\nu}_{\mathrm{PCM}}/\mathrm{cm}^{-1}$), which correspond to the experimentally observed transition, together with the

solvatochromic shift from the peak position in cyclohexane ($\Delta\tilde{\nu} = \tilde{\nu}_{\mathrm{CHX}} - \tilde{\nu}_{\mathrm{PCM}}$). U-camB3LYP gives a larger solvatochromic shift than U-B3LYP. In Figure C5, the absorption transition energies obtained from DFT calculations ($\tilde{\nu}_{\mathrm{PCM}}$) are plotted against the orientation polarizability of the solvent ($\Delta f = (\varepsilon - 1)/(2\varepsilon + 1) - (n - 1)/(2n + 1)$, ε: dielectric constant n: reflactive index). Experimental results from a previous report by Ito and Matsuda[52] are also shown for comparison. Since the line slope of the plot calculated by U-B3LYP is similar to that in the experimental report, we adopted unrestricted-B3LYP as the functional set. For the MD calculations, we used structural parameters and electro static potential (ESP) charges obtained in vacuum because no PCM is available for IL solvents and it is difficult to separate the effect of solvent polarization from the MD potential.

Figure 4-10 shows the time profiles of the sum of the solute–solvent ([P_{4441}][NTf_2]) interaction energies after bond dissociation simulated at the ground-state potential of the PAPT radical (D_0^{eq}) (E_{GS}, red line) and the Franck–Condon (FC) excited-state potential (D_2^{noneq}) ($E_{ES\text{-}FC}$, black line) obtained by MD simulations. The interaction energy becomes more negative in the several picoseconds after dissociation. Since the

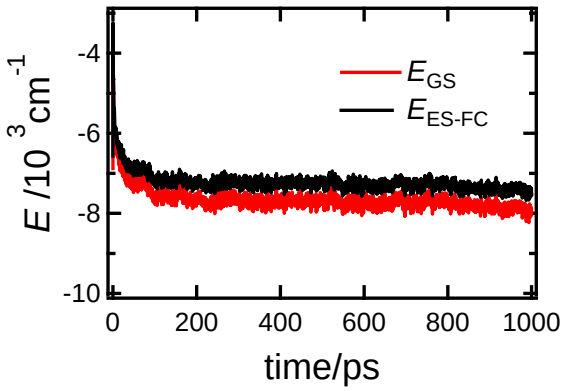

Figure 4-10. Time profile of the PAPT radical-solvent ILs interaction energy after the photo-dissociation in the ground state (black) and FC excited state (red) in [P_{4441}][NTF_2].

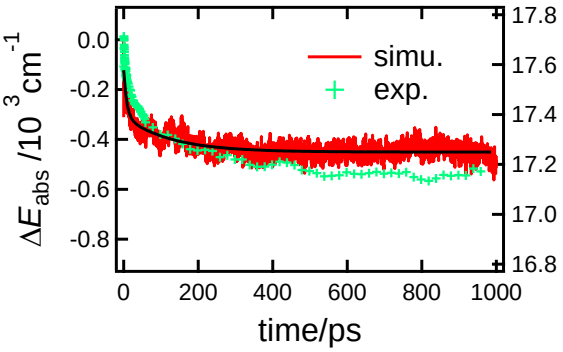

Figure 4-11. Time profile of the transition energy of absorption in $[P_{4441}][NTf_2]$ obtained from MD simulation together with the experimental obtained spectrum shift (green markers in the inset graph). Black line represents functional fit to the simulation results by tri-exponential function.

photodissociation process is accompanied by a significant change in the dipole moment orientation and molecular volume, these energy changes in the short time region could be caused by a change in distance between the interaction sites of the PAPT radical and solvent ILs that diffuse toward the solute after photodissociation. Figure 4-11 shows the time profiles of the transition energies corresponding to absorption (ΔE_{abs}) calculated by subtracting E_{GS} from $E_{\mathrm{ES\text{-}FC}}$. In the case of the absorption transition energy, we found the simulations reproduced the experimental results, as plotted together in the figure (green line). The energy difference from the simulations ($\Delta E = E(0) - E(\infty)$) for $[P_{4441}][NTf_2]$ is approximately 6.0 kJ mol^{-1}, which almost corresponds to the experimental spectral shift, $\Delta\tilde{\nu}$: 600 cm^{-1}($= \tilde{\nu}(0) - \tilde{\nu}(\infty)$) (7.2 kJ mol^{-1}). The decay time constants obtained from the simulation also capture the trend of the experimental results. ΔE_{abs} from the simulations was found to decay exponentially with three time-constants of 0.7, 11.1, and 129 ps. We obtained similar time constants experimentally for the absorption peak shifts for the faster two components (τ_1 and τ_2 in Table C3).

The solvation process is related to the difference in the local solvation environment

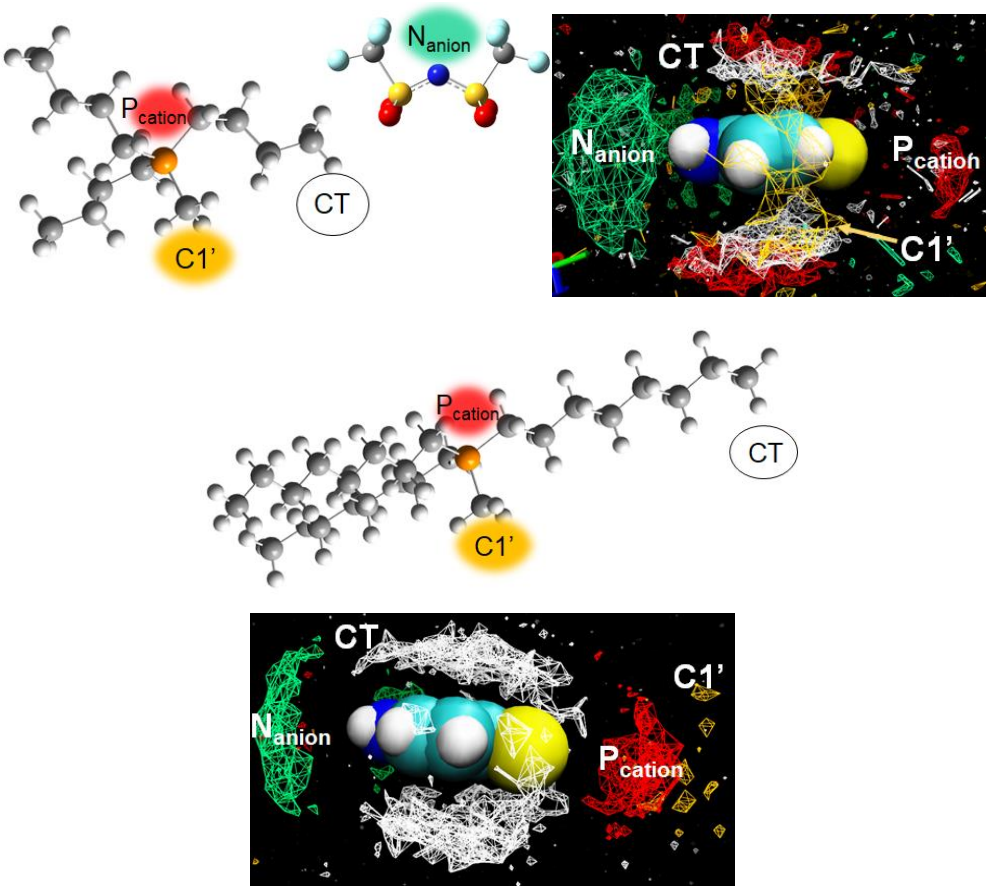

Figure 4-12. Spatial distribution function of $[P_{4441}][NTf_2]$ and $[P_{8881}][NTf_2]$ around PAPT radical by averaging 30 ns trajectrory.

of ILs around BPADS and PAPT radical. In this paragraph, we show spatial distribution function (SDF) of ILs and discuss the origin of energy relaxation process after the photodissociation and the reason why that process did not show viscosity independent within the experimental time window. Figure 4-12 shows the SDFs of selected atomic species of $[P_{4441}][NTF_2]$ and $[P_{8881}][NTf_2]$ around a PAPT radical. The SDFs were obtained from a long run (30 ns) after photodissociation and thus reflect the equilibrated structure. For the atomic species of the solvent ILs, we selected the charged head groups of the cation (P_{cation}, red) and anion (N_{anion}, green), the terminal carbon in the alkyl chain (CT, white), and the methyl carbon in the cation (C1', yellow). For example, in

[P_{4441}][NTf_2], N_{anion} is located in the vicinity of the amino group of the PAPT radical to form hydrogen bonding, which determines the P_{cation} and CT positions. The same is true for the solvation environment of BPADS as shown in Figure C6. The differences in the solvation structure for BPADS and the PAPT radical is probability density of P_{cation}, that is estimated by the radial distribution function around S atom ($g_s(r)$) of solutes as shown in the Figures C7. After the photodissociation, S atom is more strongly solvated by the P_{cation}, which results in the stabilization of PAPT radicals and the red-shift in the transient absorption spectrum. Since the solvation structures around the NH_2 group and phenyl group before and after the dissociation do not change so much, the movement of the cation around the S atom may not be hindered by other species. The initial solvation process is considered not to require significant movement of the cations and anions. Additionally, that solvation structure is quite similar for two IL composed of different cation species; N_{anion} sticks to amino group of the solute molecule, and CT holds the phenyl ring. Thus, the solvation dynamics may be independent of cations with different alkyl chain lengths and the solvent viscosity.

Next, we discuss the spectrum shift in the excited states of photo-dissociated product. Figure 4-13 shows the time profile of the interaction energy in [P_{4441}][NTf_2] extracted from the trajectory simulated for the D_2 state of a PAPT radical (D_2^{eq}), which was switched from the ground state at (a) 1000 and (b) 10 ps after bond dissociation. E_{ES} (yellow curve) is the sum of the solute–solvent interaction energy extracted from the excited-state trajectory, and $E_{GS\text{-}FC}$ (blue line) is the same sum calculated from the FC ground-state (D_0^{noneq}) trajectory. Comparing these profiles with those in Figure 4-10, neither E_{ES} nor $E_{GS\text{-}FC}$ is strongly dependent on time, but the profile is dependent on the time delay of photoexcitation, on the contrary to the experimental results. As shown in Figure 4-13 (a)

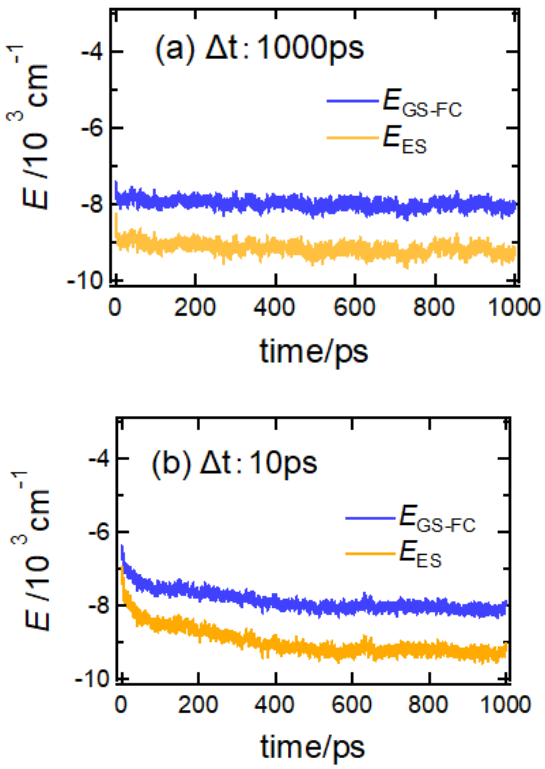

Figure 4-13. Time profile of the sum of the interaction energy between PAPT radical in D_2 state (D_2^{eq}) and Frank-Condon D_0 state (D_0^{noneq}) with solvent IL [P_{4441}][NTf_2], excited at (a) 1000ps and (b) 10ps after bond-dissociation.

and (b), the solute–solvent interaction energy $E(t)$ for excitation 10 ps after bond dissociation shows a decay, while that obtained at a 1000 ps delay does not show any meaningful dependence on time. The above difference might be attributable to the dynamics of the geminate radical pair upon the relaxation process specific to the photodissociated products. Figure C8 shows the time profile of the pair distance of the PAPT radicals (distance between sulfur atoms and between center of mass of radicals) in [P_{4441}][NTf_2] after bond dissociation. In both solvent ILs, the pair distance significantly increases in the initial 100 ps after bond dissociation. This result combined with the experimentally obtained time profile of $\mu_2(t)$ (Figure 4-7) gives information about the

dynamics of the geminate radicals: after photodissociation, the geminate radicals confined in the solvent cage initially diffuse out of the cage and are separately solvated by the surrounding solvent ions. Since the radicals do not completely escape the cage within 10 ps, the local environment that the PAPT radical experiences at 10 ps after photodissociation should be quite different from that at 1000 ps, where the radical pairs are sufficiently separate. At 10 ps after bond dissociation, the solvent ILs are still reorienting to solvate the PAPT radicals. When a PAPT radical is photoexcited at this time, the remainder of the solvation process should occur in the excited state, which is origin of the decay in $E(t)$ in the early period after photodissociation (Figure 4-13 (b)). On the other hand, at 1000 ps after bond dissociation, solvation of the PAPT radical is almost complete. The energy relaxation triggered by photoexcitation at this time is due to the solvent response to the electronic redistribution of the PAPT radical. The perturbation caused by photoexcitation of the PAPT radical is insufficient to force the surrounding solvent to reorient, probably because the change in the magnitude of the dipole moment is small and the orientation of the dipole moment is almost the same as that in the ground state. This is the reason why the time profile of the interaction energy rapidly approaches $E(\infty)$.

Figure 4-14 shows the time profiles of the transition energies corresponding to emission (ΔE_{em}) calculated by subtracting E_{ES} from $E_{\mathrm{GS\text{-}FC}}$. First, for both excitation timings (10 and 1000 ps after bond dissociation), as shown in Figure 4-14, $\Delta E_{\mathrm{em}}(t)$ shifts to a lower energy with time, which means that energy relaxation occurs in the excited state. It is apparent that $\Delta E_{\mathrm{em}}(t)$ excited at 10 ps shows a slow decay, while $\Delta E_{\mathrm{em}}(t)$ excited at 1000 ps does not show a significant decay component. This can be

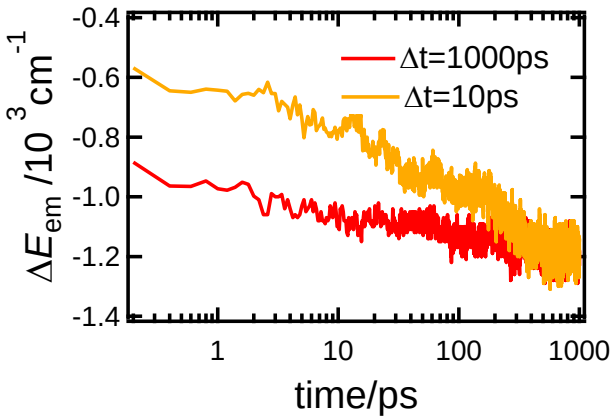

Figure 4-14. Time profile of the transition energy of emission, excited at 10 ps (yellow line) and 1000ps (red line) in $[P_{4441}][NTf_2]$.

explained as discussed above: the remaining solvent relaxation process that was not completed within 10 ps in the ground state occurs in the electronic excited state when the PAPT radical is excited at 10 ps.

Comparison of the time-averaged spectra at different excitation timings may give insight into the discrepancy between the experiments and simulations. Figure C9 shows the time-averaged emission spectra of the PAPT radical in $[P_{2225}][NTf_2]$ excited at 10 and 500 ps after photodissociation. The spectra were reconstructed from the fitting parameters of the log-normal function (eq. (4.1)) simulating the time-resolved emission spectra. The emission peak shifts by approximately 100 cm^{-1} to a lower energy with increased excitation time (10 $\rightarrow$ 500 ps). This means that an energy relaxation process does occur along the solvation coordinate in the excited state, although the emission peak in Figure 7 does not show a red-shift. As shown in Figure 4-6, the transient absorption peak position red-shifts by 360 cm^{-1} from 10 to 500 ps. Even if we took the time average as we did for the emission spectra (100 ps averaged), this peak position difference is still 2.5 times larger than that of the emission spectra (100 cm^{-1}). A similar trend was observed in the other ILs. This difference between the absorption and emission energy transitions with

time cannot be explained by the potential energy surface of the photophysical relaxation process considered here. There might be another relaxation path in the excited state caused by the pairing conformation, where one of radicals affect the electronic state of the other, especially when the PAPT radical is excited at an early time after photodissociation. Unfortunately, this effect was not captured in this work, since the pairing configuration change is fast and completed in ~10 ps, as shown in Figure 4-7, whereas the time resolution of our system for time-resolved emission measurements is limited to ca. 20 ps. To further investigate the effect of the initial pairing configuration change on the spectral shift and clarify the unique spectral shift in the excited state, we will need to acquire several-picosecond-resolved emission spectra.

4.4. Conclusions

In this chapter, we investigated the solvation dynamics of the PAPT radical in both the ground state and electronically excited state triggered by the photodissociation of BPADS. Transient absorption and time-resolved emission spectra of the PAPT radical in various ILs were measured after photodissociation. The time profile of the peak position extracted from the transient absorption spectra showed a red-shift, indicating that the solvent molecules reorient to stabilize the photodissociated compounds. We also found that the time constants for the peak shifts in the different ILs were independent of the cation species, i.e., the solvent viscosity. From the emission measurements, on the other hand, the band position in the time-resolved emission spectra did not shift to a lower energy, which means that solvation dynamics might not occur. Non-equilibrium MD simulations reproduced the experimentally observed spectral shift in the transient absorption spectra, with good agreement between both the extent of the spectral shift and the time constants. Based on our investigation of the solvation structure, the spectral shift is caused by the reformation of solute–solvent IL interactions induced by the changes in the dipole moment orientation and molecular volume caused by photodissociation. The investigation also reveals that solvation structure of two different ILs provide quite similar environment for both BPADS and the PAPT radical. This is the reason why absorption spectrum shift is independent of solvent viscosity. On the other hand, the simulated emission spectral shift did not completely capture the experimental observations. There are several possible explanations for this. First, the computational method we applied in this study is preliminary one. The potential set of the geminate PAPT radicals still could be sophisticated to include intermolecular potential between them. Further examination of the non-equilibrium MD simulation may provide us insight

into molecular dynamics occurring immediately after the photodissociation. Second, from experimental side, molecular dynamics at early stage of solvation might be missed in our present experimental setup. Configuration dynamics of the geminate PAPT radicals occurred in 10ps after the photodissociation should be important to reveal the solvation dynamics afterward. We consider that the unique solvation dynamics observed in our study might be specific to the photodissociated product. For further research, from the experimental side, we plan to use other molecules that undergo photodissociation and emissive. Although detail is not included in this section, we found unique recombination dynamics of geminate radicals in ILs: the recombination yield and kinetics didn't show dependence on the solvent viscosity. The details of the recombination dynamics of the PAPT radicals together with some mathematical models to explain the unique molecular dynamics in ILs will be given in the subsequent section.

Appendix C

Table of contents

C1. Experimental Details; Synthesis of Ionic Liquids

C1. 1. Materials

Triethylammine (>98%), dichloromethane (99.5%>), hexane (96.0%>) and sodium hydrocarbonate (99.6%>) were purchased from Nacalai Tesque. Tributhylammine (>99%) was purchased from EMD Millipore Coorporation. Triocthylammine (>97%), 1-bromopentane (>97%), Iodomethane (>95%) were purchased from FUJIFILM Wako Pure Chemical Corporation. Sodium tetrafluoroborate (98%>) and potassium hexafluorophosphate (99.44%>) were purchased from Stella Chemifa. Lithium bis(trifluoromethanesulfonyl)imide (Li[NTf_2]) was purchased from Kanto Kagaku. All these chemicals except triethylammine were used without further purification.

C1. 2. Synthesis of [N_{2225}][NTf_2]

1-bromopentane (100.1 g, 0.66 mol) was slowly added to 1.03 equivalent triethylamine (68.7 g, 0.68 mol) dissolved in 150 mL of ethanol under N_2 atmosphere. The reaction mixture was stirred at 80 ℃. [N_{2225}]Br was obtained by evaporating the solvent at 60 ℃. The product was purified by recrystallization in methanol at –40℃. [N_{2225}]Br (13.3 g, 0.04 mol) was dissolved into dichloromethane (40 mL) and 1.5 equivalent lithium bis(trifluoromethanesulfonyl)imide (18.8 g, 0.07 mol) was added to the solution. The mixture was stirred vigorously, and dichloromethane layer was washed with distilled water for three times. To enhance the reaction yield, the resulted solution was again mixed with aqueous solution (30 mL) of lithium bis(trifluoromethanesulfonyl)imide (9.6g, 0.03mol). The dichloromethane solution was washed with distilled water for three times. Finally, [N_{2225}][NTf_2] was obtained as transparent liquid after the evaporation of the solvent at 60 ℃. The purity of the product

was confirmed by ^{13}C and ^{19}F NMR. The amount of bromide in the solution was confirmed by Mohr titration in methanol. Purity of anion was 99.8 %.

^{13}C {^{1}H} NMR (75 MHz, $CDCl_3$, TMS): δ= 120 .0(q, C_F; $[N(SOCF_3)_2]^-$), 57.2(s, 1C), 52.9(s, 6C), 28.2(s, 2C), 22.1(s, 3C), 21.3(s,4C), 13.7(s,5C), 7.24(s, 7C)

C1. 2. Synthesis of $[N_{4441}][NTf_2]$

1.2 equivalent molar iodomethane (46 g, 0.32 mol) was slowly added to tributylammine (50 g, 0.27 mol) dissolved in 200 mL of hexane at 0 ℃ under N_2 atmosphere. The mixture was stirred overnight at room temperature. The resulted solution was used for the next reaction without further purification. 1.2 equivalent potassium hexafluorophposphate (59.6 g, 0.32 mol) and sodium hydrogen carbonate (2.5 g, 0.02 mol) were dissolved in distilled water (500 mL). $[N_{4441}]$I/hexane solution and 1,2-dicholoethane (180 mL) was added to this solution and stirred vigorously. The organic layer was extracted and washed with distilled water over three times until yellowish color of the organic solution disappeared. $[N_{4441}][PF_6]$ was obtained by evaporating the solvent at 60℃. The product was purified by recrystallization in dichloromethane at −40 ℃ for three times.

1.2 equivalent molar lithium bis(trifluoromethanesulfonyl)imide (50.9 g, 0.18 mol) in distilled water(200 mL) was added to the $[N_{4441}][PF_6]$ (55.4g, 0.15 mol) /dichloromethane solution (200 mL). The mixture was stirred vigorously, and dichloromethane layer was washed with distilled water for three times. To improve the yield of anion exchange, the solution was again mixed with the aqueous solution (150 mL) of 0.6 equivalent molar lithium bis(trifluoromethanesulfonyl)imide (24.5 g, 0.09 mol) and stirred vigorously. The dichloromethane layer was extracted and washed with

distilled water for three times. $[N_{4441}][NTf_2]$ was obtained as transparent liquid by evaporating the solvent at 60 ℃. The purity of the product was confirmed ^{13}C and ^{19}F NMR.

^{13}C $\{^1H\}$ NMR (75 MHz, $CDCl_3$, TMS): δ= 119.9(q, C_F; $[N(SOCF_3)_2]^-$), 61.7(s, 1C), 48.4(s,5C), 24.1(s, 2C), 19.5(s, 3C), 13.4(s, 4C)

C1. 3. Synthesis of $[N_{8881}][NTf_2]$

1.2 equivalent molar iodomethane (32.6 g, 0.22 mol) was added to trioctylammine (70 g, 0.20 mol) dissolved in 200 mL of hexane at 0 ℃ under N_2 atmosphere. The reaction mixture was stirred at room temperature overnight. $[N_{8881}]I$ was obtained by evaporating hexane, and was used for the next reaction without further purification. $[N_{8881}]I$ was dissolved in 500 mL of dichloromethane and mixed with 700 mL of aqueous solution of potassium hexafluorophposphate (43.7 g, 0.24 mol) and sodium hydrogen carbonate (1.8 g, 0.02 mol). The mixture was stirred vigorously, and dichloromethane solution was washed with distilled water for three times. By evaporating solvent at 60 ℃, $[N_{8881}][PF_6]$ was obtained. The product was purified by recrystallization in saturated solution of dichloromethane at 60℃.

1.2 equivalent molar lithium bis(trifluoromethanesulfonyl)imide (26.8 g, 0.09 mol) in distilled water (100 mL) was added to the dichloromethane solution (100 mL) of $[N_{8881}][PF_6]$ $[N_{8881}][PF_6]$ (40 g, 0.08 mol). The mixture was stirred vigorously, and dichloromethane layer was washed with distilled water for three times. $[N_{8881}][NTf_2]$ was obtained by evaporating the solvent at 60℃. The purity of the product was confirmed by ^{13}C and ^{19}F NMR.

^{13}C {^{1}H} NMR (75 MHz, $CDCl_3$, TMS): δ= 119.9(q, C_F; $[N(SOCF_3)_2]^-$), 61.9(s, 1C), 48.4(s, 9C), 31.7(s, 2C), 29.0$_3$(s, 3C), 29.0$_2$(s, 4C), 26.1(s, 5C), 22.6(s, 6C), 22.3(s, 7C), 14.1(s, 8C)

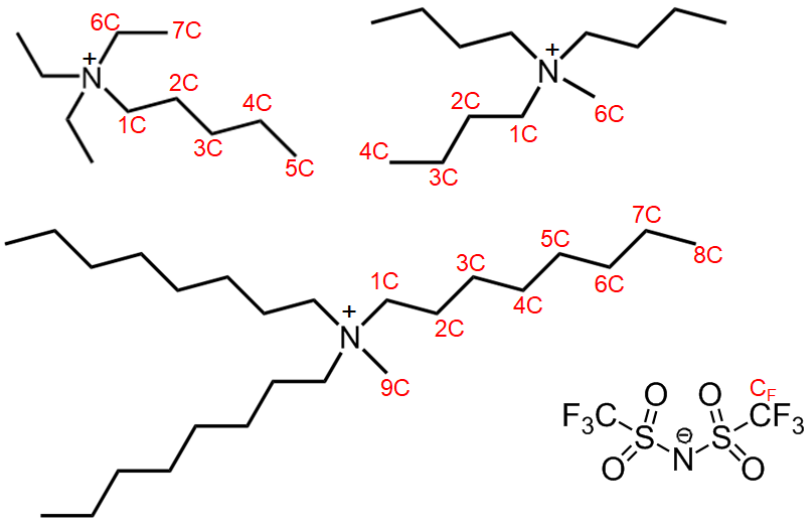

C2. Computational Details; Optimized Parameters Obtained from DFT Calculation and MD Simulation

C2. 1. Optimized Structure and ESP (electro static potential) Charges on Each Atom

Table C2-1(a). Optimized structure of bis-(*p*-aminophenyl)disulfide and ESP charge on each atom calculated by B3LYP/6-31G+(d,p). The values in parenthesis in ESP charge denote the corrected values to achieve molecular symmetry of each phenyl ring and total zero charge.

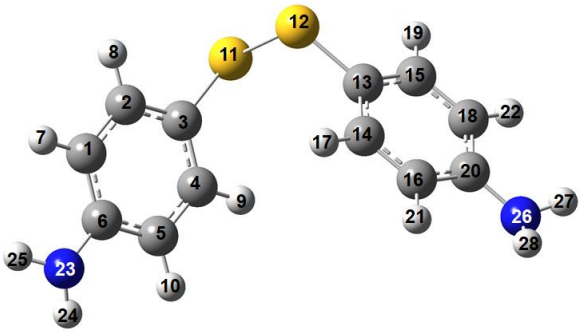

		x	y	z	ESP charge
1	C	3.912	0.019	0.610	−0.09 (−0.06)
2	C	2.974	−0.978	0.366	−0.41
3	C	1.861	−0.734	−0.456	0.59
4	C	1.719	0.538	−1.033	−0.40 (−0.41)
5	C	2.659	1.538	−0.797	−0.04 (−0.06)
6	C	3.771	1.294	0.029	0.21
7	H	4.765	−0.187	1.252	0.14 (0.12)
8	H	3.101	−1.958	0.815	0.10_9 (0.11)
9	H	0.867	0.741	−1.674	0.11_4 (0.11)
10	H	2.531	2.518	−1.252	0.10 (0.12)
11	S	0.685	−2.026	−0.820	−0.23
12	S	−0.685	−2.026	0.820	−0.23
13	C	−1.861	−0.734	0.456	0.59
14	C	−1.719	0.538	1.033	−0.40
15	C	−2.974	−0.978	−0.366	−0.41
16	C	−2.659	1.538	0.797	−0.04 (−0.06)
17	H	−0.867	0.741	1.674	0.11_4 (0.11)

18	C	−3.912	0.019	−0.610	−0.09 (−0.06)
19	H	−3.101	−1.958	−0.815	0.10_8 (0.11)
20	C	−3.771	1.294	−0.029	0.21
21	H	−2.531	2.518	1.252	0.10 (0.12)
22	H	−4.765	−0.187	−1.252	0.14 (0.12)
23	N	4.685	2.307	0.310	−0.59
24	H	5.596	2.016	0.636	0.25
25	H	4.726	3.074	−0.346	0.25
26	N	−4.685	2.307	−0.310	−0.59
27	H	−5.596	2.016	−0.636	0.25
28	H	−4.726	3.074	0.346	0.25

Table C2-1(b). Optimized structure of *p*-aminophenylthiyl radical and ESP charge on each atom calculated by unrestricted B3LYP/6-31G+(d,p). The value in parenthesis in ESP charge denotes the corrected value for the total charge to be zero which is used for the simulation.

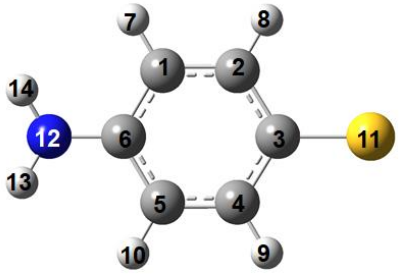

		x	y	z	ESP charge
1	C	−1.068	−1.218	−0.004	−0.22
2	C	0.313	−1.215	−0.002	−0.19
3	C	1.059	0	−0.001	0.39
4	C	0.313	1.215	−0.002	−0.19
5	C	−1.069	1.218	−0.004	−0.22
6	C	−1.789	0	−0.003	0.44
7	H	−1.612	−2.16	−0.008	0.14
8	H	0.858	−2.153	−0.001	0.08
9	H	0.858	2.153	−0.001	0.08
10	H	−1.612	2.16	−0.008	0.14
11	S	2.777	0	0.004	−0.33 (−0.34)
12	N	−3.163	0	−0.036	−0.75
13	H	−3.664	−0.855	0.148	0.32
14	H	−3.664	0.855	0.149	0.32

Table C2-1(c). Optimized structure of *p*-aminophenylthyil radical and ESP charges on each atom calculated by TDDFT unrestricted-B3LYP/6-31G+(d,p). The value in parenthesis in ESP charge denotes the corrected value for the total charge to be zero which is used for the simulation.

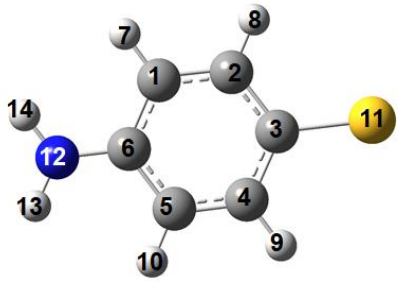

		x	y	z	ESP charge
1	C	−1.093	−1.222	0	−0.13
2	C	0.298	−1.212	0	−0.23
3	C	1.026	0	0	0.43
4	C	0.298	1.212	0	−0.23
5	C	−1.093	1.222	0	−0.23
6	C	−1.813	0	0	0.35
7	H	−1.633	−2.166	0	0.13
8	H	0.844	−2.149	0	0.07
9	H	0.844	2.149	0	0.07
10	H	−1.633	2.166	0	0.13
11	S	2.85	0	0	−0.44 (−0.46)
12	N	−3.191	0	0	−0.68
13	H	−3.714	−0.863	0	0.34
14	H	−3.714	0.863	0	0.34

C2.2. Preparation of the Initial Configuration of MD Simulation

We first set up a cubic simulation box with one solute molecule (BPADS) dissolved in ILs (500 cations and 500 anions). The box size was optimized to yield a reasonable density in the references for each solvent at 300 K. First, we conducted the energy minimization process equipped to GROMACS (steepest descent) for initially prepared simulation box. After maximum force on atom was smaller than the threshold, annealing procedure was applied; the temperature was set to 800 K and gradually decreased to 300 K for 500 ps. Using the resulted gro. file, we next conducted 1 ns run in the NPT ensemble to confirm density of the system optimized simulation box size, we also performed long simulation run to calculate mean square displacement of cation and anion to get self-diffusion coefficient. From 30 ns long run, we got self-diffusion coefficient of P_{4441} cation, P_{8881} cation and NTf_2 anion in each ILs. The optimized box size and physicochemical parameters (density and self-diffusion coefficient) together with some experimental values are summarized in Table C3-2.

Table C2-2. Optimized box size of the system, density and self-diffusion coefficient obtained from the MD simulation in ILs.

Solvent ILs	Box size /nm	Density /g cm^{-3}		Self-diffusion coefficient D 10^{-8}/cm^2 s^{-1}	
		simulation	Ref.	cation	anion
$[P_{4441}][NTf_2]$	6.90×6.90× 6.90	1.19	1.28[53] (298K)	8.04 (5.48[55])	5.59 (6.93[55])
$[P_{8881}][NTf_2]$	7.96×7.96×7.96	1.05	1.09[54] (298.15K)	12.3	7.20

C3. Time Constants of Spectrum Shift in Various ILs

Time-profiles of spectrum shift in various ILs were fit to tri-exponential function as follows;

$$\tilde{\nu}_{\mathrm{p}}(t) = \tilde{\nu}_{\infty} + A_1 \exp(-t/\tau_1) + A_2 \exp(-t/\tau_2) + A_3 \exp(-t/\tau_3)$$

$\tilde{\nu}_{\infty}$ is peak position at t→ ∞. Obtained parameters are summarized in the table below.

Table C3. Viscosity of ILs and time constants and amplitudes of absorption spectrum shift in various ILs.

cation species	η/mPas (295 K)	τ_1/ps	τ_2/ps	τ_3/ps	A_1	A_2	A_3	ν_{∞}
$[N_{1113}]$	89.8	1.2	23.2	227	1	1.44	1.56	17.1
$[P_{2225}]$	103.3	1.5	30.7	328	1	1.67	1.67	17.0
$[N_{2225}]$	206.4	1.6	35.2	396	1	2.09	2.36	17.1
$[P_{4441}]$	253.0	1.6	25.7	212	1	1.55	2.54	17.2
$[P_{8884}]$	412.7	1.3	39.6	289	1	1.91	2.64	17.1
$[P_{8881}]$	422.5	1.2	27.5	257	1	1.88	3.33	17.2
$[N_{4441}]$	663.8	1.0	27.5	433	1	1.39	2.10	17.1
$[N_{8881}]$	721.6	1.4	31.7	351	1	2.13	3.49	17.2

C4. Results of DFT Calculation at the Level of Unrestricted-B3LYP and Unrestricted-camB3LYP

Table C4. Dipole moment (μ), UV-Vis specrtrum ($\tilde{\nu}_{\mathrm{PCM}}$) and solvatochromic shift ($\Delta\tilde{\nu}$) of *p*-aminophenylthyil radical.

		unrestricted-B3LYP			unrestricted-camB3LYP		
Electronic state	Solvent (PCM model)	μ /D	$\tilde{\nu}_{\mathrm{PCM}}$ 10^3 cm^{-1}	$\Delta\tilde{\nu}$ /10^3cm^{-1}	μ /D	$\tilde{\nu}_{\mathrm{PCM}}$ /10^3cm^{-1}	$\Delta\tilde{\nu}$ /10^3cm^{-1}
D_0	None(vacuum)	6.52	20.49	-	6.07	22.06	-
D_2		9.94	18.65	-	10.98	20.33	
D_0	CHX	8.01	19.28	0	7.46	20.47	
D_2		12.1	16.97	-	14.32	18.25	
D_0	THF	10.1	18.67	0.61	9.35	19.37	1.10
D_2		14.7	15.97	-	19.36	16.39	
D_0	Acetone	10.7	18.55	0.73	10.02	19.09	1.38
D_2		15.9	15.75	-	21.52	15.69	
D_0	Methanol	10.9	18.57	0.71	10.19	19.07	1.40
D_2		15.8	15.74	-	22.09	15.56	
D_0	Acetonitrile	10.2	18.53	0.75	10.21	19.03	1.44
D_2		15.8	15.69	-	22.17	15.49	
D_0	DMSO	11	18.41	0.87	10.28	18.87	1.60
D_2		15.9	15.53	-	22.39	15.24	

C5. Supplementary Figures

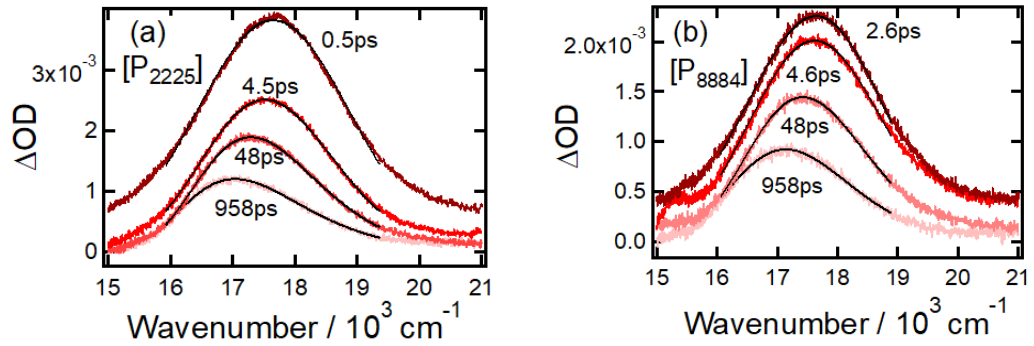

Figure C1-1. Transient absorption spectrum after the photodissicaion in (a) $[P_{2225}][NTf_2]$ and (b) $[P_{8884}][NTf_2]$.

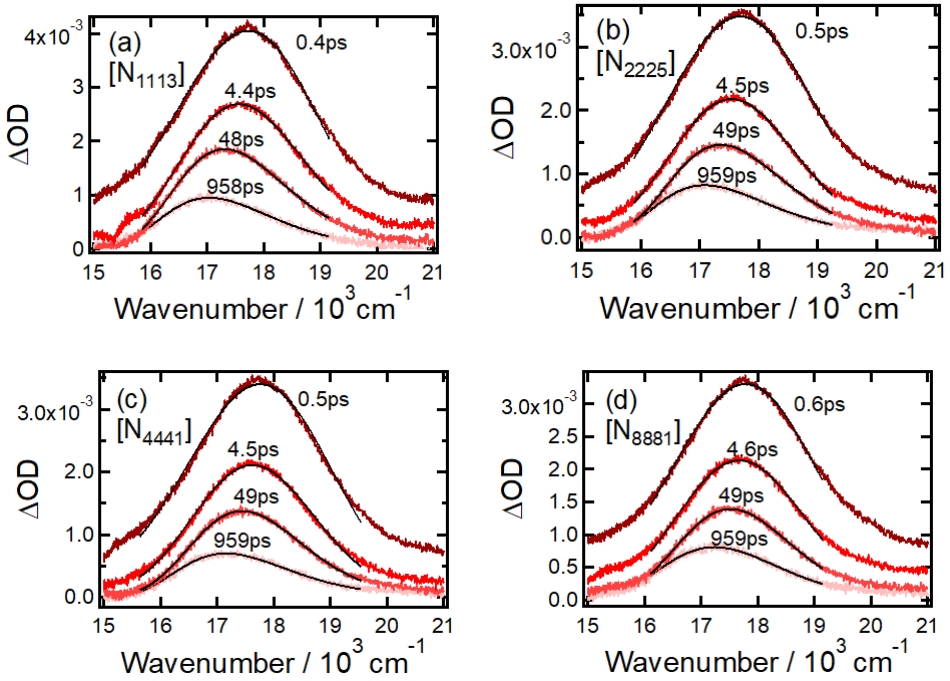

Figure C1-2. Transient absorption spectrum after the photodissicaion in ammonium ILs ((a) $[N_{1113}][NTf_2]$, (b) $[N_{2225}][NTf_2]$, (c) $[N_{4441}][NTf_2]$ and (d) $[N_{8881}][NTf_2]$).

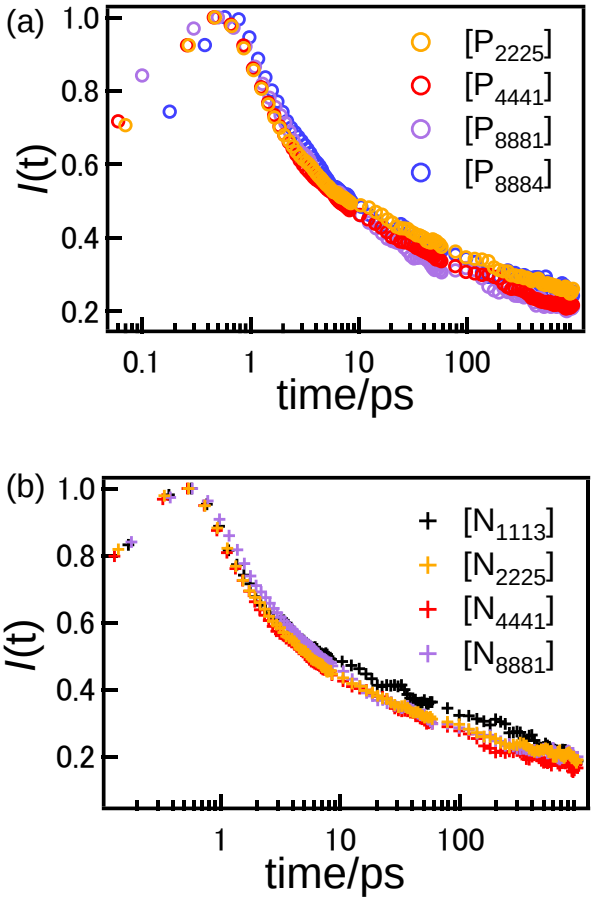

Figure C2. Time profile of spectrum integral of the PAPT radical after the photo-dissociaotin in various (a) phosphonium ILs and (b) ammnonium ILs.

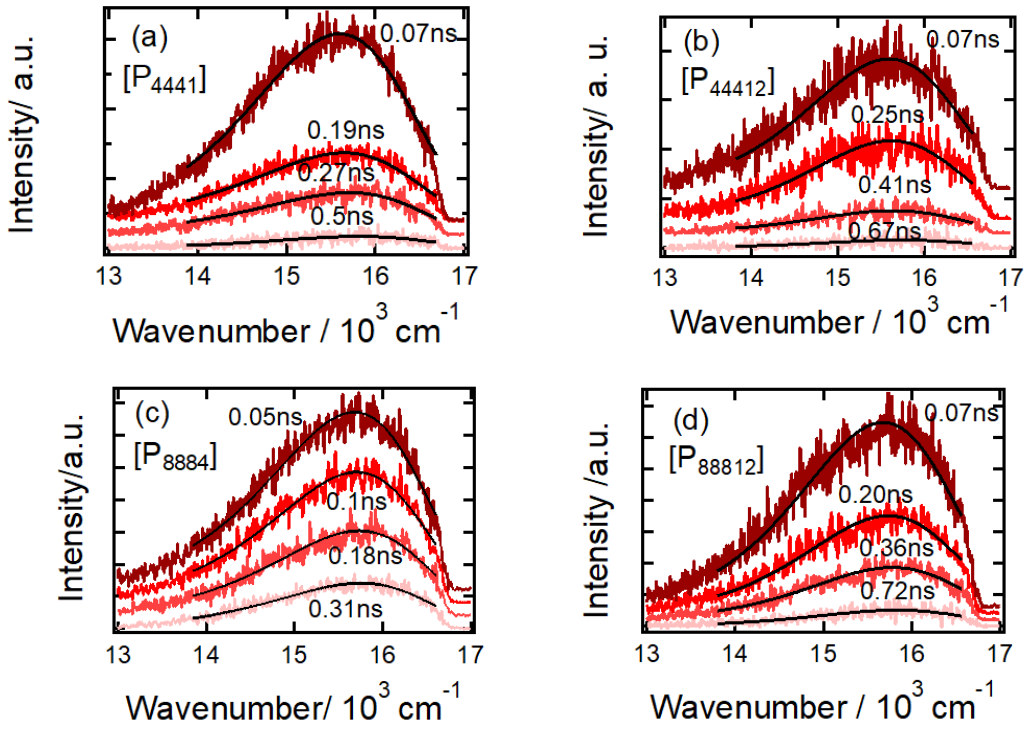

Figure C3. Time-resolved emission spectrum of the PAPT radical in ILs ((a) $[P_{4441}][NTf_2]$, (b) $[P_{44412}][NTf_2]$, (c) $[P_{8884}][NTf_2]$ and (d) $[P_{88812}][NTf_2]$) excited at 10 ps.

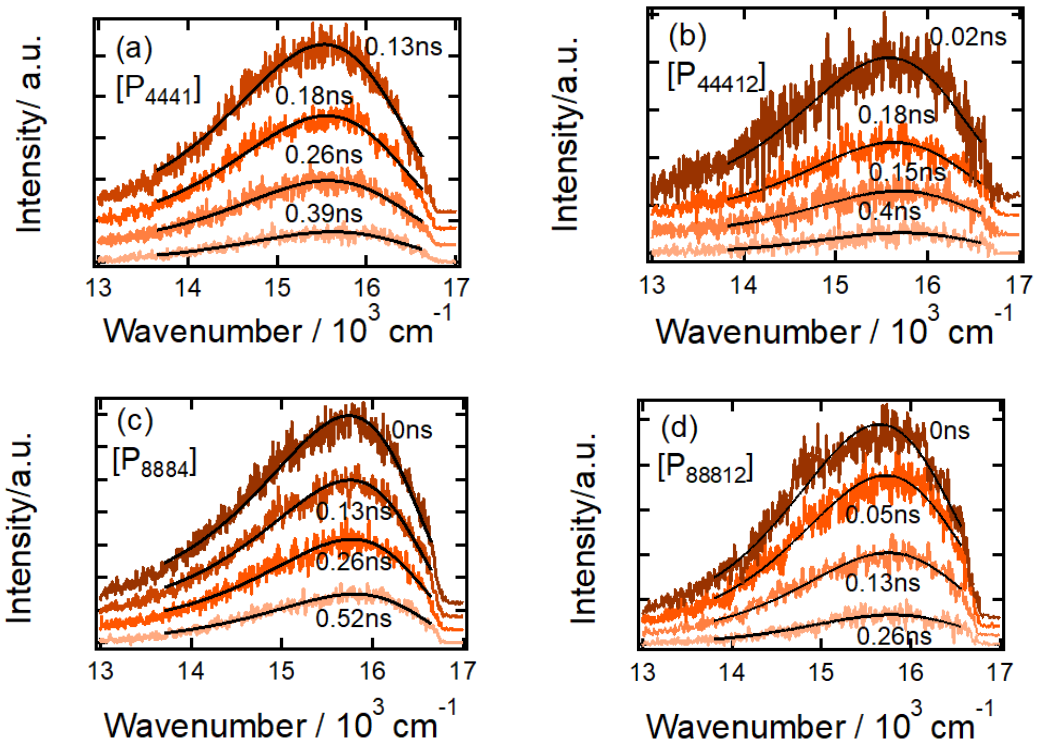

Figure C4. Time-resolved emission spectrum of PAPT radical in ILs ((a) $[P_{4441}][NTf_2]$, (b) $[P_{44412}][NTf_2]$, (c) $[P_{8884}][NTf_2]$ and (d) $[P_{88812}][NTf_2]$) excited at 500 ps

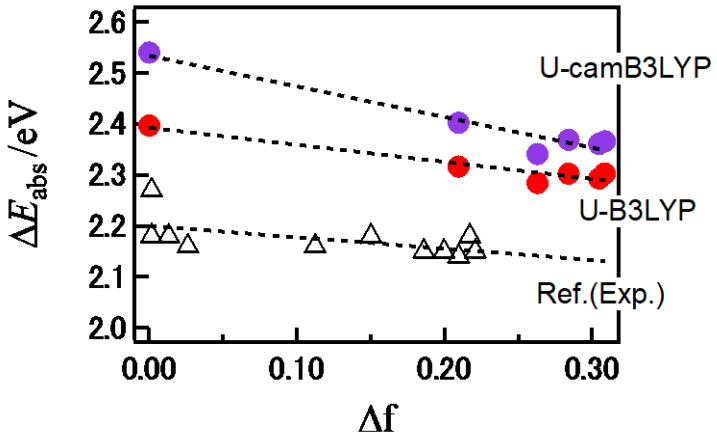

Figure C5. UV-Vis spectrum of PAPT radical in various solvent calculated by unrestricted-camB3LYP (purple) and unrestricted B3LYP (red), together with the experimental results[52].

(a)

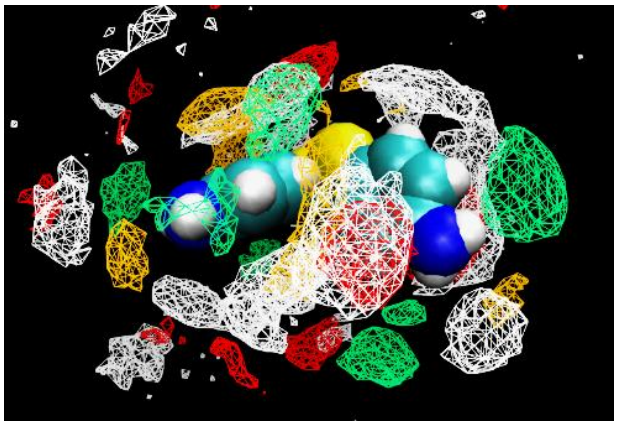

(b)

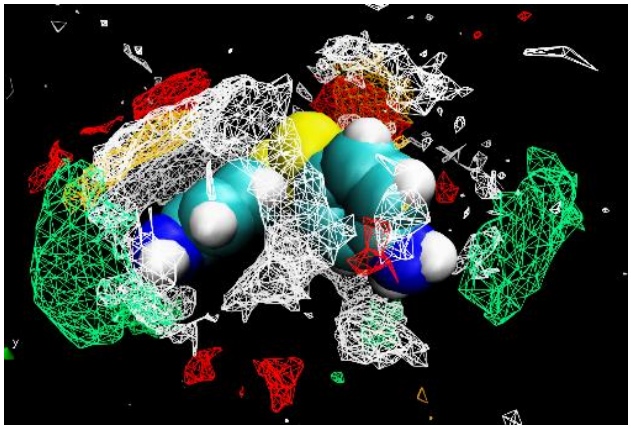

Figure C6. Spatial distribution function of (a) $[P_{4441}][NTf_2]$ and (b) $[P_{8881}][NTf_2]$ around bis-(*p*-aminophenyl)disulfide.

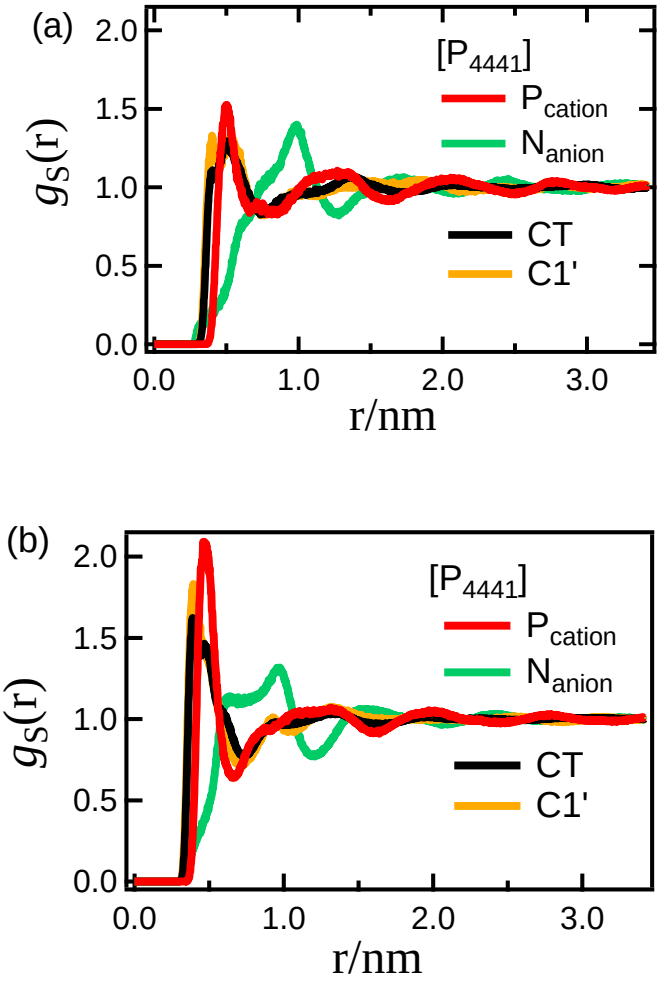

Figure C7-1. Radial distribution function of $[P_{4441}][NTf_2]$ around (a) BPADS and (b) PAPT radical (distribution around sulfur atom).

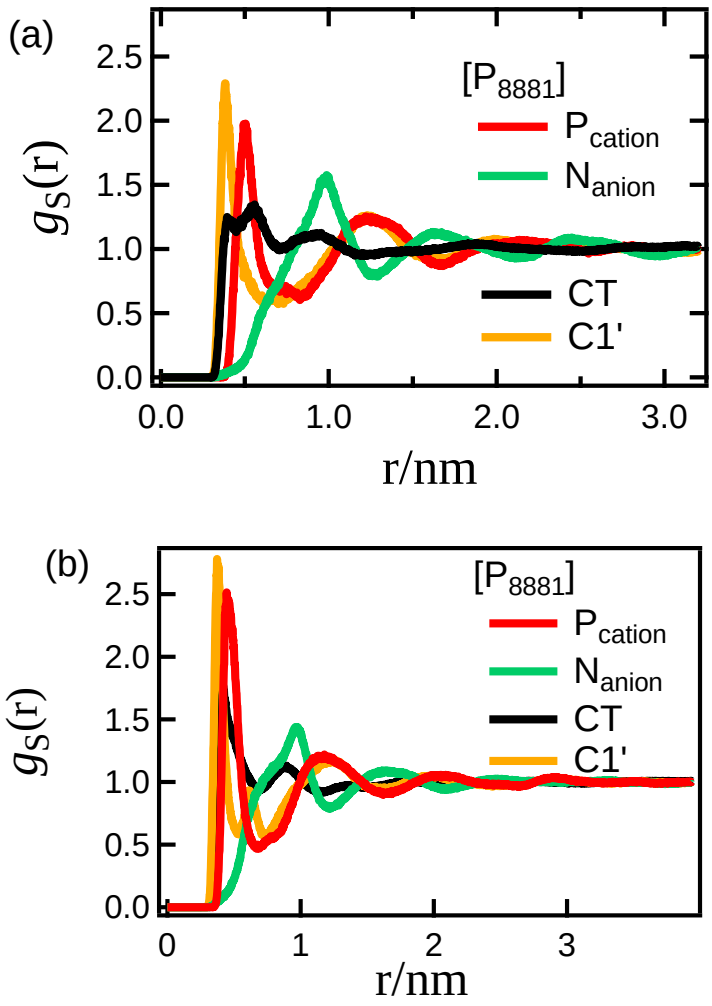

Figure C7-2. Radial distribution function of $[P_{8881}][NTf_2]$ around (a) BPADS and (b) PAPT radical (distribution around sulfur atom).

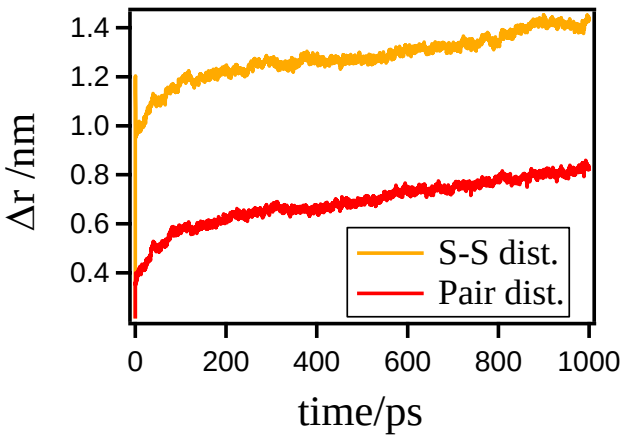

Figure C8. Time profiles of distance between geminate radicals (center of the molecule, red line) and between S atoms in geminate pair in $[P_{4441}][NTf_2]$.

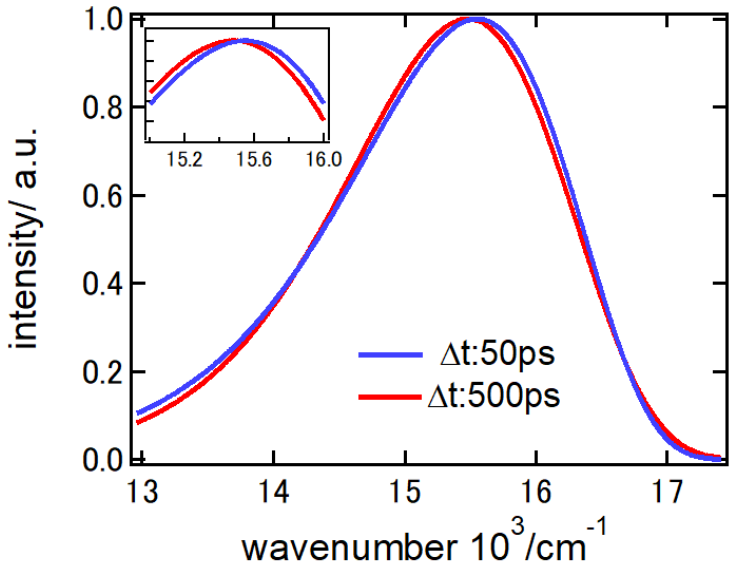

Figure C9. Time averaged emission spectrum of PAPT radical in $[P_{2225}][NTf_2]$ excited at 10ps (blue) and 500ps (red).

References

1. Fleming, G., Chemical applications of ultrafast spectroscopy. **1986**.

2. Mukamel, S., *Principles of nonlinear optical spectroscopy*. Oxford university press New York: 1995; Vol. 6.

3. Hirata, F., *Molecular theory of solvation*. Springer Science & Business Media: 2003; Vol. 24.

4. Lakowicz, J. R., *Principles of Fluorescence Spectroscopy*. Springer US: 2017.

5. Bragg, A. E.; Cavanagh, M. C.; Schwartz, B. J., Linear Response Breakdown in Solvation Dynamics Induced by Atomic Electron-Transfer Reactions. *Science* **2008,** *321* (5897), 1817.

6. Chapman, C. F.; Fee, R. S.; Maroncelli, M., Measurements of the Solute Dependence of Solvation Dynamics in 1-Propanol: The Role of Specific Hydrogen-Bonding Interactions. *The Journal of Physical Chemistry* **1995,** *99* (13), 4811-4819.

7. Sajadi, M.; Weinberger, M.; Wagenknecht, H.-A.; Ernsting, N. P., Polar solvation dynamics in water and methanol: search for molecularity. *Physical Chemistry Chemical Physics* **2011,** *13* (39), 17768-17774.

8. Kumpulainen, T.; Rosspeintner, A.; Vauthey, E., Probe dependence on polar solvation dynamics from fs broadband fluorescence. *Physical Chemistry Chemical Physics* **2017,** *19* (13), 8815-8825.

9. Maroncelli, M.; Fleming, G. R., Computer simulation of the dynamics of aqueous solvation. *The Journal of Chemical Physics* **1988,** *89* (8), 5044-5069.

10. Maroncelli, M., Computer simulations of solvation dynamics in acetonitrile. *The Journal of Chemical Physics* **1991,** *94* (3), 2084-2103.

11. Cichos, F.; Brown, R.; Bopp, P. A., Coupled molecular dynamics/semiempirical simulation of organic solutes in polar liquids. II. Coumarin 153 in methanol and acetonitrile. *The Journal of Chemical Physics* **2001,** *114* (15), 6834-6842.

12. Heid, E.; Moser, W.; Schröder, C., On the validity of linear response approximations regarding the solvation dynamics of polyatomic solutes. *Physical Chemistry Chemical Physics* **2017,** *19* (17), 10940-10950.

13. Rey, R.; Hynes, J. T., Translational versus rotational energy flow in water solvation dynamics. *Chemical Physics Letters* **2017,** *683*, 483-487.

14. Yamaguchi, T.; Yoshida, N.; Nishiyama, K., Relation between Anharmonicity of Free-Energy Profile and Spectroscopy in Solvation Dynamics: Differences in Spectral Broadening and Peak Shift in Transient Hole-Burning Spectroscopy Studied by Equilibrium Molecular Dynamics Simulation. *The Journal of Physical Chemistry B* **2019,** *123* (32), 7036-7042.

15. Hazra, M. K.; Bagchi, B., Non-linearity in dipolar solvation dynamics in water-ethanol mixture: Composition dependence of free energy landscape. *The Journal of Chemical Physics* **2019,**

151 (8), 084502.

16. Loring, R. F.; Yan, Y. J.; Mukamel, S., Time-resolved fluorescence and hole-burning line shapes of solvated molecules: Longitudinal dielectric relaxation and vibrational dynamics. *The Journal of Chemical Physics* **1987,** *87* (10), 5840-5857.

17. Loring, R. F.; Yan, Y. J.; Mukamel, S., Hole-burning spectroscopy of polar molecules in polar solvents: solvation dynamics and vibrational relaxation. *The Journal of Physical Chemistry* **1987,** *91* (6), 1302-1305.

18. Nishiyama, K.; Okada, T., Relaxation Dynamics of Inhomogeneous Spectral Width in Binary Solvents Studied by Transient Hole-Burning Spectroscopy. *The Journal of Physical Chemistry A* **1998,** *102* (48), 9729-9733.

19. Morine, G. H.; Kuntz, R. R., Spectral shifts of the p-aminophenylthyl radical absorption and emission in solution. *Chemical Physics Letters* **1979,** *67* (2), 552-554.

20. Ishizaka, S.; Kotani, M., Laser emission from transient organic free radicals in solution. *Chemical Physics Letters* **1985,** *117* (3), 251-253.

21. Borisevich, N.; Gorelenko, A.; Lysak, N.; Mel'Nichuk, S.; Tikhomirov, S.; Tolkachev, V.; Toltorozhev, G., Luminescence and emission of free radicals in gaseous and condensed phases. *ZhETF Pisma Redaktsiiu* **1986**.

22. Borisevich, N. A.; Buganov, O. V.; Dubovskii, V. L.; Tikhomirov, S. A.; Tolstorozhev, G. B., Femtosecond dynamics of geminate recombination of radicals upon photodissociation of aromatic disulfides. *Optics and Spectroscopy* **2005,** *98* (3), 368-373.

23. Thyrion, F. C., Flash photolysis of aromatic sulfur molecules. *The Journal of Physical Chemistry* **1973,** *77* (12), 1478-1482.

24. Scott, T. W.; Liu, S. N., Picosecond geminate recombination of phenylthiyl free-radical pairs. *The Journal of Physical Chemistry* **1989,** *93* (4), 1393-1396.

25. Ernsting, N. P., Solvation of photolytically generated p-aminophenylthiyl radicals studied by sub-picosecond transient absorption. *Chemical Physics Letters* **1990,** *166* (3), 221-226.

26. Hirata, Y.; Niga, Y.; Okada, T., Photodissociation of aminophenyldisulfide and aminophenylthiol in the liquid phase. Geminate recombination and the dimer formation of p-aminophenylthiyl radical. *Chemical Physics Letters* **1994,** *221* (3), 283-288.

27. Bultmann, T.; Ernsting, N. P., Competition between Geminate Recombination and Solvation of Polar Radicals following Ultrafast Photodissociation of Bis(p-aminophenyl) Disulfide. *The Journal of Physical Chemistry* **1996,** *100* (50), 19417-19424.

28. Hirata, Y.; Niga, Y.; Makita, S. i.; Okada, T., Geminate Recombination of the p-Aminophenylthiyl Radical Pair Produced by the Photodissociation of p-Aminophenyl Disulfide in Nonpolar Solvents. *The Journal of Physical Chemistry A* **1997,** *101* (4), 561-565.

29. Kimura, Y.; Saga, N., Application of the time-resolved spectroscopy on the photo-

dissociation dynamics of disulfide compounds in supercritical fluids. *Journal of Molecular Liquids* **2005,** *119* (1-3), 113-117.

30. Osawa, K.; Terazima, M.; Kimura, Y., Photo-dissociation dynamics of bis(p-dimethylaminophenyl) disulfide in ionic liquids studied by ultrafast transient absorption spectroscopy. *Chemical Physics Letters* **2013,** *564*, 21-25.

31. M. S. S. Esperança, J.; Canongia Lopes, J. N.; Tariq, M.; Santos, L. M. N. B. F.; Magee, J. W.; Rebelo, L. P. N., Volatility of Aprotic Ionic Liquids — A Review. *Journal of Chemical & Engineering Data* **2010,** *55* (1), 3-12.

32. Aparicio, S.; Atilhan, M.; Karadas, F., Thermophysical Properties of Pure Ionic Liquids: Review of Present Situation. *Industrial & Engineering Chemistry Research* **2010,** *49* (20), 9580-9595.

33. Jin, H.; Baker, G. A.; Arzhantsev, S.; Dong, J.; Maroncelli, M., Solvation and Rotational Dynamics of Coumarin 153 in Ionic Liquids: Comparisons to Conventional Solvents. *The Journal of Physical Chemistry B* **2007,** *111* (25), 7291-7302.

34. Samanta, A., Solvation Dynamics in Ionic Liquids: What We Have Learned from the Dynamic Fluorescence Stokes Shift Studies. *The Journal of Physical Chemistry Letters* **2010,** *1* (10), 1557-1562.

35. Kimura, Y.; Suda, K.; Shibuya, M.; Yasaka, Y.; Ueno, M., Excitation Wavelength Dependence of the Solvation Dynamics of 4′-N,N-Diethylamino-3-methoxyflavon in Ionic Liquids. *Bulletin of the Chemical Society of Japan* **2015,** *88* (7), 939-945.

36. Yoshifumi, K., Solvation heterogeneity in ionic liquids as demonstrated by photo-chemical reactions. *Pure and Applied Chemistry* **2020,** (0), 20191116.

37. Lang, B.; Angulo, G.; Vauthey, E., Ultrafast Solvation Dynamics of Coumarin 153 in Imidazolium-Based Ionic Liquids. *The Journal of Physical Chemistry A* **2006,** *110* (22), 7028-7034.

38. Zhang, X. X.; Liang, M.; Ernsting, N. P.; Maroncelli, M., Complete solvation response of coumarin 153 in ionic liquids. *J Phys Chem B* **2013,** *117* (16), 4291-304.

39. Daschakraborty, S.; Pal, T.; Biswas, R., Stokes shift dynamics of ionic liquids: Solute probe dependence, and effects of self-motion, dielectric relaxation frequency window, and collective intermolecular solvent modes. *The Journal of Chemical Physics* **2013,** *139* (16), 164503.

40. Shim, Y.; Duan, J.; Choi, M. Y.; Kim, H. J., Solvation in molecular ionic liquids. *The Journal of Chemical Physics* **2003,** *119* (13), 6411-6414.

41. Roy, D.; Maroncelli, M., Simulations of Solvation and Solvation Dynamics in an Idealized Ionic Liquid Model. *The Journal of Physical Chemistry B* **2012,** *116* (20), 5951-5970.

42. Terranova, Z. L.; Corcelli, S. A., On the Mechanism of Solvation Dynamics in Imidazolium-Based Ionic Liquids. *The Journal of Physical Chemistry B* **2013,** *117* (49), 15659-15666.

43. Kimura, Y.; Fukui, T.; Okazoe, S.; Miyabayashi, H.; Endo, T., Photo-excitation dynamics of N, N-dimethyl-p-nitroaniline in ionic liquids: Effect of cation alkyl-chain length. *Journal of Molecular*

Liquids **2019,** *289*, 111128.

44. M. J. Frisch, et al., Gaussian 09, Gaussian, Inc., Wallingford CT, 2010.

45. D. Van Der Spoel, E. Lindahl, B. Hess, G. Groenhof, A. E. Mark, A. E, H. J. C. Berendsen, *J. Comput. Chem.* 2005, **26**, 1701.

46. C. Kutzner, S. Páll, M. Fechner, A. Esztermann, B. L. de Groot, H. Grubmüller, *J. Comput. Chem.*2019, **40**, 2418.

47. J. N. Canongia Lopes, J. Deschamps and A. A. H. Pádua, *J. Phys. Chem. B* 2004, **108**, 2038.

48. J. N. Canongia Lopes and A. A. H. Pádua, *J. Phys. Chem. B* 2006, **110**, 19586.

49. M. L. Horng, J. A. Gardecki, A. Papazyan and M. Maroncelli, *J. Chem. Phys.* 1995, **99**, 17311.

50. E. A. Carter, J. T. Hynes, J. Chem. Phys., 1991, **94**, 5961

51. Ishizaka, S.; Kotani, M., Estimation of extinction coefficient and radiative lifetime of a free radical, p-aminophenylthiyl. *Chemical Physics Letters* **1987,** *139* (1), 89-92.

52. Ito, O.; Matsuda, M., Solvent effect on rates of free-radical reactions. 2. Addition of the p-(dimethylamino)benzenethiyl radical to .alpha.-methylstyrene. *The Journal of Physical Chemistry* **1984,** *88* (5), 1002-1005.

53. Tsunashima, K.; Sugiya, M., Physical and Electrochemical Properties of Room Temperature Ionic Liquids Based on Quaternary Phosphonium Cations. *Electrochemistry* **2007,** *75* (9), 734-736.

54. Carvalho, P. J.; Ventura, S. P. M.; Batista, M. L. S.; Schröder, B.; Gonçalves, F.; Esperança, J.; Mutelet, F.; Coutinho, J. A. P., Understanding the impact of the central atom on the ionic liquid behavior: Phosphonium vs ammonium cations. *The Journal of Chemical Physics* **2014,** *140* (6), 064505.

55. Philippi, F.; Rauber, D.; Zappc, J.; Hempelmann, R., Transport properties and ionicity of phosphonium ionic liquids. *Phys. Chem. Chem. Phys*., **2017**, 19, 23015-23023.

Chapter 5

Geminate Recombination in Ionic Liquids: Analysis with Smoluchowski-Collins-Kimball Equation

5.1. Introduction

In Chapter 4, we have presented spectroscopic studies on the photodissociation reaction in ionic liquids (ILs) and discussed the solvation dynamics of ILs appeared in the spectrum shift of the transient absorption and the time-resolved emission of the photo-products. In this Chapter, we will focus on the recombination dynamics of the photo-products, *p*-aminophenylthyil (PAPT) radicals, which can be evaluated by the spectrum integral of the transient absorption. Main topic of this chapter is application of theoretical model to simulate the experimental results.

Geminate recombination dynamics in solution have been a well-examined theme both experimentally and theoretically.[1] The first work goes back to 1934 by Frank and Rabinowitsch. They proposed that solvent molecules could trap photo dissociated atoms or radicals, and force them to recombine; the effect is commonly called the solvent cage effect.[2] This effect emerges in various ways after the photodissociation as described below. Before the complete dissociation, photodissociated atoms or radicals first experience

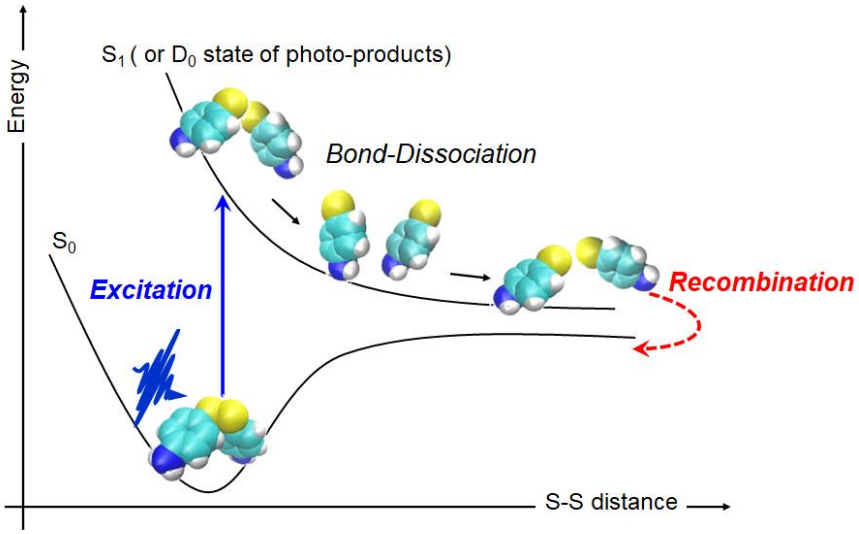

Figure 5-1. Photodissociation reaction of bis-(*p*-amionophenyl) disulfide and following recombination reaction of geminate pair of *p*-aminothyilradicals.

collision with surrounding solvent molecules to dissipate their excess energy. Some of them recombine in a solvent cage (primary geminate recombination). Other fractions of geminate pairs can escape from the cage. They still have probability to recombine by diffusing back (secondary geminate recombination). Remaining fractions of geminate pairs that already escape from solvent cage do not recombine geminately. By diffusing in a solution until they meet other atoms or radicals, nongeminate recombination is occurred.

So far, several groups have worked on the photodissociation and following recombination dynamics of sulfur compounds both by experimentally[3-9] and theoretically.[10] Experimentally, Thyrion measured the transient absorption spectra of various aromatic sulfur molecules and found that the time-profile of the concentration of photodissociated products showed two different decay components and the initial decay component was several times faster than the total decay.[3] In his work, however, the recombination kinetic was not fully discussed. Main approach to simulate the experimentally obtained time-profile of the concentration of photodissociated products was to employ the diffusion equation based on the Smoluchowski's theory (details of the theory is described in the following section). Scott et al. investigated solvent and temperature dependence of the recombination kinetics of diphenyl disulfide obtained by transient absorption measurements in liquid alkanes.[4] They compared experimentally obtained time-profile of the concentration of the radical with the time-dependent survival probability of radical pair solved by the Smoluchowski's diffusion equation considering the partially reflecting boundary condition where the inward flux of particles across the reaction boundary is proportional to the concentration at the surface. Ernsting et al.[6] investigated the photo-dissociation of bis-(*p*-amionophenyl) disulfide (BPADS) in various alcohols and propylene carbonate, and analyzed the experimental results with the

same theoretical model. According to their analysis, Smolchowski's model couldn't reproduce the survival probability of the radical over the whole time-range. Especially in long-time region, theoretical model predicted a lower yield of the escaped radical than actual, if they fit the time trace in the initial several picoseconds to the model equation. This deviation was attributed to the competition of the recombination dynamics with solvation dynamics, formation of solvent cage.

As mentioned in Chapter 1, improvement of diffusion equation based on Smoluchowski's theory has been conducted to reproduce experimentally or computationally observed reaction kinetics. Smoluchowski-Collins-Kimball (SCK) equation where boundary condition at reaction radius is revised, is the representative example and have been shown to reproduce transient dynamics.[11] Implements of an intermolecular potential, for example square well-potential and/or Coulomb potential[12], to diffusional equation has been another the strategies to reproduce the experimental and computational observation. Lee et al. has reported an analytic expression of Green's function for Smoluchowski equation with Coulomb potential and a reaction sink term, and applied the formulation to the recombination kinetics.[13] Both the effects of attractive and repulsive interactions on the recombination dynamics were investigated, and the accuracy of the expression of Green's function were confirmed by comparing the numerical solution of survival probability of geminate recombination for the same equation.

In ionic liquids (ILs), recombination kinetics of various types of atoms or radicals have also been examined by several research groups.[9,14-16] Strehmel et al. reported recombination dynamics of photodissociated product of triphenylimidazolyl radical in various ILs composed of imidazolium cation, by measuring transient absorption

spectrum.[14] They discuss dependence of recombination rate constant and activation parameters for recombination on the species of ILs and solvent viscosity. Osawa et al. also investigated photodissociation and recombination dynamics of dimethyl-analogues of BPADS (bis(p-dimethylaminophenyl) disulfide) in ILs composed of pyrrolidinium cation and piperidinium cation, and in conventional solvents (methanol and ethylene glycol). [9] In those ILs, geminate recombination occurred faster than in methanol, but was like that in ethylene glycol. The analysis based on the Smoluchowski's model could not reproduce the survival probability as was the case of conventional liquid solvents. It is unclear whether the deviation of the recombination yield from the theoretically predicted value is due to the unique properties of ILs as a solvent or not.

In this chapter, geminate recombination of PAPT radical was analyzed with diffusional equation based on SCK theory. To take the effect of the potential well between radical pair into account, square well potential (SWP) is implemented to the SCK equation. We discuss optimized parameters such as the mutual diffusion coefficient of the radicals, the cage radius and the well depth, based on analytic expression of the model.

5.2. Experiments

Experimental details for measuring the transient absorption of the PAPT radical are described in the previous chapter. From the transient absorption spectrum of the PAPT radical (Figure 4-5 and Figure C1), the concentration of the radical was evaluated by integration of the absorption signal using the fitting parameters obtained by eq (4.3). Time profiles of the radical concentration are given in Figure C2.

To evaluate solute-solvent interaction and solvation structure of ILs, molecular dynamics (MD) simulation of the photodissociation reaction were conducted. The simulation procedure is given in Chapter 4. In this chapter, we only refer to the radial distribution function of selected atomic group of $[P_{4441}][NTf_2]$ around BPADS molecule in equilibrium simulations.

5.3. Theoretical Formulations

5.3.1. Definition of the System

The purpose of this section is to provide an analytic expression for the survival probability of radical pairs after the photodissociation. The recombination process of radical pairs can be described by the SCK model which describes the diffusion-limited reaction.[11,17] In the SCK model, two identical spherical molecules diffuse with a relative diffusion constant D under the influence of a potential of mean force (PMF) $V(r)$ which depends only on their relative separation r. These species can react irreversibly to form a bound molecule at the contact separation a. The reaction event is implemented with either the boundary condition at the contact separation or the reaction sink function. The combination of a delta-function reaction sink and the reflecting boundary condition is equivalent to the radiation boundary condition.[18] In the following, we employ the reaction sink expression.

Let $\rho(r,t)$ be the probability density that the inter-particle distance is r, at time t. Then, the time evolution equation of the probability density is given as,[18]

$$\frac{\partial\rho(r,t)}{\partial t} = \hat{\mathcal{L}}(r)\rho(r,t) - S(r)\rho(r,t), \qquad \hat{\mathcal{L}}(r) = D\frac{1}{r^2}\frac{\partial}{\partial r}r^2 e^{-U(r)}\frac{\partial}{\partial r}e^{U(r)} \tag{5.1}$$

where the reaction sink function is defined with the delta function and the second-order rate coefficient k_a,

$$S(r) = k_a\frac{\delta(r-a)}{4\pi a^2}. \tag{5.2}$$

The PMF is scaled by Boltzmann constant k_B and temperature T, $U(r) = V(r)/k_BT$. The initial, boundary and asymptotic conditions for $\rho(r,t)$ are given by

$$\rho(r,0) = \frac{\delta(r-r_0)}{4\pi r^2}, \quad \text{(initial condition)} \tag{5.3}$$

$$\frac{\partial}{\partial r} e^{U(r)} \rho(r,t)\Big|_{r=a} = 0, \quad \text{(reflecting boundary condition)} \tag{5.4}$$

$$\lim_{r\to\infty} \rho\,(r,t) = 0. \quad \text{(asymptotic condition)} \tag{5.5}$$

For simplicity, we assume the initial probability density is sharp at some distance r_0. The survival probability of the radical pairs is given as the spatial integration of the probability density that is the solution of eq (5.1),

$$\Phi(t) = 4\pi \int_a^\infty dr r^2\, \rho(r,t). \tag{5.6}$$

5.3.2. Free Diffusion Model

In the absence of the PMF, $U(r)=0$, the radical species freely diffuse in the region $r > a$. In this case, the survival probability is analytically given as[11]

$$\begin{aligned} \Phi(t) = 1 - \frac{a}{r_0}\frac{k_a}{k_a + 4\pi a D}\Bigg[&\operatorname{erfc}\left(\frac{r_0 - a}{2\sqrt{Dt}}\right) \\ &- exp\left(\gamma^2 Dt + \gamma(r_0 - R)\right)\operatorname{erfc}\left(\gamma\sqrt{Dt} + \frac{r_0 - a}{2\sqrt{Dt}}\right)\Bigg] \end{aligned} \tag{5.7}$$

where erfc(x) is the complementary error function,

$$\operatorname{erfc}(x) = \frac{2}{\sqrt{\pi}} \int_x^\infty dt\, e^{-t^2}, \tag{5.8}$$

and γ is defined as

$$\gamma = \frac{1}{a}\frac{k_a + 4\pi a D}{4\pi a D} \tag{5.9}$$

In the limit of $t \to \infty$, the survival probability becomes

$$\lim_{t\to\infty} \Phi(t) = 1 - \frac{a}{r_0}\frac{k_a}{k_a + 4\pi a D}. \tag{5.10}$$

5.3.3. Square Well Potential Model

As reported by Bultmann et al., the SCK model without the PMF failed to explain the survival probability of radical pairs in polar solvents.[6] The effect of PMF is significant to take into account the short-time dynamics.[19] In the present study, we employ the square well potential (SWP) as the model for the PMF,

$$U(r) = -E\Theta(R - r) = \begin{cases} 0 & (r > R) \\ -E & (r < R)' \end{cases} \tag{5.11}$$

where Θ is the Heaviside's step function, R is the position of the potential barrier, and E is the depth of the potential well. According to the asymptotic analysis of the SCK equation by Agmon et al.,[20] the long-time asymptotic expression of the survival probability for the SWP model is given by

$$\begin{aligned} \Phi(t) \sim 1 - \frac{a_{\text{eff}}}{r_{\text{eff}}}\frac{k_{\text{eff}}}{k_{\text{eff}} + 4\pi D a_{\text{eff}}}\Bigg[1 \\ - \{1 - (r_{\text{eff}} - a_{\text{eff}})\gamma_{\text{eff}}\}\mathrm{e}^{\gamma_{\text{eff}}^2 Dt}\mathrm{erfc}\left(\sqrt{\gamma_{\text{eff}}^2 Dt}\right)\Bigg] \quad (t \to \infty), \end{aligned} \tag{5.12}$$

where we define the parameters as

$$k_{\text{eff}} = k_a e^E, \tag{5.13}$$

$$a_{\text{eff}} = a\chi(a), \tag{5.14}$$

$$r_{\text{eff}} = r_0\chi(r_0), \tag{5.15}$$

$$\gamma_{\text{eff}} = \frac{k_{\text{eff}} + 4\pi a_{\text{eff}} D}{4\pi a_{\text{eff}} D}\frac{1}{a_{\text{eff}}}, \tag{5.16}$$

$$\chi(r) = \frac{R}{r + (R - r)e^{-E}} \tag{5.17}$$

The details of the derivation of eq (5.12) is shown in Appendix D1. Eq (5.12) is exact only for the long-time limit $t \to \infty$,

$$\lim_{t\to\infty} \Phi(t) = 1 - \frac{a_{\text{eff}}}{r_{\text{eff}}} \frac{k_{\text{eff}}}{k_{\text{eff}} + 4\pi a_{\text{eff}} D}. \tag{5.18}$$

Eq (5.12) behaves as a good approximation in the long-time region but a poor approximation in the short-time region. To obtain the exact result in the whole time-region, we provide the analytic expression by means of the Green function method (in Appendix D2). However, because the analytic expression is obtained only in the Laplace space, it is not appropriate for the parameter fitting to experimental results.

5.4. Results and Discussion

5.4.1. Experimental results and simulation with the free diffusion model

The details of the analysis of the transient absorption spectrum of the radical is described in Chapter 4. In this chapter, we describe a brief summary. Figure 5-2 shows the transient absorption spectrum after the photodissociation in ILs ([P_{4441}][NTf_2] and [N_{4441}][NTf_2]). As shown in the transient absorption spectrum, spectrum intensity is decreased with time due to the geminate recombination. In order to discuss the concentration change with time, we evaluated the spectrum integral at each time which is defined as spectrum integral at each time as follows

$$I(t) = \int_{-\infty}^{\infty} \frac{\Delta \mathrm{OD}(t, \tilde{\nu})}{\tilde{\nu}} d\tilde{\nu}, \tag{5.19}$$

In evaluation of the spectrum integral, we fit the transient spectrum by a log-normal function, and analytically calculated the integral as described in Chapter 4.

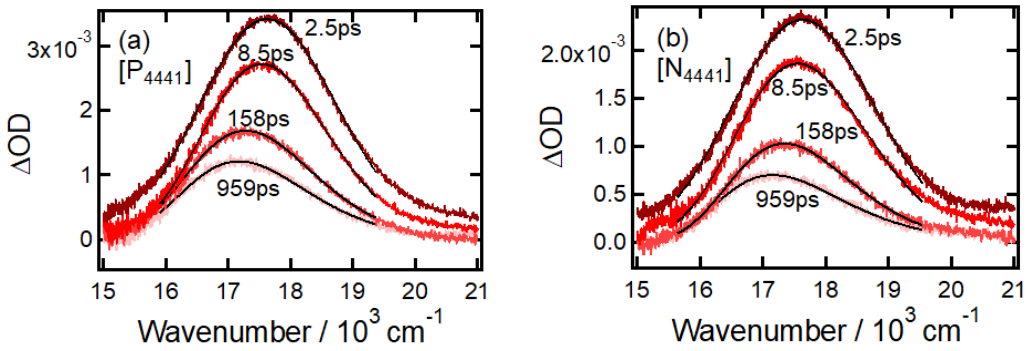

Figure 5-2. Absorption spectrum of PAPT radical generated after the photo-dissociation in (a) [P_{4441}][NTf_2], (b) [N_{4441}][NTf_2].

Figure 5-3 shows time-profiles of the radical concentration (normalized by the maximum value) in various ILs composed of tetraalkylphosphonium ([P_{4441}][NTf_2] and ([P_{8881}][NTf_2]) and tetraalkylammonium ([N_{1113}][NTf_2] and ([N_{8881}][NTf_2]). Despite the variety in the viscosity of solvent ILs, the yields of the geminate recombination estimated

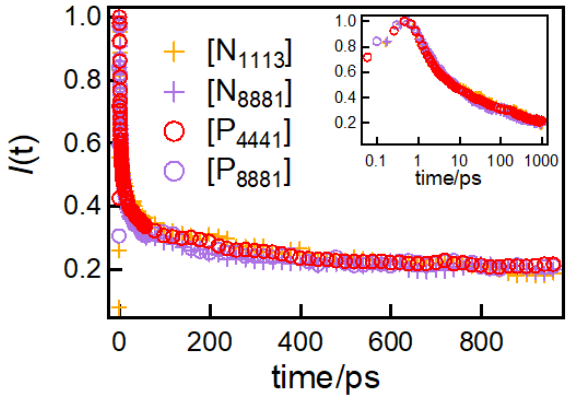

Figure 5-3. Time-profile of spectral first moment of radical absorption various ILs. Inset graph is semi-log plot of time.

at 100 ps are approximately the same, 70% in all ILs. It is also noted that the time-profiles of the radical concentration were quite similar: the concentration dramatically decreased (nearly 50%) in the first ten picoseconds followed by a gradual decrease.

The time-profiles in Fig. 5-3 were first simulated by a simple diffusion-limited model. In eq (5.7), we assumed that diffusion coefficient D, initial distance, r_0 were parameters. The contact distance a is 7.2 Å which is twice of the distance between the center of aromatic ring and the center of disulfide bond. Since initial geminate recombination: the case occurred when $r_0 = a$, isn't included in this model, we assumed that $t = 0$ for the theoretical calculation is time when the concentration of geminate radical reaches maximum and that k_a is second-order diffusion-limited rate constant (3×10^{13} cm^3 s^{-1}) reported in the previous paper.[3]

First, we simulated the time-profiles from t_0 when the radical concentration is maximum, to 1000 ps. In simulating the theoretical curve, we manually changed the parameter of the initial distance r_0 and optimized the diffusion coefficient. Black curves in Figure 5-4 show the fitting results to the experimentally obtained time-profiles. The parameters obtained by the fit are summarized in Table D1-1. The best fit value of the initial distance was

found to be 7.25 Å. As shown in the figure, the free diffusion model could not simulate experimental results. The deviation appears both in the short (approximately within 10 ps) and in the final yield of recombination. In short time region, the experimentally obtained yield of PAPT radicals decreased within 10 ps after the photodissociation significantly rather than theoretical prediction from diffusional model. Since the formation of solvent cage and the recombination dynamics is competing process as mentioned in Introduction, immediately after the photodissociation, the recombination of geminate pair confined in the solvent cage would be promoted, which results in the deviation from the experimental results in the early time. For the long time region, it is found that the final yield of geminate radical is smaller compared to the experimental one. If we simulated the experimental time profile in the longer time region than 20 ps

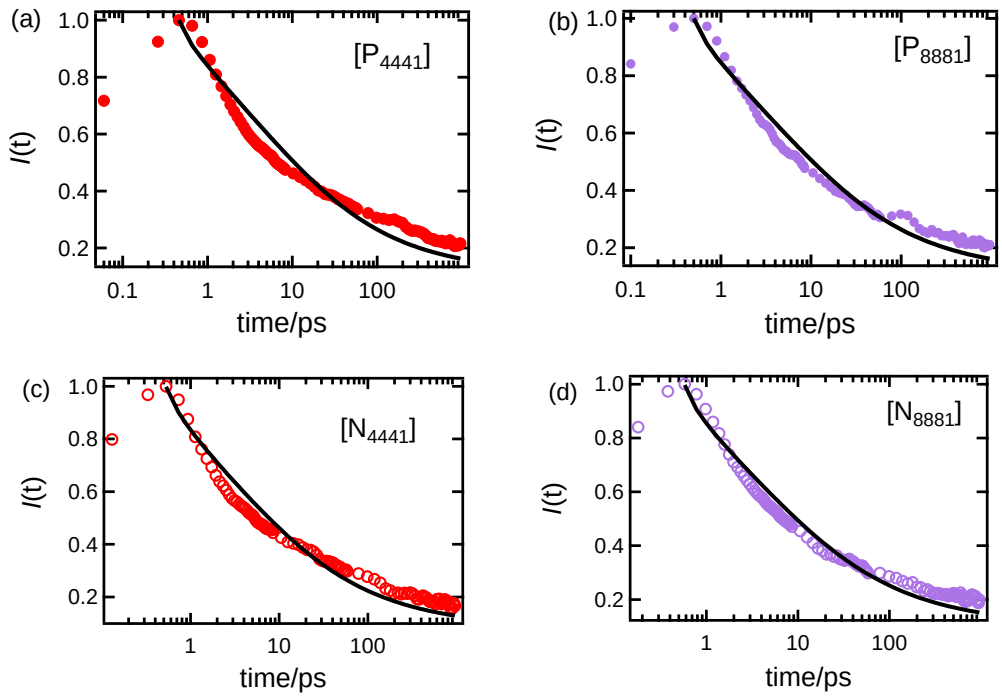

Figure 5-4. Time profiles of spectrum integral in (a) $[P_{4441}][NTf_2]$, (b) $[P_{8881}][NTf_2]$, (a) $[N_{4441}][NTf_2]$ and (d) (a) $[N_{8881}][NTf_2]$calculation results obtained by fitting the profile to free diffusion model (eq. (5.7)).

excluding the initial fast decay component, experimental profile was well simulated for r_0 = 6.8 Å which was smaller than reaction radius. When r_0 was fixed to the optimized value determined for full range fitting (7.25 Å), the fitting profile was not so different from the result of the full range fitting. Therefore, the parameters optimized for the short time behavior could not reproduce the long time dynamics, and the parameters optimized for the long time-dynamics was meaningless. Fitting results and obtained parameter (diffusion coefficient) are shown in Appendix D (Table D1-2 and Figure D1). In the following section, we will discuss the recombination dynamics by the theoretical model including the solvent cage.

5.4.2. Simulation with SWP model

Here we will discuss the modeling including the solvent cage as the SWP as described in section 5.3.3. Using long-time asymptotic expression, experimentally obtained time-profiles were simulated under several assumption. The validity of the optimized parameters was confirmed by the numerical calculation of the survival probability with the analytic form of the SWP model (eq. (5.12)) using optimized parameters.

Following are the fitting procedure using the asymptotic form for $t \to \infty$. We first select fitting parameters, $x(1)$, $x(2)$ and $x(3)$ as,

$$x(1) = D/{a_{\mathrm{eff}}}^2 \tag{5.21}$$

$$x(2) = \frac{k_{\mathrm{eff}}}{4\pi a_{\mathrm{eff}} D} = \frac{k_a \exp(\beta E)}{4\pi D a_{\mathrm{eff}}} \tag{5.22}$$

$$x(3) = \frac{a_{\mathrm{eff}}}{r_{\mathrm{eff}}} \tag{5.23}$$

for ease of treatment in the least-square fitting procedure using MATLAB software (version R2019b). Using these parameters, eq (5.12) can be rewritten as

$$\Phi(t) \sim 1 - \frac{x(2)}{1+x(2)}\left[x(3)\right. \\ \left. - \{1-(2+x(2))(1-\mathrm{x}(3))\}\mathrm{e}^{x(4)t}\mathrm{erfc}\left(\sqrt{\mathrm{x}(4)t}\right)\right] \tag{5.24}$$

where $x(4) = x(1)(1+x(2))$. The experimentally obtained recombination time-profiles were fit in time range of 20-1000 ps, and all parameters ($x(1)$, $x(2)$ and $x(3)$) were adjustable. Since there are six input parameters (E, R, r_0, a, D, k_a), we have to fix at least three parameters in order to evaluate other parameters from the obtained results $x(1)$, $x(2)$, and $x(3)$. As in the case of the Smoluchowski model calculation, the contact distance a is 7.2 Å which is twice of the distance between the center of aromatic ring and the center of disulfide bond. We assumed that k_a is second-order diffusion-limited rate constant (3×10^{13} cm^3 s^{-1}) reported in the previous paper.[3] Since the recombination yield and dynamics in various ILs are quite similar (Fig. 5-3), the cage radius R was assumed to be independent of solvent species and fixed to a certain value. In a SWP model, R should take a close value to r_0. We tested several value in the range of $7.2 < R < 8$. Then, appropriate one was determined by the numerical answer of analytic form calculated with optimized parameters. From the optimized parameters ($x(1)$, $x(2)$ and $x(3)$), we determined the mutual diffusion coefficient D, the most important parameter to describe geminate recombination as following procedure. We also obtain the value of E which describes the cage strength around the radical.

Examples of fitting of experimental time-profiles in $[P_{4441}][NTf_2]$, $[P_{8881}][NTf_2]$, $[N_{4441}][NTf_2]$ and $[N_{8881}][NTf_2]$ are shown in Figure 5-5 (a), (b), (c), and (d), respectively. Other results are summarized in Supplementary materials (Figure D2). Red markers are the time-profiles of the radical concentration determined from experiments, and green curves are calculation results by fitting the experimental results in the time range from 20

to 1000 ps to the asymptotic form. The fitting curve using the asymptotic form seems to successfully reproduce the experimental results in the long time-region, where the simple diffusion model fails to simulate. From the optimized parameters ($x(1), x(2)$ and $x(3)$), we determined D, E and r_0 by assuming R = 7.5 Å, which are summarized in Table 5-1.

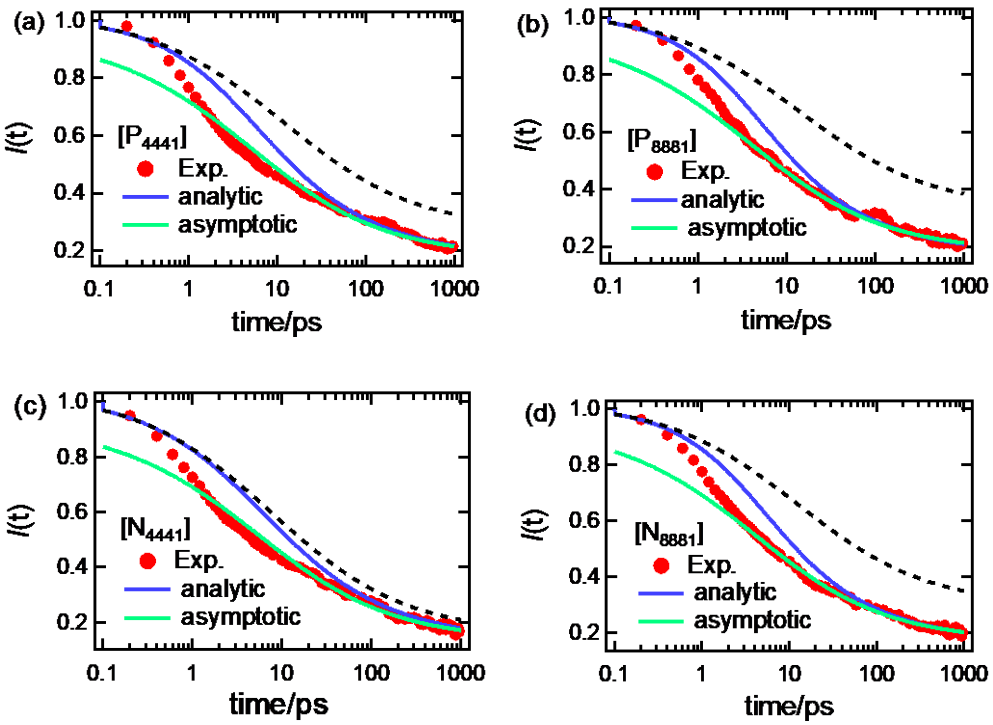

Figure 5-5. Time profiles of the dissociation yield of the PAPT radical in various ILs. Red circles are experimental traces, green curves are the fitting results using the asymptotic form (eq (5.12)) using the data from 20 ps to 1000 ps, and blue curves are the numerical calculation results of the analytic form (eq. (D.31)) using the optimized parameters obtained by the fitting.

To examine validity of these fitting results, we numerically solved analytic form of the SWP model, eq (D.31) with optimized parameters. In Fig. 5-5, blue curves represent the numerical answers of eq (D.31) with the optimized parameters in the case of R = 7.5 Å. In each IL, an analytic form is coincident with the asymptotic form in the time-range (20-1000ps) applied to fitting. In the short time-region where the asymptotic

form does not cover, the analytic form calculated with the parameters in Table 5-1 captures experimental trend reasonably; the recombination yield significantly decreases within 10 ps, although there still remains the deviation from the experimental profile. Here we denote what happened if we use the larger value of R to obtain other parameters. In Table D2, we summarized the values of E, D_{fit}, and r_0 obtained from the same optimized parameters of $x(1)$, x (2) and x (3) when R is assumed to be 8.0, 8.5 and 9.0 Å. The potential well (E) becomes somewhat large and the diffusion coefficient become twice. Figure 5-6 shows examples of the numerical calculations of analytic form in $[P_{4441}][NTf_2]$ when R= 7.5, 8.0, 8.5 and 9.0 Å. Numerical solution of analytic form for other ILs are summarized in Supporting materials (Figure. D3). As is shown from Fig. 5-6, all numerical solutions for various values of R could reproduce the experimentally obtained time-profiles in long time region and final recombination yield. On the other hand, deviation is found in the short time region within 100 ps where experimentally obtained recombination yield drastically decrease. The deviations are more evident for the large R. When the value of R is large, reactants could diffuse in the cage for relatively long time, which retards the recombination reaction to start. Although there is still discrepancy

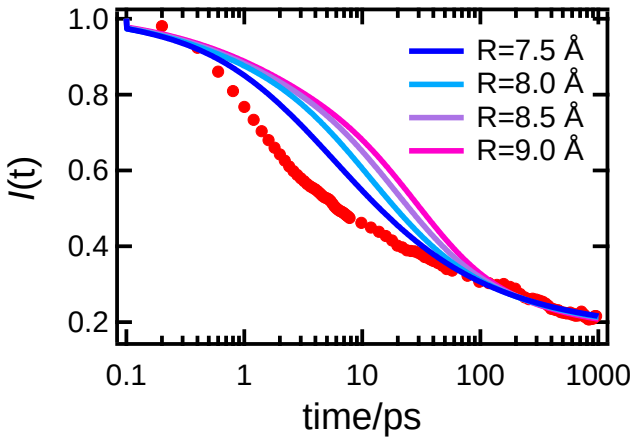

Figure 5-6. Numerical solution of analytic form of SWP model with obtained parameters for $[P_{4441}][NTf_2]$. Profiles represented with red markers are experimental results.

between experimental result and theoretical solution even R =7.5 Å, the parameters summarized in Table 5-1 would be most plausible to describe our experimental results within the model used here. Based on the comparison between experimental time-profiles and calculation results, the validity of the obtained parameters is discussed in the next section.

Table 5-1. Potential well E, diffusion coefficient D and initial separation of geminate radicals r_0 obtained from fitting to eq. (5.12). D_{fit} is fitting-obtained mutual diffusion coefficient of pair of geminate radicals.

	R = 7.5 Å		
Ionic liquids	E /kJ mol	D_{fit} /10^{-5} cm^2 s^{-1}	r_0/Å
$[N_{1113}]^+$	1.78	2.03	7.35
$[N_{2225}]^+$	1.60	1.93	7.34
$[N_{4441}]^+$	1.72	1.49	7.34
$[N_{8881}]^+$	1.79	2.09	7.35
$[P_{2225}]^+$	1.76	3.02	7.35
$[P_{4441}]^+$	1.45	1.99	7.31
$[P_{8881}]^+$	1.62	2.12	7.34
$[P_{8884}]^+$	1.82	3.10	7.35

5.4.3. Discussion on the Modeling Parameters

First, we discuss the diffusion coefficient D_{fit} obtained from the fit of the recombination trace. Unfortunately, the diffusion coefficients of the PAPT radical has not been determined experimentally. Generally, the Stokes-Einstein (SE) equation based on the conventional hydrodynamic theory has been used to estimate the order of the diffusion coefficient. In the SE equation, the diffusion coefficient is given by

$$D_{\mathrm{SE}} = \frac{k_{\mathrm{B}}T}{C\eta r_{\mathrm{SE}}}. \tag{5.25}$$

where C is the parameter for the boundary condition of the flow at the sphere surface (6π or 4π), η the viscosity of the solvent, and r_{SE} is the Stokes-radius of the radical assumed to be sphere. Since SE equation contains a lot of approximations (e.q. the shape of solute, the neglect of the solute-solvent interaction, and so on), deviations from experimentally obtained diffusion coefficient have been reported for various systems. For ILs, it has been indicated that the volume ratio of solute and solvent ILs is an important factor for the solute diffusion. Kaintz et al. collected the diffusion coefficients of a lot of molecules in ILs, and took the correlation of the ratio between the experimentally determined diffusion coefficient and D_{SE} with the ratio of the volumes between solute and solvent.[21] Later, Kimura et al. added data of diffusion coefficients of three solutes (carbon monoxide, diphenylacetylene, and diphenylcyclopropenone) in various fluids containing ILs to the collection by Kainz et al., and proposed an empirical equation including the effect of the ratio of the size as follows;[22]

$$D_{\mathrm{emp}}(\mathrm{m^2 s^{-1}}) = 1.16 \times 10^{-11} \left(\frac{T(\mathrm{K})}{\eta(\mathrm{mPa\ s})}\right)^{0.95} \left(\frac{V_U}{V_V}\right)^{-1.17}. \tag{5.26}$$

In this equation, V_U and V_V represent van der Waals volume of solute and solvent (sum of cation and anion), respectively. In Table 5-2, diffusion coefficient obtained from fitting D_{fit} are compared with D_{SE} and D_{emp}. The Stokes radius was assumed to be 2.6 Å taken from ref. 23. The van der Waals volume of the solute V_{V} (114 Å^3) was calculated from the Bondi method,[24] and those of ILs are taken from literatures[21,22].

Table 5-2. Comparison of diffusion coefficients obtained by the fit to the recombination trace D_{fit} (R = 7.5 Å) with the estimated values from the SE relation D_{SE} and the empirical equation D_{emp}, together with the viscosity of ILs. Note that D_{fit} is mutual diffusion coefficient.

Ionic liquids	V_U / Å^3	η/mPas (295 K)	D_{fit} /10^{-5} cm^2 s^{-1}	D_{SE} /10^{-5} cm^2 s^{-1}	D_{emp} /10^{-5} cm^2 s^{-1}	Ratio (=D_{fit}/2D_{emp})
N_{1113}	288	90	2.03	9.25×10^{-3}	4.8×10^{-2}	21
N_{2225}	373	253	1.93	3.28×10^{-3}	2.9×10^{-2}	33
N_{4441}	407	423	1.49	1.97×10^{-3}	1.1×10^{-2}	67
N_{8881}	611	722	2.09	1.15×10^{-3}	1.6×10^{-2}	65
P_{2225}	383	103	3.02	8.04×10^{-3}	5.8×10^{-2}	26
P_{4441}	417	206	1.99	4.02×10^{-3}	2.7×10^{-2}	37
P_{8881}	621	664	2.12	1.25×10^{-3}	1.7×10^{-2}	62
P_{8884}	740	413	3.10	2.01×10^{-3}	3.0×10^{-2}	52
EG[a)]		17	2.34	4.89×10^{-2}	-	-

a) Recombination yield of *p*-dimethylaminophenythyilradical in ethylene glycol (EG) is referred from ref. 9.

As is shown in the Table 5-2, the SE equation underestimate the diffusion coefficients in comparison with those obtained from the empirical equation, especially for the large cation. In comparison with the D_{emp}, the simulated diffusion coefficient D_{fit} from the recombination trace is larger in one order of magnitude, and the deviation is larger for the ILs with larger molecular size or viscosity.

It is an interesting issue that the difference between D_{fit} and D_{emp} is unique to ILs or not. If it is unique to ILs, the difference may reflect unique solvation structure or dynamics of ILs which is not considered in this model. In order to check this point, we have simulated the result in ordinal solvent, ethylene glycol (EG)[9]. The data are taken from ref. 9, and the result of the fit is shown in Figure D4. As shown in Table 5-2, D_{fit} was 23 times faster than 2D_{SE} and there still remains large difference. Therefore, the difference may not be ascribed to unique structure of ILs.

Herein, we suggest two plausible reason why the diffusion coefficients obtained from the fitting with SWP model deviated from the conventional theory and empirically calculated one. One is that the diffusional motion discussed here does not correspond to translational diffusion. The translational diffusion coefficient is generally determined by the time- and spatial-averaged solute motion in a long range and time scale. Formally, diffusion coefficient is by the integration of velocity autocorrelation $Z(t)$ to infinite time range[25]

$$D \propto \int_0^\infty Z(t)dt, \tag{5.27}$$

where

$$Z(\mathrm{t}) = \langle \mathrm{v}(0)\mathrm{v}(t) \rangle. \tag{5.28}$$

However, when considering the diffusion process of solute in the initial stage of reaction, we need to consider time-dependence of diffusion coefficient since the diffusive motion related to the geminate recombination is limited in the time and space. In general, the velocity autocorrelation function of molecule in solution relaxes in several ten picoseconds. In the short time scale, the friction which is related to the velocity auto correlation function acting on the molecule from the solvent should differ from the long-time one, as is represented by the memory function of the friction $\Gamma(\mathrm{t})$ [25]

$$\Gamma(\mathrm{t}) = \frac{1}{Z(0)}\left[-m\ddot{Z}(t) - \int_0^t \Gamma(t-t')\dot{Z}(t')dt'\right]. \tag{5.29}$$

(m: mass of solute)

Yamaguchi and coworkers have focused on the microscopic origin of viscosity of ILs and investigated frequency-dependent viscosity of ILs.[26,27] Among various ILs they have reported[26], shear relaxation time of ILs composed of NTf_2 anion, for example, lied in time range of sub nanoseconds to several nanoseconds, which means that steady-state viscosity

can't be attained within ns scale. In the case of the geminate recombination in ILs, the reaction is quite fast and completed within 1 ns as shown in Figs. 5-3 and 5-4. The time scale that the reaction complete within is faster than that for shear relaxation of ILs, which might result in D_{fit} that is larger in one order of magnitude than D_{emp}.

Another reason for the deviation is that SCK equation with SWP might not suitable to the photodissociation reaction. So far, survival probability or time-dependent rate coefficient obtained from diffusional equation with Collins-Kimball boundary condition have been examined by several groups. For example, fluorescence quenching is a well-examined diffusion-limited reaction model between fluorophore and quencher. Time-dependent rate constants and survival probability calculated from the SCK model have given good coincidence with those obtained from MD simulation[28] and experiment.[29] Thus, in the case of bimolecular reaction where initial velocity distribution is in equilibrium, SCK theory have successively given plausible answer. On the other hand, in the case of photo-dissociation, initial velocity distribution is not in equilibrium and biased toward the direction for the bond-dissociation. That initial velocity might make the potential well of the recombination smaller than actual. This might be the one of the reasons why SWP model couldn't simulate the experimental results completely.

Although the discrepancy from the experiment was found for the optimized diffusion coefficient, as mentioned in the last section, bimolecular reaction dynamics in short time is well reproduced by considering potential of mean force (PMF) between reactants. In our SWP model, PMF is expressed by two parameters, the well depth, E and the well distance R. In this paragraph, we discuss the values of E and R. When assuming that R is 7.5 Å, the values of E lie between 1-2 kJ mol^{-1} as shown in Table 5-1. The PMF between radicals ($W_{RR}(r)$) can be evaluated from the radical distribution function (RDF) between

radicals ($g_{\mathrm{RR}}(r)$) as

$$W_{\mathrm{RR}}(r) = -k_B T \ln g_{\mathrm{RR}}(r). \tag{5.30}$$

In principle, $g_{\mathrm{RR}}(\mathrm{r})$ can be evaluated by our MD simulations as described in Chapter 4. However, we could not get enough statistics by the simulations since the number of radical molecules are only two. In this study, we compare the value of E with the PMF between the reactant (BPADS) and solvent ions to estimate the stabilization

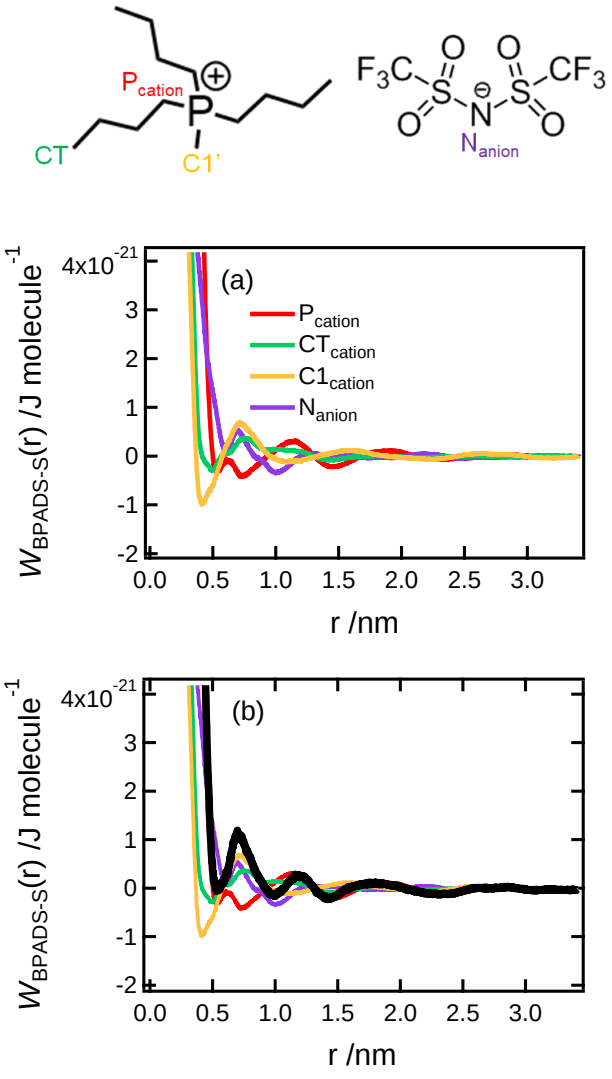

Figure 5-7. Potential mean force (PMF) between BPADS (center of mass of BPADS) and (a) selected atomic group of $[P_{4441}][NTf_2]$ and (b) sum of them.

energy from the solvent to the solute. Figure D5 shows RDF ($g_{\mathrm{BPADS-S}}(\mathrm{r})$) between BPADS (center of mass of BPADS) and atoms of solvent ions of $[P_{4441}][NTf_2]$. We selected several atomic groups of the IL, charged head of anion (N_{anion}, purple curve) and cation (P_{cation}, red curve), terminal alkyl carbon in cation (CT, green curve) and methyl group in cation (C1', yellow curve). From each RDF, we calculated PMF between BPADS and each part of the ILs by eq. (5.31).

$$W_{\mathrm{BPADS-S}}(r) = -k_{\mathrm{B}}T \ln g_{\mathrm{BPADS-S}}(r). \tag{5.31}$$

Figure 5-7 (a) shows $W_{\mathrm{BPADS-S}}(r)$ calculated from $g_{\mathrm{BPADS-S}}(r)$. The PMF between BPADS and ILs were estimated from the summation of each PMF, and is shown in black curve in Figure 5-7 (b). As shown in Fig. 5-7 (b), ILs, on average, builds a potential wall at 7.5 Å for the separation (first minimum of PMF), and its height is approximately 1.2×10^{-21} J molecule^{-1} that corresponds to 0.7 kJ mol^{-1}. This almost corresponds to the value of *E* obtained from fitting. Considering that bulky structure of cation and anion, solvent cage formed by ILs would be actually thicker. Estimated from the primal solvation shell thickness from $g_{\mathrm{BPADS-S}}(r)$ and hydrodynamic radius of the pair of PAPT radical, the cage radius *R* may be extended to 12 Å. If we use this value to estimate the values of *D*, *E*, and r_0 from the optimized parameters ($x(1)$, $x(2)$, and $x(3)$), the calculated value of *E* becomes large (4.1 kJ mol^{-1} in $[P_{4441}][NTf_2]$). The value of *D* becomes also large, while the value of r_0 is not so sensitive to the boundary. (see Table D2).

Finally, we comment another plausible factor which causes a dramatical decrease within 10 ps. As discussed in Chapter 4 (Fig. 4-7), immediately after the photodissociation, spectrum width of absorption spectrum of PAPT radical decreased by pairing conformation of geminate radical. Since the time scale of the decrease almost corresponds

to that of decrease of spectrum integra, the concentration of geminate radicals, that conformation change of the geminate PAPT radicals such as the rotation and the change of their relative conformation in the solvent cage, are the reason for the decrease in the yield within several ten picoseconds.

5.5. Conclusions

In this Chapter, we discuss the geminate recombination of *p*-aminophenylthyil (PAPT) radicals in ILs and explored the theoretical model to reproduce the experimentally observed recombination dynamics by transient absorption spectrum measurements. As already reported in literatures,[6,9] the free diffusion model failed to simulate the time-profile of concertation of PAPT radicals both in the final yield and in the initial rapid decrease. Square well potential (SWP) was implemented to the diffusional equation based on the Smoluchowski-Collins-Kimball (SCK) theory to consider the situation at the initial stage of the reaction, where a pair of radicals is stuck in the solvent cage. The long-time asymptotic form of SWP model was derived and used to fit the experimentally obtained recombination yield. We discussed the validity of the obtained parameters (diffusion coefficient *D*, cage radius *R* and potential depth *E*) obtained by the numerical calculation of the analytic form of the SWP model. Although the diffusion coefficients obtained from the fit was 10-100 times faster than that empirically estimated one, it could be partially rationalized by the transient effect of the translational dynamics between radical pair and the initial velocity distribution of the diffusional motion. The depth of the potential well was somewhat reasonably explained by the results of MD simulations.

Our numerical model, still, cannot reproduce well the initial dynamics within 10 ps. There may be several reasons for the discrepancy. From the theoretical side, frequency dependent translational motion and the initial velocity distribution may be important for the improvement of fitting. The detail of PMF will be also considered. The experiment spectral shape suggests the existence of the strong interaction of radical pair within the first 10 ps. To attain further reproducibility of the experimental results, another theoretical treatment such as Fokker-Plank-Kramers equation[30,31] and more detailed treatment of the

pair potential will be needed.

Appendix D

Table of Contents

D1. The Derivation of eq (5.12)

Agmon and Szabo systematically analyzed the long-time asymptotic behavior of the SCK model.[20] Using their results, we derive the asymptotic expression of the survival probability for the square well potential (SWP) model. In the Laplace space, the asymptotic form of the survival probability for $\mathrm{s} \to 0$ is written as,[20]

$$\widetilde{\Phi}(\mathrm{s}) \sim \frac{1}{\mathrm{s}} - \frac{a_{\mathrm{eff}}}{\mathrm{r_{eff}}} \frac{\mathrm{k_{eff}}}{\mathrm{k_{eff}} + 4\pi \mathrm{D} a_{\mathrm{eff}}} \left[\frac{\sqrt{\gamma_{\mathrm{eff}}^2 \mathrm{D}}}{\mathrm{s}\left(\sqrt{\mathrm{s}} + \sqrt{\gamma_{\mathrm{eff}}^2 \mathrm{D}}\right)} + \frac{(\mathrm{r_{eff}} - \sigma_{\mathrm{eff}})\gamma_{\mathrm{eff}}}{\sqrt{\mathrm{s}}\left(\sqrt{\mathrm{s}} + \sqrt{\gamma_{\mathrm{eff}}^2 \mathrm{D}}\right)} \right], \quad (\mathrm{s} \to 0) \tag{D.1}$$

where we define the parameters as,

$$k_{\mathrm{eff}} = k_a e^E, \tag{D.2}$$

$$a_{\mathrm{eff}} = a\chi(a), \tag{D.3}$$

$$r_{\mathrm{eff}} = r_0 \chi(r_0), \tag{D.4}$$

$$\gamma_{\mathrm{eff}} = \frac{k_{\mathrm{eff}} + 4\pi a_{\mathrm{eff}} D}{4\pi a_{\mathrm{eff}} D} \frac{1}{a_{\mathrm{eff}}}, \tag{D.5}$$

$$\chi(r) = \frac{1}{r}\left[\int_r^\infty \mathrm{d}r' r'^{-2}\, e^{-U(r')}\right]^{-1} \tag{D.6}$$

The inverse Laplace transform of eq (D.1) gives the long-time asymptotic expression,

$$\Phi(t) \sim 1 - \frac{a_{\mathrm{eff}}}{r_{\mathrm{eff}}} \frac{k_{\mathrm{eff}}}{k_{\mathrm{eff}} + 4\pi D a_{\mathrm{eff}}} \left[1 - \{1 - (r_{\mathrm{eff}} - a_{\mathrm{eff}})\gamma_{\mathrm{eff}}\} e^{\gamma_{\mathrm{eff}}^2 Dt} \mathrm{erfc}\left(\sqrt{\gamma_{\mathrm{eff}}^2 Dt}\right)\right], \quad (t \to \infty) \tag{D.7}$$

where we use the Laplace transform,

$$\int \mathrm{d}t e^{-st}\left[1 - e^{at^2}\mathrm{erfc}\left(a\sqrt{t}\right)\&\right] = \frac{a}{s\left(\sqrt{s} + a\right)}, \tag{D.8}$$

$$\int \mathrm{d}t e^{-st}\left[1 - e^{at^2}\mathrm{erfc}\left(a\sqrt{t}\right)\right] = \frac{a}{s\left(\sqrt{s} + a\right)}. \tag{D.9}$$

For the SWP model, eq (D.6), $\chi(r)$ is given by

$$\chi(r) = \frac{R}{r + (R - r)e^{-E}} \tag{D.10}$$

D2. The Green Function of SCK Equation for the SWP Model and the Survival Probability

In this section, we derive the analytic solution of the survival probability for the square well potential (SWP) model using the Green function method.[32,33] The Green's function, *G*, for the probability density is defined as

$$\rho(r,t) \equiv 4\pi \int \mathrm{d}r' r'^2 \, G(r,t|r')\rho(r',0) \tag{D.11}$$

Inserting eq (D.11) into eq (5.1), the time evolution equation of the Green's function is obtained as

$$\frac{\partial G(r,t|r_0)}{\partial t} = \hat{\mathcal{L}}(r)G(r,t|r_0) - S(r)G(r,t|r_0) \tag{D.12}$$

with the initial, boundary and asymptotic conditions,

$$G(r,0|r_0) = \frac{\delta(r-r_0)}{4\pi r_0^2}, \qquad \text{(initial condition)} \tag{D.13}$$

$$\frac{\partial}{\partial r} e^{U(r)} G(r,t|r_0)\Big|_{r=a} = 0, \quad \text{(reflecting boundary condition)} \tag{D.14}$$

$$\lim_{r\to\infty} G(r,t|r_0) = 0. \quad \text{(asymptotic condition)} \tag{D.15}$$

The Laplace transform of eq (D.12) gives

$$s\tilde{G}(s,t|r_0) - \frac{\delta(r-r_0)}{4\pi r_0^2} = \hat{\mathcal{L}}(r)\tilde{G}(s,t|r_0) - S(r)\tilde{G}(s,t|r_0). \tag{D.16}$$

The diffusion operator is decomposed into free diffusion and residual parts

$$\hat{\mathcal{L}}(r) = \hat{\mathcal{L}}_0(r) + D\frac{1}{r^2}\frac{\partial}{\partial r} r^2 U'(r), \tag{D.17}$$

where the free diffusion operator is defined as

$$\mathcal{L}_0(r) \equiv D\frac{1}{r^2}\frac{\partial}{\partial r} r^2 \frac{\partial}{\partial r}. \tag{D.18}$$

Eq (D.18) is rewritten as

$$s\tilde{G}(r,s|r_0) - \frac{\delta(r-r_0)}{4\pi r_0^2} = \hat{\mathcal{L}}_0(r)\tilde{G}(r,s|r_0) - S_{\text{eff}}(r)\tilde{G}(r,s|r_0) \tag{D.19}$$

Here, the residual part of the diffusion operator is included into the effective reaction sink function,

$$S_{\text{eff}}(r) = S(r) - D\frac{1}{r^2}\frac{\partial}{\partial r}r^2U'(r) \tag{D.20}$$

In the absence of the effective reaction sink, $S_{\text{eff}} = 0$, the Green's function is given as[17]

$$\tilde{G}_0(r,s|r_0) = \frac{1}{s-\mathcal{L}_0(r)}\frac{\delta(r-r_0)}{4\pi r_0^2} \tag{D.21}$$

$$= \frac{1}{8\pi D\zeta r r_0}\left[e^{-\zeta|r-r_0|} + \frac{\zeta\sigma-1}{\zeta\sigma+1}e^{-\zeta(r+r_0-2a)}\right], \tag{D.22}$$

$$\zeta = (s/D)^{1/2}.$$

The left multiplication of eq (D.19) by $\left(s-\mathcal{L}_0(r)\right)^{-1}$ gives the Dyson type integral equation for the Green's function,

$$\tilde{G}(r,s|r_0) = \tilde{G}_0(r,s|r_0) - 4\pi\int \mathrm{d}r' r'^2\,\tilde{G}_0(r,s|r')S_{\text{eff}}(r')\tilde{G}(r',s|r_0). \tag{D.23}$$

For the spherical potential well model, eq (5.11), the effective reaction sink function is obtained as,

$$S_{\text{eff}}(r) = k\frac{\delta(r-a)}{4\pi a^2} - DE\left[\frac{2}{r}\delta(r-R) + \delta'(r-R) + \delta(r-R)\frac{\partial}{\partial r}\right]. \tag{D.24}$$

Inserting eq (D.24) into eq (D.23) gives,

$$\begin{aligned}\tilde{G}(r,s|r_0) = \tilde{G}_0(r,s|r_0) - k\tilde{G}_0(r,s|a)\tilde{G}(a,s|r_0)\\ - 4\pi DR^2E\partial_{r_0}\tilde{G}_0(r,s|r_0)\big|_{r_0=R}\tilde{G}(R,s|r_0).\end{aligned} \tag{D.25}$$

When $r = a$ and $r = R$, eq (D.23) receptively becomes

$$\tilde{G}(a,s|r_0) = \tilde{G}_0(a,s|r_0) - k\tilde{G}_0(a,s|a)\tilde{G}(a,s|r_0) - 4\pi DR^2 E\partial_{r_0}\tilde{G}_0(a,s|r_0)\big|_{r_0=R}\tilde{G}(R,s|r_0), \quad \text{(D.26)}$$

$$\tilde{G}(R,s|r_0) = \tilde{G}_0(R,s|r_0) - k\tilde{G}_0(R,s|a)\tilde{G}(a,s|r_0) - 4\pi DR^2 E\partial_{r_0}\tilde{G}_0(R,s|r_0)\big|_{r_0=R}\tilde{G}(R,s|r_0). \quad \text{(D.27)}$$

From the combination of eq (D.26) and eq (D.27), we obtain the algebraic equation with respect to $\tilde{G}(a,s|r_0)$ and $\tilde{G}(R,s|r_0)$. Therefore, $\tilde{G}(a,s|r_0)$ and $\tilde{G}(R,s|r_0)$is given as

$$\begin{bmatrix}\tilde{G}(a,s|r_0)\\ \tilde{G}(R,s|r_0)\end{bmatrix} = \begin{bmatrix}1+k\tilde{G}_0(a,s|r_0) & 4\pi DR^2E\partial_{r_0}\tilde{G}_0(a,s|r_0)\big|_{r_0=R}\\ k\tilde{G}_0(R,s|r_0) & 1+4\pi DR^2E\partial_{r_0}\tilde{G}_0(R,s|r_0)\big|_{r_0=R}\end{bmatrix}^{-1}\begin{bmatrix}\tilde{G}_0(a,s|r_0)\\ \tilde{G}_0(R,s|r_0)\end{bmatrix} \quad \text{(D.28)}$$

Inserting eq (D.28) into eq (D.23) gives the analytic Green's function in the Laplace space. The recombination rate of the geminate reactant pair at time *t* is given by

$$R(t|r_0) \equiv 4\pi\int_a^\infty \mathrm{d}r r^2 S(r)G(r,t|r_0) = kG(a,t|r_0) \quad \text{(D.29)}$$

The survival probability is given as the time integration of the recombination rate,

$$\Phi(r_0,t) \equiv 1 - \int_0^t \mathrm{d}t' R(t'|r_0) = 1 - k\int_0^t \mathrm{d}t' G(a,t'|r_0) \quad \text{(D.30)}$$

The Laplace transform of eq (D.30) gives

$$\tilde{\Phi}(r_0,s) = ks^{-1}\tilde{G}(a,s|r_0). \quad \text{(D.17)}$$

Therefore, the survival probability is obtained from the inverse Laplace transform of $s^{-1}\tilde{G}(a,s|r_0)$. Because the inversion cannot be analytically performed, we numerically calculate the survival probability in the time domain with the Gaver-Stehfest inversion algorithm.[34,35]

D3. Parameters Obtained by the Free Diffusion Model

Table D1-1. Diffusion coefficients (D) obtained by the fitting to the simple diffusion model, assuming initial pair distance r_0 is 7.25 Å.

Cation of Ionic liquids	D / 10^{-5} cm^2 s^{-1}
$[N_{1113}]^+$	0.71
$[N_{2225}]^+$	0.53
$[N_{4441}]^+$	0.45
$[N_{8881}]^+$	0.58
$[P_{2225}]^+$	0.88
$[P_{4441}]^+$	0.65
$[P_{8881}]^+$	0.64
$[P_{8884}]^+$	0.87

Table D1-2. Diffusion coefficients (D) obtained by the fitting of experimentally obtained time-profile in the long time range (20-1000 ps) to the simple diffusion model.

Cation of Ionic liquids	D / 10^{-5} cm^2 s^{-1}	r_0 / Å
$[P_{4441}]^+$	1.51	6.81
	0.86	7.25

D4. Parameters Obtained by the SWP Model (R =8.0, 8.5 and 9.0Å)

Table D2. Potential depth (E), diffusion coefficients (D_{fit}) and initial separation of geminate radicals (r_0) calculated by the resulted parameters obtained by the fitting to SWP model.

(a)

	R = 8 Å		
Ionic liquids	E /kJ mol	D_{fit} /10^{-5} cm^2 s^{-1}	r_0/Å
$[N_{1113}]^+$	2.05	2.19	7.36
$[N_{2225}]^+$	1.86	2.07	7.35
$[N_{4441}]^+$	1.99	1.60	7.36
$[N_{8881}]^+$	2.07	2.26	7.36
$[P_{2225}]^+$	2.03	3.26	7.36
$[P_{4441}]^+$	1.69	2.12	7.31
$[P_{8881}]^+$	1.88	2.28	7.35
$[P_{8884}]^+$	2.10	3.35	7.36

(b)

	R = 8.5 Å		
Cation of Ionic liquids	E / kJ mol	D_{fit} / 10^{-5} cm^2 s^{-1}	r_0 / Å
$[N_{1113}]^+$	2.35	2.38	7.37
$[N_{2225}]^+$	2.15	2.23	7.36
$[N_{4441}]^+$	2.28	1.74	7.37
$[N_{8881}]^+$	2.37	2.45	7.38
$[P_{2225}]^+$	2.33	3.53	7.37
$[P_{4441}]^+$	1.96	2.29	7.32
$[P_{8881}]^+$	2.16	2.47	7.36
$[P_{8884}]^+$	2.41	3.64	7.38

(c)

	R = 9.0 Å		
Cation of Ionic liquids	E / kJ mol	D_{fit} / 10^{-5} cm^2 s^{-1}	r_0 / Å
$[N_{1113}]^+$	2.67	2.59	7.39
$[N_{2225}]^+$	2.46	2.43	7.38
$[N_{4441}]^+$	2.60	1.89	7.39
$[N_{8881}]^+$	2.69	2.67	7.39
$[P_{2225}]^+$	2.65	3.85	7.39
$[P_{4441}]^+$	2.26	2.48	7.33
$[P_{8881}]^+$	2.47	2.68	7.38
$[P_{8884}]^+$	2.73	3.97	7.39

D5. Supplementary Figures

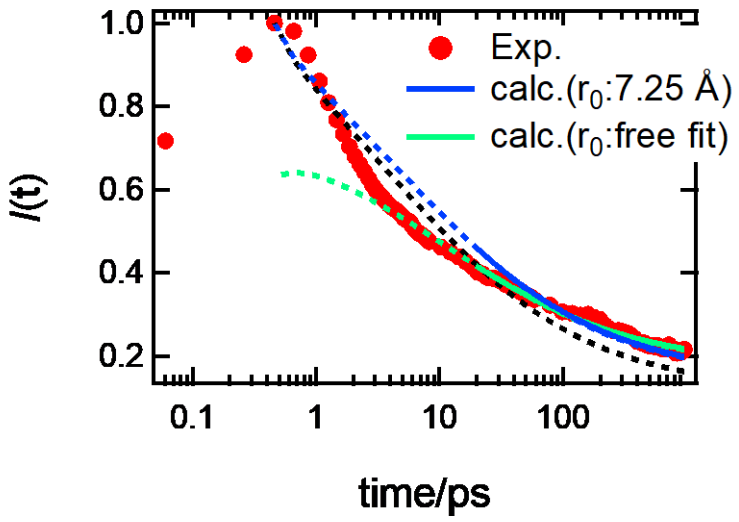

Figure D1. Time profiles of the dissociation yield of the PAPT radical in $[P_{4441}][NTf_2]$ (red circles) and simulation results obtained by fitting of the profile (20-1000 ps) to the free diffusion model (eq. (7)). Green curve is the calculation results obtained when the initial distance r_0 is free parameter, and blue one is that obtained when r_0 = 7.25 Å. Black broken curve is the fitting results as shown in the main text (Figure 4(a)).

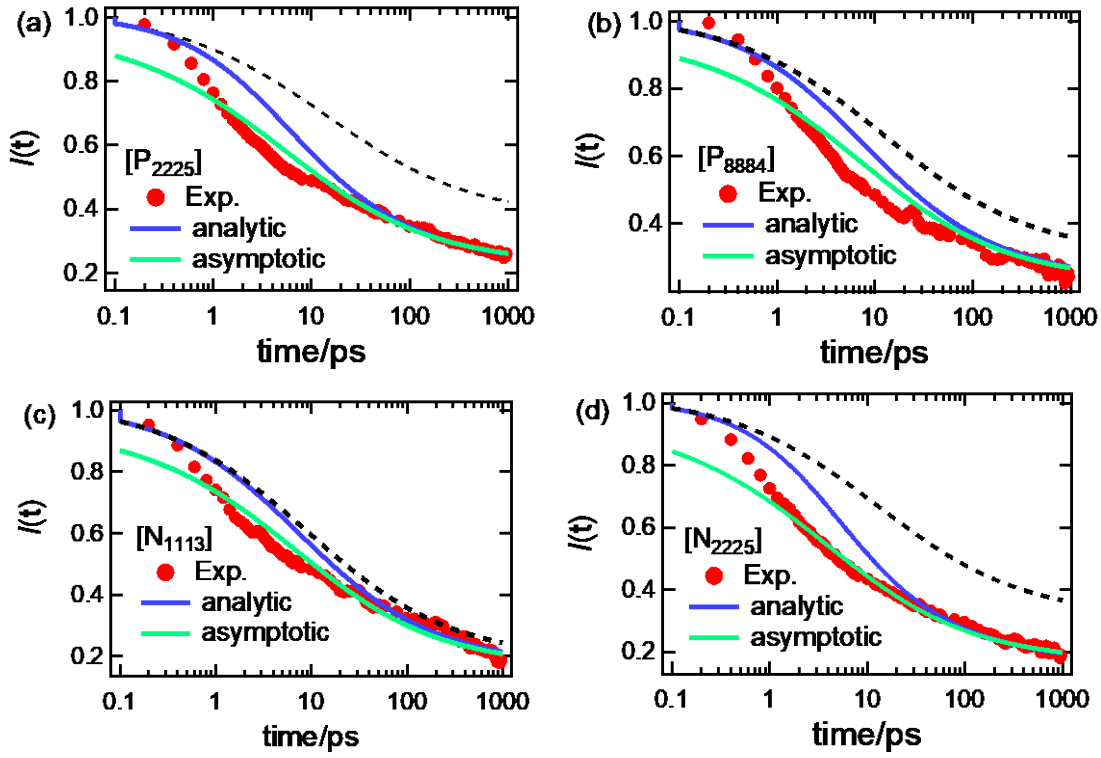

Figure D2. Time profiles of the dissociation yield of the PAPT radical. Red circles are experimental traces, green curves are the fitting results using the asymptotic form (eq (5.12)) using the data from 20 ps to 1000 ps, and blue curves are the numerical calculation results of the analytic form (eq. (D.31)) using the optimized parameters obtained by the fitting. Black broken line represents the numerical calculation of the free diffusion model using the parameters obtained by the fitting.

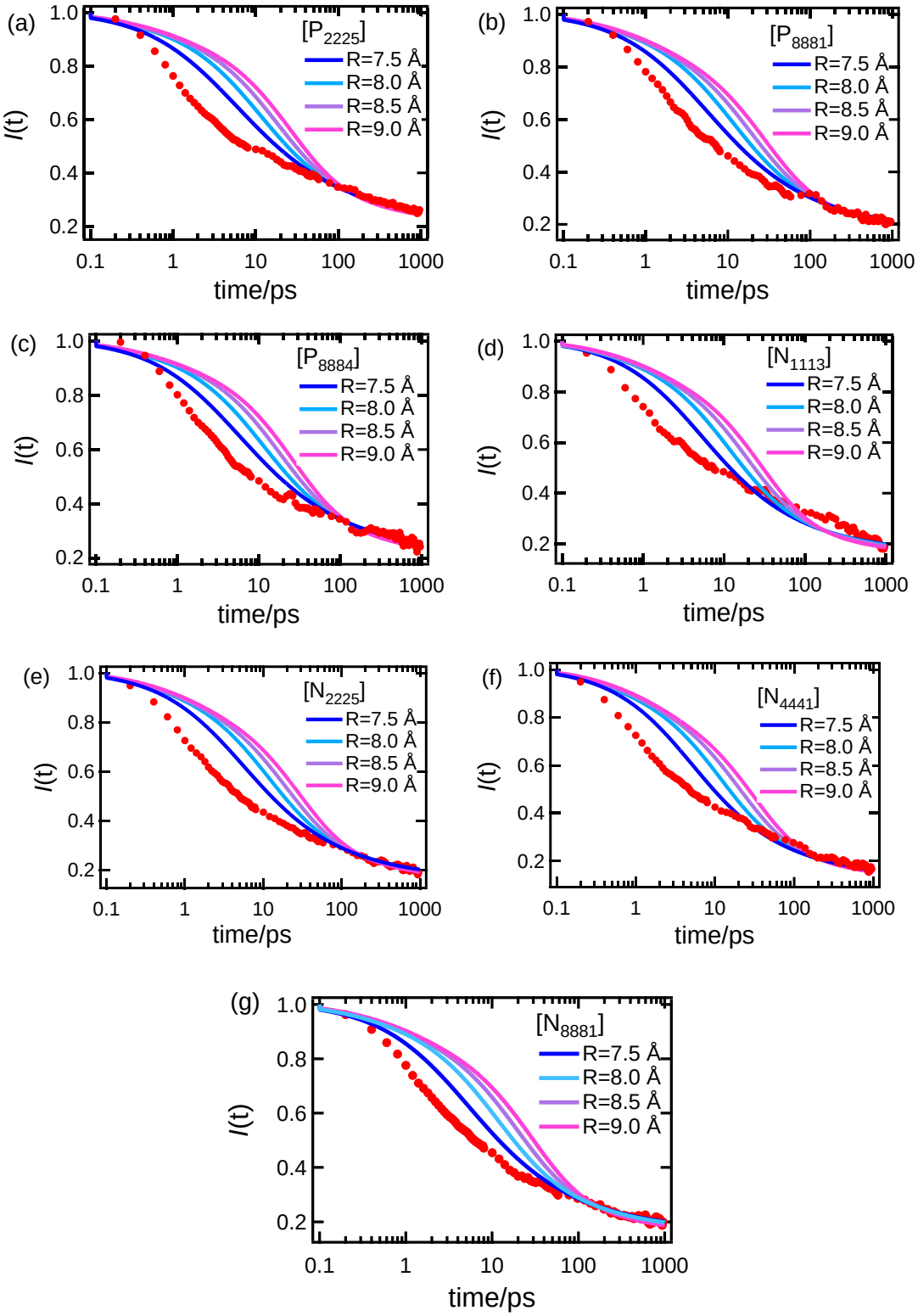

Figure D3. Numerical solution of analytic form of SWP model with obtained parameters for (a) $[P_{2225}][NTf_2]$, (b) $[P_{8881}][NTf_2]$, (c) $[P_{8884}][NTf_2]$, (d) $[N_{1113}][NTf_2]$, (e) $[N_{2225}][NTf_2]$, (f) $[N_{4441}][NTf_2]$ and (g) $[N_{8881}][NTf_2]$. Profiles represented with red markers are experimental results.

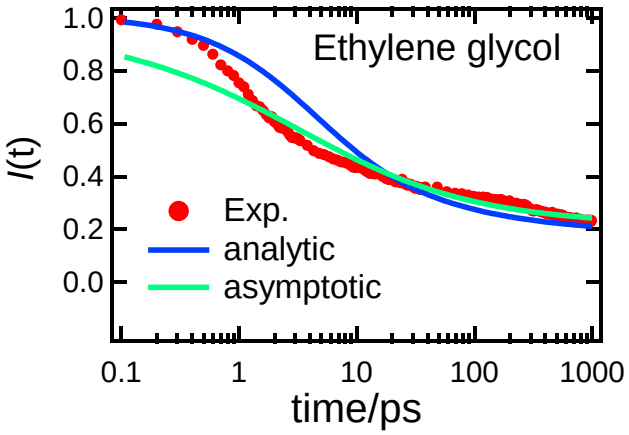

Figure D4. Time profiles of the dissociation yield of the PAPT radical in ethylene glycol. Red circles are experimental traces, and black curves are the fitting results using the asymptotic form (eq (12)) using the data from 20 to 1000 ps.

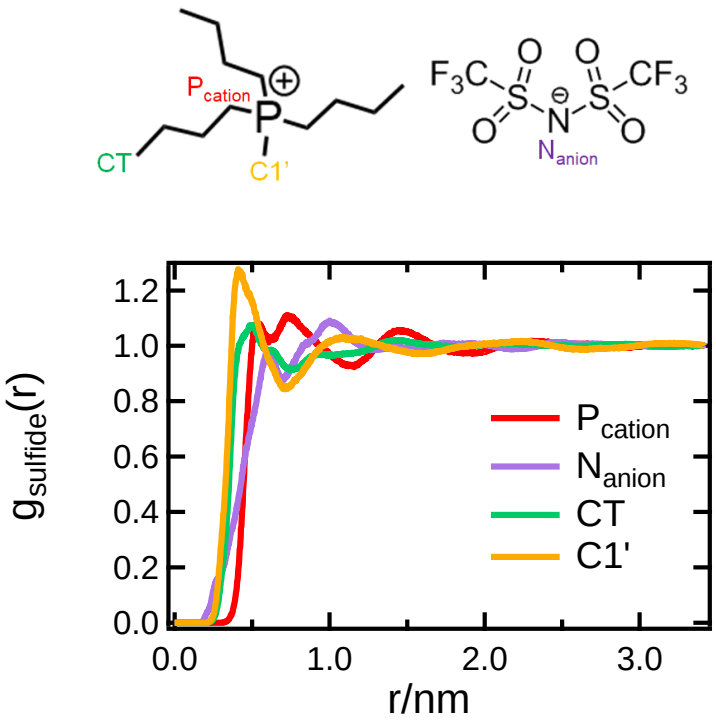

Figure D5. Radial distribution function (RDF) of $[P_{4441}][NTf_2]$ around BPADS (center of mass of BPADS).

References

1. Harris, A. L.; Brown, J. K.; Harris, C. B., The Nature of Simple Photodissociation Reactions in Liquids on Ultrafast Time Scales. *Annual Review of Physical Chemistry* **1988,** *39* (1), 341-366.

2. Franck, J.; Rabinowitsch, E., Some remarks about free radicals and the photochemistry of solutions. *Transactions of the Faraday Society* **1934,** *30* (0), 120-130.

3. Thyrion, F. C., Flash photolysis of aromatic sulfur molecules. *The Journal of Physical Chemistry* **1973,** *77* (12), 1478-1482.

4. Scott, T. W.; Liu, S. N., Picosecond geminate recombination of phenylthiyl free-radical pairs. *The Journal of Physical Chemistry* **1989,** *93* (4), 1393-1396.

5. Ernsting, N. P., Solvation of photolytically generated p-aminophenylthiyl radicals studied by sub-picosecond transient absorption. *Chemical Physics Letters* **1990,** *166* (3), 221-226.

6. Bultmann, T.; Ernsting, N. P., Competition between Geminate Recombination and Solvation of Polar Radicals following Ultrafast Photodissociation of Bis(p-aminophenyl) Disulfide. *The Journal of Physical Chemistry* **1996,** *100* (50), 19417-19424.

7. Kimura, Y.; Sugihara, K.; Terazima, M.; Hirota, N., Study on the Photolysis Quantum Yield of Diphenyl Disulfide by the Transient Grating Method. *Bulletin of the Chemical Society of Japan* **1997,** *70* (11), 2657-2664.

8. Kimura, Y.; Saga, N., Application of the time-resolved spectroscopy on the photo-dissociation dynamics of disulfide compounds in supercritical fluids. *Journal of Molecular Liquids* **2005,** *119* (1-3), 113-117.

9. Osawa, K.; Terazima, M.; Kimura, Y., Photo-dissociation dynamics of bis(p-dimethylaminophenyl) disulfide in ionic liquids studied by ultrafast transient absorption spectroscopy. *Chemical Physics Letters* **2013,** *564*, 21-25.

10. Hirata, Y.; Ohta, M.; Okada, T.; Mataga, N., Direct observation of photodissociation of tetraphenylhydrazine and its derivatives in the solution phase: picosecond study of nitrogen-nitrogen bond rupture in the fluorescence state. *The Journal of Physical Chemistry* **1992,** *96* (4), 1517-1520.

11. Collins, F. C.; Kimball, G. E., Diffusion-controlled reaction rates. *Journal of Colloid Science* **1949,** *4* (4), 425-437.

12. K. M. Hong and J. Noolandi, The Journal of Chemical Physics 68(11), 5163-5171 (1978).

13. K. Lee, J. Sung, C. H. Choi and S. Lee, The Journal of Chemical Physics 152(13), 134102 (2020).

14. Strehmel, V.; Wishart, J. F.; Polyansky, D. E.; Strehmel, B., Recombination of photogenerated lophyl radicals in imidazolium-based ionic liquids. *ChemPhysChem* **2009,** *10* (17), 3112-3118.

15. Berdzinski, S.; Horst, J.; Straßburg, P.; Strehmel, V., Recombination of lophyl radicals in pyrrolidinium-based ionic liquids. *ChemPhysChem* **2013,** *14* (9), 1899-1908.

16. Okada, T.; Yago, T.; Takamasu, T.; Wakasa, M., Cage lifetimes of ionic liquids as studied by the magnetic field effect probe. *Physical Chemistry Chemical Physics* **2012,** *14* (10), 3490-3497.

17. Rice, S. A., *Diffusion-limited reactions*. Elsevier: 1985.

18. Wilemski, G.; Fixman, M., General theory of diffusion-controlled reactions. *The Journal of Chemical Physics* **1973,** *58* (9), 4009-4019.

19. Ibuki, K.; Ueno, M., Effect of potential of mean force on short-time dynamics of a diffusion-controlled reaction in a hard-sphere fluid. *The Journal of Chemical Physics* **1997,** *107* (17), 6594-6602.

20. Agmon, N.; Szabo, A., Theory of reversible diffusion-influenced reactions. *The Journal of Chemical Physics* **1990,** *92* (9), 5270-5284.

21. Kaintz, A.; Baker, G.; Benesi, A.; Maroncelli, M., Solute Diffusion in Ionic Liquids, NMR Measurements and Comparisons to Conventional Solvents. *The Journal of Physical Chemistry B* **2013,** *117* (39), 11697-11708.

22. Kimura, Y.; Kida, Y.; Matsushita, Y.; Yasaka, Y.; Ueno, M.; Takahashi, K., Universality of Viscosity Dependence of Translational Diffusion Coefficients of Carbon Monoxide, Diphenylacetylene, and Diphenylcyclopropenone in Ionic Liquids under Various Conditions. *The Journal of Physical Chemistry B* **2015,** *119* (25), 8096-8103.

23. Bultmann, T. Dissertation, Universita¨t Go¨ttingen, **1994**

24. Bondi, A., van der Waals Volumes and Radii. *The Journal of Physical Chemistry* **1964,** *68* (3), 441-451.

25 Yamaguchi, T.; Kimura, Y., Effects of Solute-Solvent Attractive Interactions on Solute Diffusion. Molecular Physics, 2000, 98, 1553-1563

26. T. Yamaguchi, E. Nakahara and S. Koda, The Journal of Physical Chemistry B 118(21), 5752-5759 (2014).

27. T. Yamaguchi, K. Mikawa, S. Koda, K. Fujii, H. Endo, M. Shibayama, H. Hamano and Y. Umebayashi, The Journal of Chemical Physics 137(10), 104511 (2012).

28. I. Kazuyasu and U. Masakatsu, Bulletin of the Chemical Society of Japan 79(10), 1509-1518 (2006).

29. E. Krystkowiak and A. Maciejewski, The Journal of Chemical Physics 117(12), 5802-5809 (2002).

30. S. A. Adelman, The Journal of Chemical Physics **64** (1), 124-130 (1976).

31. K. Ibuki and M. Ueno, Bulletin of the Chemical Society of Japan **70** (3), 543-553 (1997).

32. Son, C. Y.; Lee, S., Effects of the interaction potential and hydrodynamic interaction on the diffusion-influenced reaction rates. *The Journal of Chemical Physics* **2011,** *135* (22), 224512.

33. Lee, K.; Sung, J.; Choi, C. H.; Lee, S., Green's function of the Smoluchowski equation with reaction sink: Application to geminate and bulk recombination reactions. *The Journal of Chemical Physics* **2020,** *152* (13), 134102.

34. D. P. Gaver, J., Observing Stochastic Processes, and Approximate Transform Inversion. *Operations Research* **1966,** *14* (3), 444-459.

35. H. Stehfest, *Commun. ACM* **1970**, 13, 47.

Chapter 6

Concluding Remarks and Perspectives

In this study, we have extensively investigated two examples of fundamental chemical reactions, proton transfer reaction and photo-dissociation and recombination reaction, by the time-resolved spectroscopic method and discuss the effect of solvation energy and solvation dynamics on the reaction kinetics. As solvents, we selected ionic liquids (ILs) and high-temperature and high-pressure methanol.

In Chapters 2 and 3, we have focused on intermolecular proton transfer (PT) dynamics in supercritical methanol and protic ionic liquids (PILs), and discuss how solvation energy and solvation dynamics involve the PT kinetics. In high-temperature and high-pressure methanol and n-alcohols under ambient condition, PT kinetics were explained by the change in solvation energy. From steady-state absorption and fluorescence spectrum, we successively related the change in the peak position of acidic form of cyanonaphthol to Kamlet-Taft hydrogen-bonding (HB) basicity (β), i.e., at equilibrium, initial state of proton transfer is stabilized with the increase of HB basicity. On the other hand, the dynamic effects of the solvent molecule, solvation dynamics were much faster than the intrinsic PT in all alcohols at various thermal condition. We concluded that the change in activation free energy by the solvation energy was the determining factor which describes the solute-solvent intermolecular PT in high-temperature and high-pressure methanol and various alcohol.

As described in Chapter 1, one of the famous physicochemical aspect of SCF is density inhomogeneity. Although we had expected that solute-solvent PT kinetics reflects the density enhancement around the solute, we didn't observe the PT itself near and above the critical point. Local density inhomogeneity has often been assessed by the peak shift in the electronic spectrum of solute molecule. Along the 30 MPa isobar condition, absorption spectrum of DCN2 at various temperature (295~523K) showed higher-energy

shift (blue-shift) with increasing temperature: electronic energy state of DCN2 had linear correlation of the solvent density. Thus, inhomogeneous effect on the density was not observed in our case.

In PILs, we observed that solvent species affected PT mechanism; PT yield and dynamics significantly depended on the HB basicity of anion composed of PILs. From relative intensity of fluorescence spectrum of 5-cyano-2-naphthol (5CN2) and 5,8-dicyano-2-naphthol (DCN2), PT yield of each species (acidic form, HB complex form and anionic form) in the excited state depended on the acidity of conjugate acid of anion composed of PILs. Contrary to the case in supercritical methanol, it was found that proton dissociation process was concerted to dynamic solvent reorganization. Formation kinetics of Y^{-}* (HB complex between solute and anion of PILs) from ROH was controlled by the diffusional process of anion toward the solute. Although in our study, proton donation from ($N_{222}H$) of PILs was not observed, its role is one of the important properties of PILs. Using another molecular probe (6-hydroxyquinoline) which has both photo-acidic and -basic properties, our group recently have discovered unique PT mechanism between solute and PILs, where both proton acceptance and donation of PILs involve the reaction. Series of our work will contribute to give more generalized description of solute-solvent PT mechanism in PILs and roles of molecular properties of solvents in proceeding PT reaction.

To sum up the studies in Chapters 2 and 3, we can put those solvents in order of HB acceptance ability: high-temperature methanol (at 30 MPa isobar) < methanol at ambient condition < n-alcohols at ambient condition (n=2~10) < anions composed of PILs ($CF_3SO_3^{-}$ < $CH_3SO_3^{-}$ < CF_3COO^{-}). Based on the order of HB basicity, solute-solvent intermolecular PT kinetics is interpreted as follows. When HB basicity is smaller than

anions of PILs, PT kinetics is explained by the change in activation free energy controlled by concerted effect of HB basicity and polarity/polarizability of solvents. Based on the pK_a* value calculated by experimentally obtained PT rate constants, ROH* is more stabilized rather than RO* in various alcohols. In this region, the concerted effect of these Kamlet-Taft parameters is divided into two regions by methanol at ambient conditions, as discussed in Chapter 2. On the other hand, when HB basicity is as large as anions composed of PILs, ROH* and proton acceptor can form relatively strong HB, that makes the energy state of HB complex lowered. Thus, we could capture the kind of intermediate species of PT by fluorescence spectrum.

In Chapters 4 and 5, in order to investigate how fundamental reaction kinetics in ILs are related to their inhomogeneous structure, we focus on the solvation dynamics of ionic ILs and their effects on the bimolecular dynamics: recombination of geminate radical pair. Since the photodissociation reaction is accompanied by the change of not only the polarity but also the molecular volume of reactant, we had expected that it could induce significant change in the solvation structure of ILs. However, experimental results showed that photodissociation of solute molecule didn't alter solvation structure of ILs significantly. It is also noted that neither solvation dynamics nor geminate recombination of radical pair showed meaningful dependence on the cation species of ILs. From the detailed analysis of transient absorption spectrum and theoretical treatment for geminate recombination, we conclude that the solvent motions to influence these molecular dynamics don't related to the viscosity of ILs.

As mentioned in the conclusion in Chapters 4 and 5, there still remains questions both for the solvation dynamics of photodissociated products and recombination dynamics. Solvation dynamics especially in the excited state of photodissociated products

didn’t reflect the solvation structure in the ground state. From recombination dynamics, it is also found that recombination dynamics completed faster than that predicted from the viscosity of ILs. We need to investigate the very initial dynamics after the photodissociation. It will be possible by our ongoing work using time-resolved vibrational spectroscopy.

As was not mentioned in the main context, another unique property of ILs that comes from inhomogeneous structure is structural relaxation. Formation or deformation of domain structure of ILs would be occurred and have attract great interest. There are several researches to computationally observe collective motion of domain in ILs. We now work on examining the experimental methods to observe this by time-resolved spectroscopic method. This work will shed a light on new physicochemical aspect of ILs and discover new mechanisms for fundamental reaction in solution.

List of Publications

Chapter 2

‘‘Excited-State Proton Transfer of 5,8-Dicyano-2-naphthol in High-Temperature and High-Pressure Methanol: Effect of Solvent Polarity and Hydrogen Bonding Ability’’

Kaori Fujii, Megumi Aramaki and Yoshifumi Kimura, *J. Phys. Chem B*. **2018**, *122*, pp.12363-12374.

Chapter 3

“Excited -State Proton Transfer of Cyanonaphthols in Protic Ionic Liquid: Appearance of a New Fluorescence Species”

Kaori Fujii, Yoshiro Yasaka, Masakatsu Ueno, Yoshinari Koyanagi, Sora Kasuga, Yoshihiro Matano, Yoshifumi Kimura, *J. Phys. Chem B*. **2017**, *121*, pp. 6042-6049.

Chapter 4

“Experimental Observation of Unique Solvation Process Along Multiple Solvation Coordinates of Photodissociated Products”

Kaori Fujii, Hiroshi Nakano, Hirofumi Sato, and Yoshifumi Kimura, *Phys. Chem. Phys. Chem.* in press, 2021.

Chapter 5

“Experimental and Theoretical Study on Geminate Recombination of *p*-Aminophenylthyil radical in Ionic Liquids; Analysis with Smoluchowski-Collins-Kimball Equation ”

Kaori Fujii, Tomoaki Yagi, Hiroshi Nakano, Hirofumi Sato, and Yoshifumi Kimura

J. Chem. Phys. to be submitted.

Acknowledgement

I would like to appreciate Prof. Y. Kimura first of all, who have guided me to the present study and of course, to doctoral course. I have learned the essence of physical chemistry with the comments and helpful discussion to my research.

I also appreciate Prof. T. Endo for useful discussion.

I would like to appreciate Prof. M. Kato at Doshisha Univ. and K. Iwata at Gakushuin Univ. who were sub-examiner of my doctoral thesis.

I appreciate the co-workers at Niigata Univ., Prof. Y. Matano, Mr. S. Kasuga and Mr. Y. Koyanagi for useful advise on the synthesis of cyanonaphthol.

I'm grateful to the co-workers at Kyoto Univ., Prof. H, Sato, Associate Prof. H. Nakano and Mr. T. Yagi for useful discussion for Chapter 4 and 5. Prof. H. Sato and Prof. H. Nakano gave us helpful comments on the computer simulation for Chapter 4, and Mr. T. Yagi made a great contribution for the proposal of mathematical model in Chapter 5.

I'm grad to learn the great works by Prof. K Ibuki. Thanks to the contribution to the theoretical treatment of the chemical reaction dynamics in solution, we could advance the discussion for treatment of diffusion-limited reaction model and come to the conclusion.

I would like to appreciate Emeritus Prof. M. Ueno and Dr. Y. Yasaka. They taught me the interest and difficulty of research at the beginning of laboratory life.

I would like thank all of the colleagues in Physical Chemistry laboratory. I have learned much from their attitude to the research, way of scientific thinking and their interests. Writing this thesis, I could review my own researches from different point of view.

I thank JSPS for the Fellowship for the Japanese Junior Scientists.

Finally, I am grateful of my family, especially my mother who always have given warm support so far.